The Effect of Corrosion Thinning on the Collapse Pressure of a Submarine Pressure Hull

by
Hermanus Carl Viljoen

Thesis presented in partial fulfilment of the requirements for the degree of Master of Engineering (Mechanical) in the Faculty of Engineering at Stellenbosch University

Supervisor: Prof Nawaz Mahomed

March 2021

Declaration

By submitting this thesis electronically, I declare that the entirety of the work contained therein is my own, original work, that I am the sole author thereof (save to the extent explicitly otherwise stated), that reproduction and publication thereof by Stellenbosch University will not infringe any third party rights and that I have not previously in its entirety or in part submitted it for obtaining any qualification.

Date: March 2021

Abstract

The effect of corrosion thinning on a submarine pressure hull is investigated using electrochemical and immersion corrosion testing, material characterisation techniques and nonlinear finite element analysis. HY-80 steel in as-received condition as well as heat treated for 90 min at 590°C was investigated. It was found that the mechanical and microstructural properties of the two conditions were almost identical. The linear- and potentiodynamic polarization techniques were used to estimate corrosion rates of 0.17 mm/year and 0.18 mm/year for as received and heat treated HY-80 in seawater. These rates were verified by immersion testing which estimated a rate of 0.19 mm/year. Measurement of actual remaining wall thickness on a submarine with a service life of 10 years was achieved using an ultrasonic through thickness gauge. The actual loss of material was found to be a maximum of 0.201 mm/year.

A finite element analysis of a 15.05 m long Type 209/1400 submarine section consisting of pressure hull plating and stiffeners was conducted. Material non-linearity was incorporated by using a true stress-strain curve for HY-80 steel. Initial overall and interframe out of circularity imperfections were introduced into the model using a Matlab script that displaced the model mesh radially. It was estimated that the submarine under investigation would collapse at a depth of roughly 560 m which relates to a safety factor of 2.25 against collapse at a normal operating depth of 250 m. It was found that collapse was preceded by yielding of stiffeners where the maximum out of circularity imperfection was introduced. Collapse pressures were found to reduce mostly linearly with wall thickness at a rate of approximately 27 kPa per year.

Uittreksel

Die effek van korrosie verdunning op die ineenstortings druk van ’n duikboot romp is ondersoek deur elektrochemiese en onderdompelings korrosie toetse, materiaal karaktariseerings tegnieke en nie-lineêre eindige-elementontleding. HY-80 staal was ondersoek in twee materiaal toestande; soos ontvangstoestand en hitte behandeld teen 590°C vir 90 minute. Dit was bepaal dat die meganiese en mikrostrukturele eienskappe van die staal toestande amper identies is. Lineêre- en potensiodinamiese polarisasie tegnieke was gebruik om ’n korrososiesnelheid van 0.17 mm/jaar en 0.18 mm/jaar in natuurlike seewater vir soos ontvangde en hitte behandelde staal te bepaal. Hierdie snelhede was bevestig met onderdompelingstoetse wat ’n korrosiesnelheid van 0.19 mm/jaar vir beide toestande voorspel het. ’n Ultrasoniese deurdiktemeter was gebruik om die oorblywende wanddikte van ‘n duikboot te meet wat vir tien jaar in gebruik was. Dit is bevind dat die maksimum korrosiekoers tot 0.201 mm/jaar was.

’n Eindige-element analise van ’n 15.05 m lange Tipe 209/14000 duikboot seksie is uitgevoer. Die seksie bestaan uit ‘n romp en interne versterkers. Materiaal nie-lineariniteit was in ag geneem deur die ware plastiese gedrag van HY-80 te inkorporeer. Aanvanklike algehele en tussenraam buite sirkelvormige onvolmaakthede is in die model geïnkorporeer met behulp van ’n Matlab program wat die eindige-element-netwerk knooppunte radiaal verplaas het. Dit is beraam dat die duikboot wat ondersoek is, teen ‘n diepte van ongeveer 562 m sal ineenstort wat beteken dat die veiligheidsvaktor teen ineenstorting 2.25 in plek is indien die standaard duikdiepte 250 m is. Daar is bevind dat die versterkers, in die area waar die maksimum onvolmaakdhede ingevoeg is, swig voordat die romp ineenstort. Dit is voorspel dat die maksimum duik druk ongeveer lineêr teen 27 kPa per jaar afneem.

Acknowledgements

The author of this project would like to acknowledge and thank the Armaments Corporation of South Africa who funded this research under the Defence Engineering and Science University Programme (DESUP).

I would also like to express my deepest gratitude to the following individuals who supported me in completion of this project:

My study leader, Prof. Nawaz Mahomed for his valuable guidance and supervision. Thank you for giving me the opportunity to further my studies.

Mr. Llewellyn Cupido for his guidance in completion of experimental work.

Finally, I would like to thank my family for their financial and emotional support throughout my studies. Without their love and encouragement this project would not have been possible.

Table of contents

List of figures

Page

List of tables

Page

List of symbols

A	Exposed area
A_o	Maximum overall out-of-circularity imperfection
A_i	Maximum interframe out-of-circularity imperfection
B	Stern-Geary constant
b_a	Anodic Tafel slope
b_c	Cathodic Tafel slope
CR	Corrosion rate
E	Potential
E_{corr}	Corrosion potential
E_o	Standard reversable potential
E_{OCP}	Open circuit potential
E_r	Reversable potential
E_y	Young's modulus
EW	Equivalent weight
F	Faraday's constant
f	Mass fraction
F_a	Equivalent longitudinal load
G	Gibbs free energy
H	Enthalpy
I	Total current
i	Total current density
i_a	Anodic current density
i_{app}	Applied current density
i_c	Cathodic current density
i_L	Diffusion limited current
i_{corr}	Corrosion current density
L_c	Compartment length
L_r	Position of a node relative to two adjacent stiffeners
m	Mass

m_W	Mass in water
n	Number of electrons transferred
n_o	Overall out-of-circularity
n_i	Interframe out-of-circularity
P	Pressure
P_b	Boiler pressure
P_y	Yield pressure
P_m	Von Mises buckling pressure
P_n	Bryant's overall elastic collapse pressure
Q	Charge
q	Charge density
R	Universal gas constant
R_p	Polarization resistance
r	Radius
S	Entropy
t	Wall thickness
T	Temperature
v	Poisson's ratio
W	Atomic weight
x	Position relative to the centre of a submarine section
ε	Strain
η	Overpotential
ρ_s	Density of steel
ρ_w	Density of water
σ_y	Yield strength
σ_c	Circumferential stress
σ_l	Longitudinal stress
φ	Imperfection phase angle

List of acronyms

ARMSCOR	Armaments Corporation of South Africa
DESUP	Defence Engineering and Science Program
SAN	South African Navy
SDF	Submarine Design Formulas
SCE	Saturated Calomel Electrode
WEDM	Wire Electrical Discharge Machining

1 Introduction

1.1 Background

Submarines experience varying hydrostatic loads while in operation due to diving, wave action, engine vibration and even shock loads associated with underwater explosions. During the initial design stage, sound engineering practice would have been implemented to ensure that the relevant safety factors to ensure safe operation are met. Post-production quality assurance processes such as hull and weld inspections would have ensured that the product conformed to the engineering specifications. However, in-service monitoring of the serviceability, which includes analysing the effect of corrosion and operating loads on hull integrity, remains an ongoing requirement.

Operation of submarines in seawater will inevitably lead to corrosion, which is typically initiated where coatings have failed or at sites where acoustic tiles have been debonded (Gannon, 2010). Thinning of the hull material could potentially reduce the safe operational limits of the vessel and, therefore, the effect of thinning needs to be thoroughly understood. The cost and time implications of remedial measures needed to repair corrosion damage is often prohibitive and therefore submarines are often operated without any action taken.

A body of knowledge on the effect of corrosion thinning on collapse pressure already exists, as extensive experimental and numerical research has already been conducted. However, considering the case-specific nature of corrosion and stress analysis, it would be advantageous to develop a local expertise in the field for application in specific cases such as the S-class (Type 209-1400mod) submarine fleet of the South African Navy (SAN).

Although previous studies investigated the effect of corrosion thinning on the collapse pressure of a submarine hull, this would be the first study to link experimentally obtained corrosion rates to reduction of operational limits. This would be the first step in enabling the South African Navy to introduce strategies and measures to ensure safe operation of their submarine fleet.

1.2 Objectives

The aim of this research is to investigate the effect of uniform corrosion thinning on the operational limits of a Type 209-1400 submarine pressure hull.

Therefore, the research objectives are:

i. Determine the uniform corrosion rate of the submarine hull material in seawater.

ii. Determine the kinetic parameters associated with the corrosion mechanism to enable instantaneous corrosion rate determination.

iii. Investigate the integrity of the submarine hull by comparing experimentally estimated corrosion rates to that of the hull structure that has been in service for a period of approximately 10 years.

iv. Perform a finite element analysis on the critical section of the submarine hull and incorporate corrosion thinning to determine the reduction of in operational depth with time.

1.3 Scope and limitations

This research project was facilitated by the Armaments Corporation of South Africa SOC Ltd (ARMSCOR) as part of their Defence Engineering and Science University Program (DESUP), which is aimed at developing local, military applicable knowledge. This is, however, limited to non-sensitive knowledge and therefore, certain information that was applicable to the study was not made available for this research. In cases where critical data was not available, reasonable estimations of the parameters were made using literature available in the public domain.

The corrosion and strength analysis contained in this study is limited to uniform corrosion and thinning of unprotected HY-80 in stagnant water. Other mechanisms such as pitting and associated stress corrosion cracking, as well as effects of weld embrittlement and residual stresses, were not investigated. Uniform corrosion is very important in large structures exposed to aggressive environments such as seawater (Fontana, 1987). Other forms of corrosion such as galvanic corrosion or pitting are also possible and was observed on the investigated submarine but can be addressed by removal and replacement of corroded material or built up using several layers of weld metal (Gannon, 2010). This is not possible for general corrosion where the whole structure is being thinned.

Furthermore, the effects of casting and penetrations were not modelled, since the details of these structures were not made available, and these are typically

designed to increase the strength of the hull structure (Gannon, 2010; Smith, Macadam and MacKay, 2015).

1.4 Thesis outline

Chapter 2 presents a literature review covering corrosion theory, corrosion rate estimation, characterisation of HY-80 steel and the analysis of submarine pressure hulls.

Chapter 3 presents the experimental procedures followed to achieve the objectives set by this study.

Chapter 4 presents the simulation methodology followed to perform a Finite Element Analysis (FEA) on the investigated submarine pressure hull.

Chapter 5 presents and discusses the experimental results obtained from an investigation into the mechanical properties of the steel, material characterisation and corrosion analysis.

Chapter 6 presents and discusses the simulation results.

Chapter 7 presents a summary of the results and conclusions drawn from the study.

Chapter 8 presents recommendations for possible continuation of this research.

2 Literature Review

2.1 Fundamental Corrosion Theory

2.1.1 Definition of Corrosion

Corrosion is the deterioration or destruction of a material as it reacts with its environment (Roberge, 2000). According to Cicek (Cicek, 2014), this reaction is either chemical or electrochemical.

Fontana (Fontana, 1987) describes corrosion as extractive metallurgy in reverse (Figure 1), which also serves as an excellent explanation for why corrosion takes place. In nature, metals are found in a low-energy thermodynamically stable state, known as ore. A large amount of heat is applied to the ore during refining processes which leads to an increase in the Gibbs free energy, a measure of the relative stability of a system:

$$G = H - TS \tag{2.1.1}$$

where G is the Gibbs free energy, H the enthalpy, T the temperature and S the entropy. A system is most stable when the Gibbs free energy is minimised.

$$\Delta G = 0 \tag{2.1.2}$$

Therefore, if given the opportunity, a system will revert to a more thermodynamically stable state.

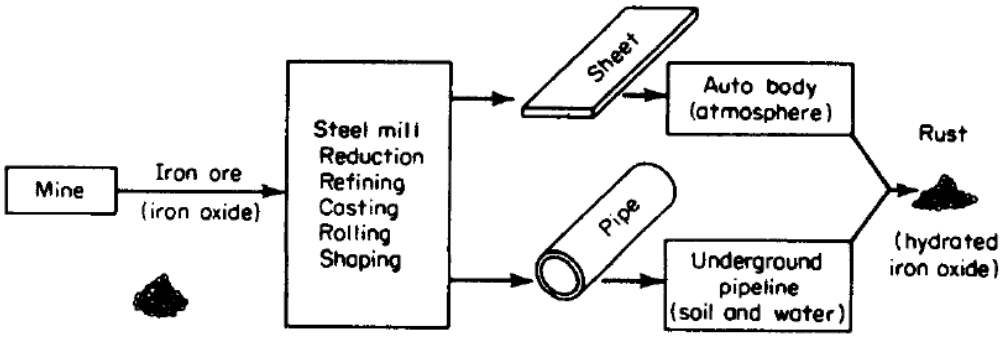

Figure 1: Metallurgy in reverse (Fontana, 1987)

2.1.2 Classification of Corrosion

Corrosion can be classified in many different ways, such as low and high temperature or oxidation and electrochemical corrosion. Fontana (1987) classifies corrosion as either wet or dry corrosion.

Wet corrosion is by far the most aggressive. Wet corrosion involves aqueous solutions of electrolytes. Dry corrosion takes place in the presence of vapours and gasses. Therefore, dry corrosion usually takes place at high temperatures above the dew point of the environment.

According to Fontana (1987), the classification of corrosion is very important as moisture could completely change the elements involved in corrosion; for example, chlorine is noncorrosive to dry steel, but chlorine attacks most metals once dissolved in water. In this study, wet corrosion is the primary cause of material deterioration.

2.1.3 Corrosion Mechanisms

Practically all forms of corrosion could be grouped in either uniform, galvanic or two-metal corrosion, pitting, crevice corrosion, intergranular corrosion, selective leaching, erosion corrosion or stress corrosion (Fontana, 1987). These different corrosion mechanisms can be grouped into three categories (Roberge, 2000) as shown in Table 1.

This study's principal focus is on uniform corrosion. Uniform/General corrosion is the thinning of material over time. Uniform corrosion takes place over large surface areas, and is therefore considered the most destructive form of corrosion in terms of material mass loss (Cicek, 2014). Although general corrosion is not of concern in most cases, as penetration rate is typically slow, it is important for applications where the weight and cost of a structure had to be optimised in the design process, when the lifetime of the structure is exceptionally long or when the safety of the environment or human lives are at stake. Some examples are pipelines, nuclear storage tanks and in the case of this study, a submarine pressure hull.

Table 1: Corrosion mechanism categories (Roberge, 2000).

Group 1: Identifiable by visual inspection	Group 2: Identifiable by special inspection tools	Group 3: Identifiable by microscopic inspection
Uniform corrosion	Erosion	Exfoliation
Pitting	Cavitation	De-alloying
Crevice corrosion	Fretting	Stress corrosion cracking
Galvanic corrosion	Intergranular corrosion	Corrosion fatigue

2.1.4 Factors Influencing Corrosion

2.1.4.1 Nature of the metal

The nature of a metal is an important factor to consider when designing with corrosion in mind. The composition of the steel, the position in the galvanic series, imperfections on the surface, heat treatment and nature of the corrosion product will all influence the corrosion mechanism and the corrosion rate of a steel. Another important phenomenon is that of passivation, in which an alloy exhibits a much higher corrosion resistance than expected from its position on the galvanic series. This is because of the formation of a very thin film on the surface of the metal that makes it passive to oxidizing environments. Chromium or chromium-nickel steels, nickel-chromium, nickel-copper and titanium alloys are all passivating. Steels with a minimum of 13% chromium show similar passivation characteristics to pure chromium (Cicek, 2014). A 50-60% nickel content is required for nickel-chromium alloys to exhibit the passivation characteristics of pure nickel.

2.1.4.2 Nature of the Corroding Environment

The nature of the environment is the other determining aspect influencing a metal's susceptibility to corrosion. Fluid velocity, pH, temperature, presence of aggressive ions such as chlorides and sulphates, dissolved oxygen, and composition of the corroding environment will all have an impact on the rate of corrosion and the mechanisms present (Roberge, 2000).

2.2 Corrosion of Metals in Seawater

Seawater is highly corrosive due to its high conductivity and its chloride content that prevents passivation in some steels. As discussed by Hudson, Stanners and Hooper (1994), seawater is one of the most severe natural corroding environments. Cicek (2014) notes that seawater is about 250 times more corrosive than fresh water.

Natural seawater has a complex composition of many major constituents. For convenience, the concentration of salts in a sample of seawater is often reported in chloride content.

$$salt\ level\ \left(\frac{g}{kg}\right) = 1.80655\ \times chloride\ concentration \qquad (2.2.1)$$

The salinity of water can also be measured by density or as a function of electrical conductivity. Both of these measurements are sensitive to temperature changes which is important considering that seawater temperatures could vary between - 2 °C and 35 °C (Hudson, Stanners and Hooper, 2013).

Even though seawater has a salinity of between 33 and 37 grams/dm^3, i.e. between 3.3 and 3.7%, it is known that an equivalent 3.5% NaCl solution is more aggressive towards carbon steel than natural seawater. This can be attributed to the additional ions found in natural seawater, such as Ca^{2+} and Mg^{2+}, forming argonite ($CaCo_3$) and brucite ($Mg(OH)_2$) calcareous deposits during corrosion of the steel (Möller, Boshoff and Froneman, 2006).

The relatively high and constant pH of sea water also contributes to its corrosive attribute. Surface seawater characteristically has pH values higher than 8 as a result of air-sea exchange and photosynthesis (Roberge, 2000), but can be as low as 7 in stagnant basins due to hydrogen sulphide produced by anaerobic bacteria.

2.3 Electrochemical Corrosion

Electrochemical corrosion occurs when four features are present in the reaction: an anode, a cathode, an electrolytic path for ionic conduction between the reaction sites and an electrical path for electron conduction between the reaction sites, as illustrated in Figure 2 (Kelly and Scully, 2003). Note that the anodic and cathodic site can be on the same piece of material.

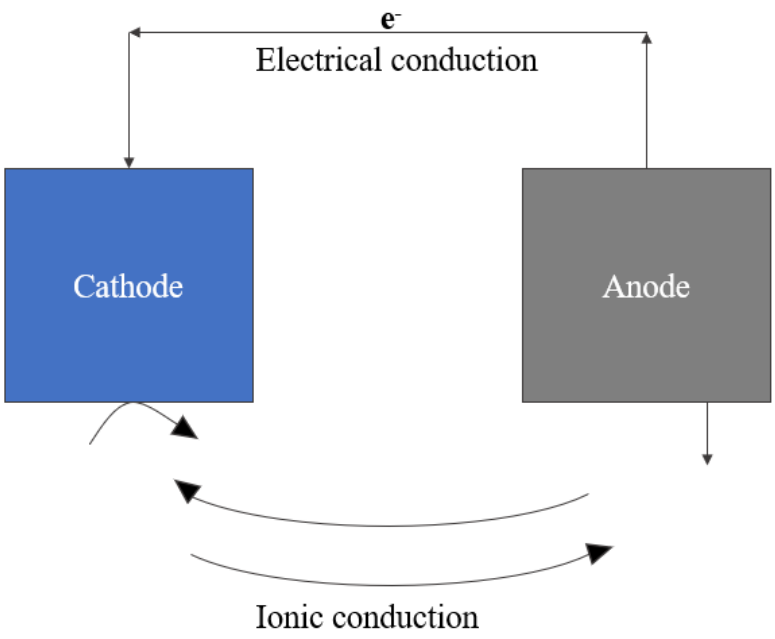

Figure 2: Schematic diagram of the four requirements for corrosion (Kelly and Scully, 2003)**.**

The anode is the electrode where oxidation takes place according to

$$M \rightarrow M^{n+} + ne^{-} \tag{2.3.1}$$

where M is the metal, $n+$ is the valence and ne^- the number of electrons taking part in the reaction. According to electrochemical theory, for an oxidation reaction to occur, a cathodic reduction reaction needs to take place at the same rate. Depending on the pH of a solution the cathodic reaction is either oxygen reduction:

$$O_2 + 4H^+ + 4e^- \rightarrow 2H_2O \tag{2.3.2}$$

for a basic solution. Or hydrogen reduction for an acidic solution:

$$2H^+ + 2e^- \rightarrow H_2(g) \tag{2.3.3}$$

2.3.1 Relation of Electrode Potential to Gibbs Free Energy

In electrochemistry, the free energy change of an electrochemical system can be written as:

$$\Delta G = -nFE_r \tag{2.3.4}$$

where n is the number of electrons involved in the reaction, F is Faraday's constant and E_r is the reversible potential difference at the solution-metal interface (Kelly and Scully, 2003). The reversible potential difference at a solution-metal interface is unique to each electrochemical reaction, just as each element has its own melting temperature (Kelly and Scully, 2003). For a reaction to occur spontaneously, the associate Gibbs free energy change needs to be negative as implied in Section 1.1.

The potential difference between two electrodes can be measured easily with a low impedance voltmeter, but directly measuring the potential of a single electrode is not possible (Roberge, 2008). The solution to this problem is the use of a reference electrode. A reference electrode introduces an additional interface that is in thermodynamic equilibrium, with a known, constant potential. Therefore, any potential change measured between the reference point and the electrode of interest is attributed to the latter (Kelly and Scully, 2003).

Historically, the hydrogen reaction's potential was chosen to be zero and all reaction potentials are reported against this reference point. The potential difference across a reversible cell between any electrode and a standard hydrogen electrode (SHE), operated at standard temperature and pressure, is called the standard electrode potential or the standard reversible potential of a cell, E_o. A list of reversible potentials under standard conditions is called an electromotive (emf)

series (Table 2). The relative potentials of reference electrodes that are more commonly used are shown in Figure 3.

The reversible potential of an electrode operated at non-standard conditions is dependent on the concentrations of the species involved in the reaction as well as temperature. This relationship is described by the Nernst equation:

$$E_r = E_o - \frac{RT}{nF} ln \frac{\{Ox\}^b \{H_2O\}^c}{\{Rd\}^a \{H^+\}^m} \quad (2.3.5)$$

Equation 2.3.5 is written for a reaction described by:

$$aRd + mH^+ + ne^- = bOx + cH_2O$$

where *R* is the universal gas constant, *F* is Faraday's constant and *T* is the solution temperature.

Table 2: Partial list of standard electrochemical reactions (Kelly and Scully, 2003)**.**

Reaction	Standard Potential (V vs. NHE)
$Au^{3+} + 3e^- = Au$	1.42
$Cl_2 + 2e^- = 2Cl^-$	1.36
$O_2 + 4H^+ + 4e^- = 2H_2O$	1.229
$Cu^2 + 2e^- = Cu$	0.34
$2H^+ + 2e^- = H_2$	0.000
$Ni^{2+} + 2e^- = Ni$	-0.23
$Fe^{2+} + 2e^- = Fe$	-0.44
$Zn^{2+} + 2e^- = Zn$	-0.763
$Al^{3+} + 3e^- = Al$	-1.706
$Mg^{2+} + 2e^- = Mg$	-2.375
$Na^+ + e^- = Na$	-2.712

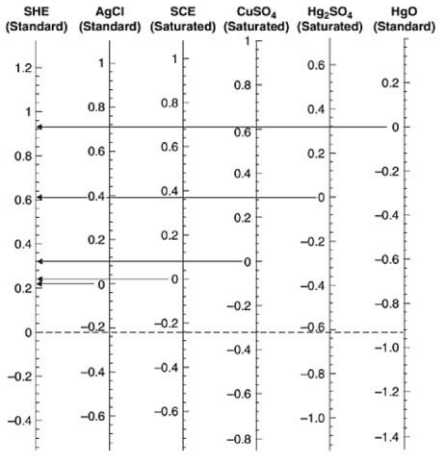

Figure 3: Graphical scheme comparing the relative potentials of the most common reference electrodes (Roberge, 2008)**.**

2.3.2 Polarization of Electrodes

Shifting the potential of an electrode away from its equilibrium potential is known as polarization. The degree of polarization (or polarization potential) is known as overpotential:

$$\eta = E - E_{ocp} \tag{2.3.6}$$

where E_{ocp} is the open circuit potential between the sample surface and the corroding environment. For positive overpotential values, the electrode of interest, known as the working electrode, is anodically polarized and in the other direction it is cathodically polarized.

The total polarization is composed of three distinct types of polarization; activation, concentration and ohmic drop (Flitt and Schweinsberg, 2005b). These three components are additive:

$$\eta_{total} = \eta_{act} + \eta_{con} + iR \tag{2.3.7}$$

Ohmic drop is a function of the environment resistivity. This is especially important when determining corrosion parameters such as polarization resistance in solutions that are not particularly conductive. Without compensating for large ohmic drops, the polarization resistance could be overestimated which could lead to an unrealistically low corrosion rate estimation.

When one of the reactions in the half-cell is controlled by the rate of charge transfer, the reaction is said to be under activation control (Roberge, 2000). Activation control is always present in the total overpotential even if it is not the

controlling component. Figure 4 shows the activation polarization curve of a hydrogen electrode.

The relationship between reaction rate and overvoltage is described by the Tafel equation:

$$\eta_{act} = \pm b \log\left(\frac{i}{i_o}\right) \tag{2.3.8}$$

where i is the rate of oxidation in terms of current density and b being the slope of the anodic and cathodic sections in the polarization curve known as the Tafel constants.

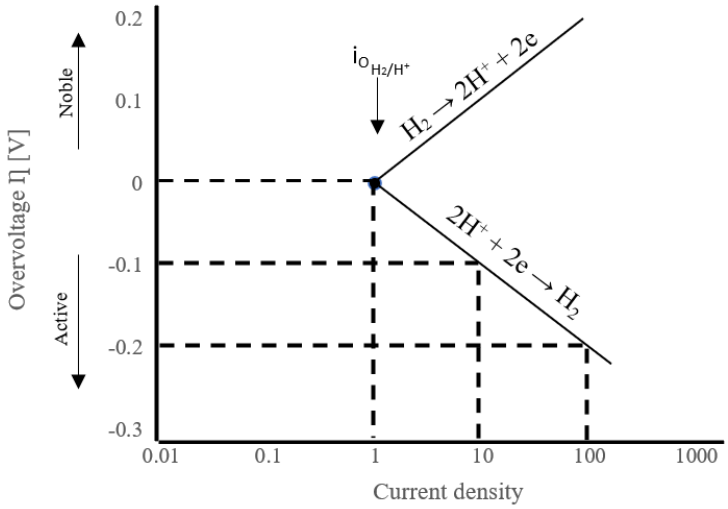

Figure 4: Activation-polarization curve of a hydrogen electrode (Fontana, 1987)**.**

Concentration or diffusion controlled polarization is when the rate determining step is limited by mass transport of species to the metal surface (Roberge, 2000). This phenomenon is present when a limited amount of active species is present in the solution, such as oxygen in aerated water. This phenomenon is illustrated in terms of the hydrogen evolution reaction in Figure 5. At high reaction rates, hydrogen ions are depleted close to the electrode surface. If the reduction rate is increased further, a limiting rate that is dependent on the rate of diffusion of hydrogen ions to the electrode surface is reached. This rate is called the limited diffusion current density, i_L, and it represents the maximum rate of reduction for a system. Figure 6 illustrates the concentration polarization curve of a reduction process. The concentration polarization is then given by Eq.2.3.8 (Li *et al.*, 2019).

$$n_{con} = \frac{2.303RT}{nF} \log\left(1 - \frac{i}{iL}\right) \tag{2.3.9}$$

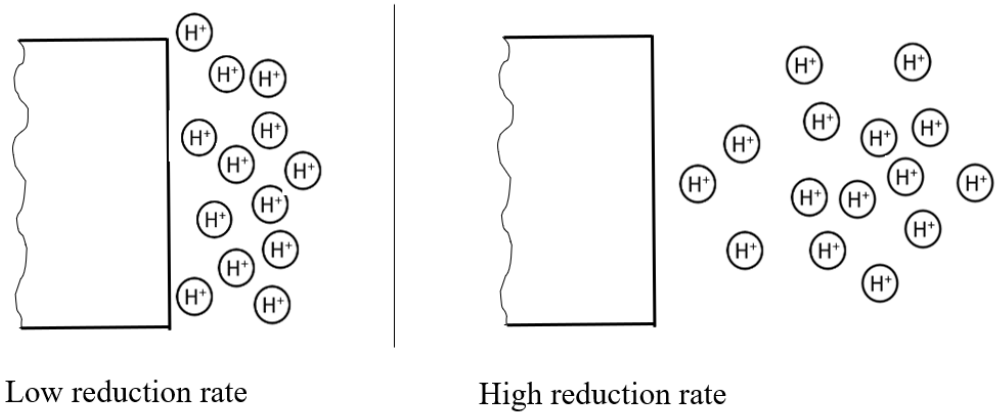

Figure 5: Concentration gradients during hydrogen evolution (Fontana, 1987)**.**

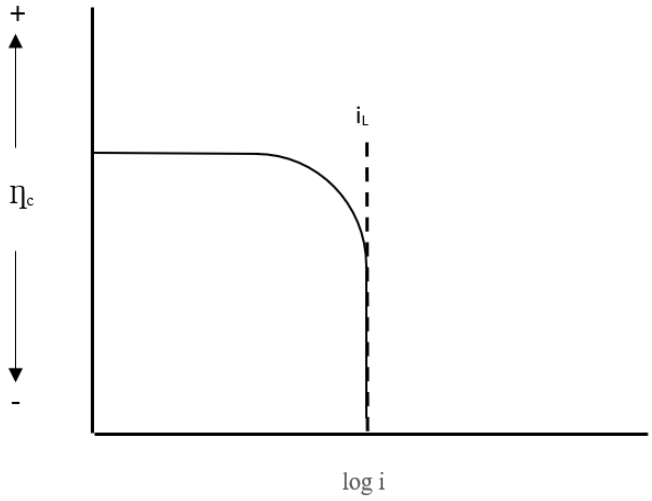

Figure 6: Concentration polarization curve for a reduction process (Fontana, 1987)**.**

Typically, in actual systems, both activation and concentration polarization are present with concentration polarization dominating at high values of negative overpotentials where the reaction rate approaches the limiting diffusion current and active polarization controlling low reaction rates as shown in Figure 7. For a cathodic process the total polarization can then be written as the sum of the active and concentration polarization components (Flitt and Schweinsberg, 2005).

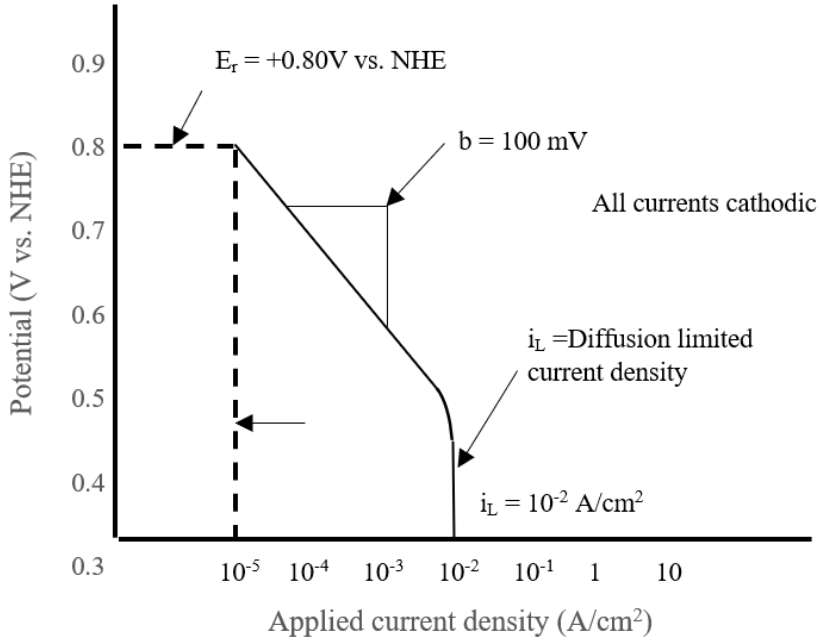

Figure 7: Schematic representation for an oxygen reduction reaction in a neutral solution (Kelly and Scully, 2003)**.**

2.3.3 Mixed Potential Theory

In order to analyse electrochemical polarization for systems containing more than one set of electrochemical reactions, mixed potential theory is needed. The first formal representation of mixed potential theory is attributed to Wagner and Traud (1938). This theory behind mixed potential theory is summarised in two hypotheses:

1. Any electrochemical reaction consists of two or more partial oxidation or reduction reactions.

2. There can be no net accumulation of charge in an electrochemical reaction.

From these two hypotheses, it can be deduced that the total rate of oxidation and the total rate of reduction must be equal for a corroding sample that is electrically isolated (Fontana, 1987). This is illustrated in Figure 8 which shows zinc submerged in hydrochloric acid.

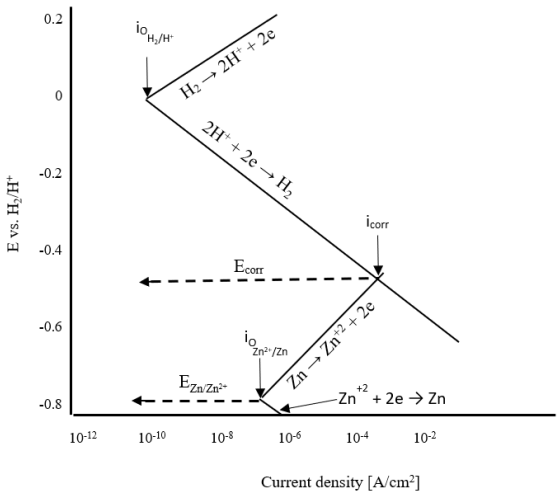

Figure 8: Electrode kinetic behaviour of pure zinc in acid solution (Fontana, 1987)**.**

The only point in the reaction where the total rate of oxidation is equal to the total rate of reduction is where the rate of zinc dissolution is equal to the rate of hydrogen evolution. No net charge is accumulated at this instance, for every zinc ion released, two electrons are utilized in the formation of a hydrogen molecule. This mixed potential state is called the corrosion potential, E_{corr}. The anodic (i_a) and cathodic (i_c) current densities at this point are equal and this current density is known as the corrosion current density, i_{corr}:

$$i_{corr} = i_a = i_c \tag{2.3.10}$$

2.3.4 Determination Corrosion Current Density

There are several established methods that can be used to determine i_{corr}. For the purposes of this project, the potentiodynamic polarization and polarization resistance techniques are discussed.

2.3.4.1 Potentiodynamic Polarization

For the potentiodynamic method, a large range of potentials are applied to a sample and the resulting current at the solution-metal interface is recorded. According to mixed potential theory, there can only be one potential at which the oxidation and reduction reactions are in equilibrium. This intersection can be identified by extrapolating the anodic and cathodic polarization curves to the corrosion potential in cases where only activation polarization is present. These extrapolated lines are known as Evan's lines and are illustrated in Figure 9. This technique is often referred to as the Tafel extrapolation method as the slopes of the Evans diagram are the Tafel slopes, b_a and b_c also referred to as the kinetic parameters of the system.

The difference between an Evans diagram and a polarization curve is that an Evans diagram represents reaction rates in terms of current density and a polarization curve represents measured current density. At the corrosion potential, the applied current:

$$i_{app} = i_a - i_c \tag{2.3.11}$$

is zero, since the half reactions are taking place at the same rate. Note that the rate of the reaction is not zero, but it cannot be measured directly because there is no net charge accumulated.

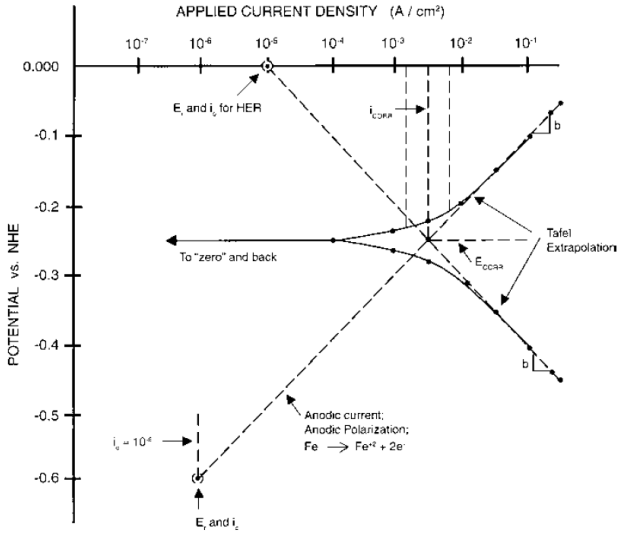

Figure 9: Illustration of an Evans diagram drawn on an experimental polarization curve (Roberge, 2008)**.**

For successful manual plotting of the Evans diagram, it is recommended that extrapolation should start at around 50 mV away from the E_{corr}. Another rule of thumb is that at least one of the anodic or cathodic polarization graphs should exhibit a linear behaviour on a semi-logarithmic scale for one decade of current density (Kelly and Scully, 2003). If this cannot be achieved, alternative methods need to be used to verify the corrosion rate. Nonlinear curve fitting algorithms in electrochemical data processing programs eliminate much of the guesswork associated with this method, but it is still good practice to verify results manually.

The presence of concentration polarization complicates the determination of i_{corr} because a limited diffusion current is present in the polarization curve. For cases where one of the reactions is under purely diffusional control, the corrosion current will be equal to the limited diffusion current. When the effects of activation and concentration polarization is similar in magnitude, the reaction is said to be under mixed control (ASTM International, 2008).

Exposing a sample to a large range of potentials could be disadvantageous for several reasons. Firstly, the sample surface is often destroyed as a result of high reaction rates at large overpotentials. Pitting, crevice corrosion and passivation could take place far away from E_{corr} which would make it very difficult to identify Tafel regions if they are present. Furthermore, potentiodynamic tests can be very lengthy as the scan rate needs to be relatively slow to prevent charging effects on the sample surface (Fischer *et al.*, 2019).

2.3.4.2 Polarization Resistance Technique

Most of the disadvantages associated with the potentiodynamic method is overcome by the polarization resistance technique. It is often used in field applications as the test is considered non-destructive and can be performed relatively quickly.

The linear polarization resistance (LPR) technique assumes that the applied current-voltage curve close to the corrosion potential, where overpotential switches polarity, is linear when plotted on a linear scale as shown in Figure 10. A curve is typically plotted for ±20 mV around the corrosion potential. A linear section very close to the corrosion potential is identified and a polarization resistance, R_p, is calculated according to Ohm's law:

$$R_p = \frac{\Delta E}{\Delta i_{app}} \tag{2.3.12}$$

The polarization resistance of a material in a solution can be used to determine the corrosion current density using the kinetic parameters of the corroding system according to the Stern-Geary equation:

$$R_p = \frac{\Delta E}{\Delta i_{app}} = \frac{b_a b_c}{2.303 i_{corr}(b_a + b_c)} \tag{2.3.13}$$

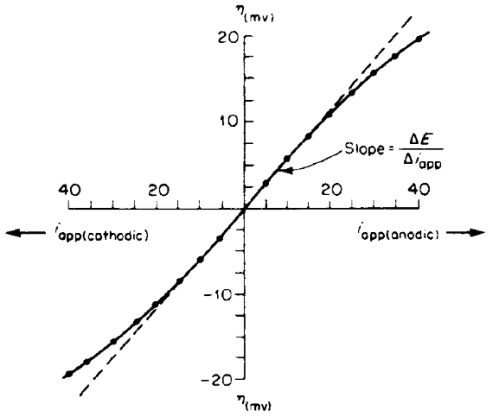

Figure 10: Applied current-voltage curve showing linearity around the corrosion potential (Fontana, 1987)**.**

Note that prior knowledge of the Tafel slopes are required. These slopes are often guessed from experience to yield a rough estimation of corrosion rate.

Even though the LPR technique is well established, it has been criticised by several researchers for the accuracy of its application in inappropriate corrosion situations such as galvanic corrosion (Angst and Büchler, 2015) or erroneous application of the technique in general. Mansfeld (1973) showed that unequal b_a and b_c values leads to a curvature in the polarization resistance curve (Figure 11). Using the LPR technique to determine *Rp* in this case could lead to large errors in corrosion rate determination. Mansfeld and Oldham (1973) developed a graphical technique that could accurately determine corrosion currents without prior knowledge of the Tafel slopes that was not sensitive to the curve in polarization around the corrosion potential. Mansfeld later published a technique that could be implemented numerically (Mansfeld, 1973). Instead of assuming the curve to be linear, Mansfeld proposed a four-step method, as described on page 17, to determine i_{corr} in which the Tafel slopes and polarization resistance are also determined.

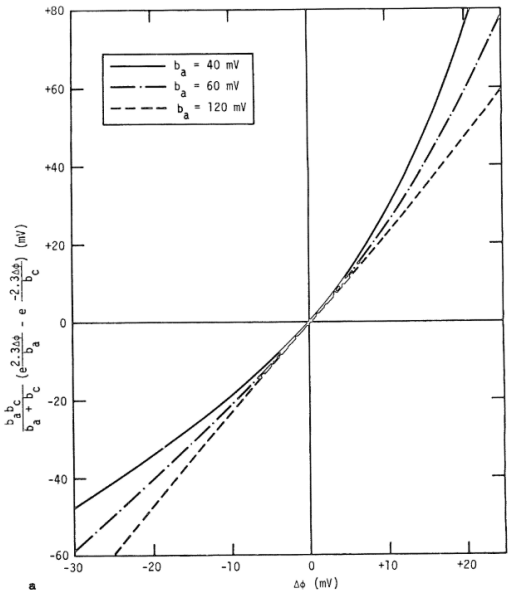

Figure 11: The effect of unequal Tafel slopes on the linear behaviour of a polarization curve, plotted for b_c=120 mV (Mansfeld, 1973)**.**

Step 1: Determine the polarization resistance by drawing a tangent to the polarization resistance curve at the corrosion potential:

$$\left(\frac{di}{dE}\right)_{E_{corr}} = R_p^{-1} \tag{2.3.14}$$

Step 2: Combine the Buttler-Volmer equation:

$$i = i_{corr}\left(e^{\frac{2.3(E-E_{corr})}{b_a}} - e^{\frac{-2.3(E-E_{corr})}{bc}}\right) \quad (2.3.15)$$

and Eq.2.3.13 to eliminate the i_{corr} variable:

$$2.3R_p i = \frac{b_a b_c}{b_a + b_c}\left(e^{\frac{2.3(E-E_{corr})}{b_a}} - e^{\frac{-2.3(E-E_{corr})}{bc}}\right) \quad (2.3.16)$$

Plot the left-hand side of equation 2.3.16 with experimental data against overvoltage with E_{corr} being the reference point.

Step 3: Theoretically, some combination of Tafel slopes on the RHS of Eq.2.3.16 will fit the experimental data that was plotted in Step 2. These values can be approximated by iteration or curve fitting software.

Step 4: The i_{corr} is calculated with the Tafel slopes and R_p values determined in the previous steps.

2.4 Electrochemical Instrumentation

Performing polarization tests and producing the various parameters discussed in the preceding sections require specialised equipment that allows for accurate, reproducible measurements. Figure 12 shows a schematic drawing of a typical test set-up. The set-up consists of a potentiostat which is an electronic device which controls a three-electrode cell. A potentiostat regulates the power output to the investigated electrode, referred to as the working electrode, by controlling the voltage output accurately. A current-controlled variant of this instrument is called a galvanostat. The functioning of these devices are quite simple, and can therefore be assembled by a researcher if costs of a purpose-built machine is prohibitive, but the accuracy of a research-grade potentiostat is difficult to achieve in a "home-made" device (Rowe *et al.*, 2011).

An auxiliary/secondary electrode, usually a carbon rod or platinum electrode, is placed in the cell to act as the cathode when the working electrode is acting as the anode or vice versa. The third electrode is the reference electrode which, as discussed in Section 2.3.1, is used to monitor the working electrode potential. Placing the reference electrode in a salt bridge or Luggin-Haber capillary tube allows for measurement close to the working electrode surface, which will minimise ohmic drop without shielding the working electrode from current flow. Additionally, the capillary tube is often fitted with a porous glass or ceramic frit that allows for ionic conduction but prevents contamination of the working solution or reference electrode. The low leak rate of a frit allows for placement of

the reference electrode above the working solution level. Data is stored on a standard computer that also acts as interface to the potentiostat (Roberge, 2008).

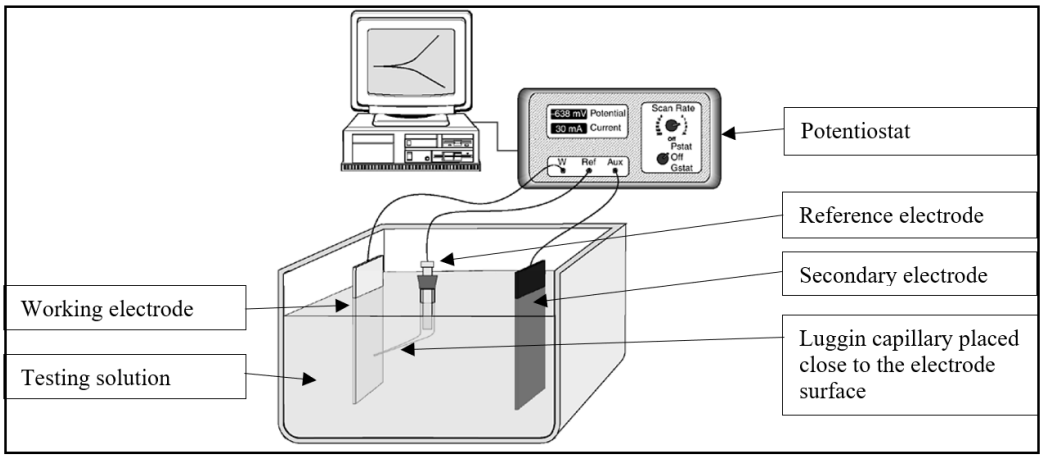

Figure 12: Electrochemical instrumentation (Roberge, 2008)**.**

2.5 Corrosion Rate Expressions

2.5.1 Mass Loss

The simplest method for monitoring and predicting corrosion rates is exposure tests. This method is relatively inexpensive and can yield very accurate results. Metal coupons with a known weight and size are placed in the corroding environment for a certain period of time. Following exposure, corrosion product is removed by chemical, electrolytic or mechanical methods. Samples are weighed again to determine the mass lost to corrosion (Fontana, 1987). Mass loss is converted to a penetration rate by taking into account the original area of the metal coupon as well as the density of the sample:

$$CR = \frac{m}{AT\rho} \tag{2.5.1}$$

where *CR* is the predicted corrosion rate, *m* is the mass lost during the corrosion period, *A* is the area exposed to the corroding environment, *T* is the testing time and ρ is the density of the material being investigated.

The biggest disadvantage of this method is that exposure periods must be long enough to obtain measurable corrosion rates. It is also important to note that the effect of the cleaning procedure should be accounted for in the mass loss calculation:

$$m = m_{measured} - m_{cleaning} \tag{2.5.2}$$

2.5.2 Electrochemical Corrosion Rates

Electrochemical techniques are used as an alternative to mass loss as they permit rapid corrosion rate measurements, can be used to monitor in-service equipment and provide valuable electrochemical information about the corrosion process. These methods are often used to measure very low corrosion rates accurately.

Faraday's laws of Electrolysis are crucial in computing corrosion rates as they describe the effect of electrical charge on mass changes and material loss rates.

Faraday's first law states that the mass, *m*, of an element discharged or liberated at an electrode is directly proportional to the charge, *Q*, passed through that electrode. Which is described mathematically as

$$m \, \alpha \, Q \tag{2.5.3}$$

Faraday's second law of electrolysis states that, if the same amount of charge is passed through different electrodes, the mass, m, discharged at each electrode will be proportional to the equivalent weight of each of the electrodes.

The equivalent weight of a pure element is given by:

$$EW = \frac{W}{n} \tag{2.5.4}$$

where *W* is the atomic weight of the element and *n* is the valency of the atom.

Equivalent weight becomes more difficult to compute for non-pure materials. According to ASTM G102-89 (Standard Practice for Calculation of Corrosion Rates and Related Information from Electrochemical Measurements), the *EW* for an alloy is written as

$$EW = \frac{1}{Q} \tag{2.5.5}$$

where *Q* is the electron equivalent of 1g of an alloy described by

$$Q = \sum \frac{n_i f_i}{W_i} \tag{2.5.6}$$

where n_i, f_i, and W_i is the valence, mass fraction, and atomic weight of the i^{th} element in the alloy respectively.

Combining Faraday's laws with an electrochemical reaction of known stoichiometry permits us to form a single equation that relates mass loss per unit area to charge density (Kelly and Scully, 2003):

$$\Delta m = \frac{q(W)}{nF} \tag{2.5.7}$$

where F is Faraday's constant. Taking the time derivative of Eq 2.5.7 allows the mass loss rate to be related to dissolution current density.

$$\dot{m} = \frac{i_{corr}(W)}{nF\rho} \tag{2.5.8}$$

For design purposes, it would be advantageous to describe a corrosion rate as a penetration rate (length/time) rather than mass loss with time. Some common units are mils per year (*mpy*) or millimetres per year (mm/*y*). ASTM G102 (2008) states that uniform penetration rate in SI units can be calculated as:

$$CR = \frac{K_1 i_{corr} EW}{\rho} \tag{2.5.9}$$

where K_1 = 3.27 x 10^{-3} mm g/µA cm yr.

2.6 Ultrasonic Thickness Measurement

Measuring wall thickness of large structures or objects that are only accessible from one side, such as pipes or pressure vessels, is a challenge. One solution to this problem is the use of an ultrasonic through thickness gauge.

Ultrasonic thickness measurement works by emitting an ultrasonic pulse through a material using a piezoelectric cell and measuring the time for an echo pulse to return to a measurement sensor (*45MG Ultrasonic Thickness Gauge User's Manual*, 2016) (Figure 13). With the speed of sound through the sample known, the thickness can be determined as:

$$t = \frac{cs}{2} \tag{2.6.1}$$

where t is the thickness of the measured material, c is the velocity of sound through the sample and s is the time taken to travel through the material and back.

A through thickness gauge is calibrated to a specific material by measuring the time needed for a pulse to return to the transducer through a sample with a known thickness. The velocity of sound through the sample is then calculated.

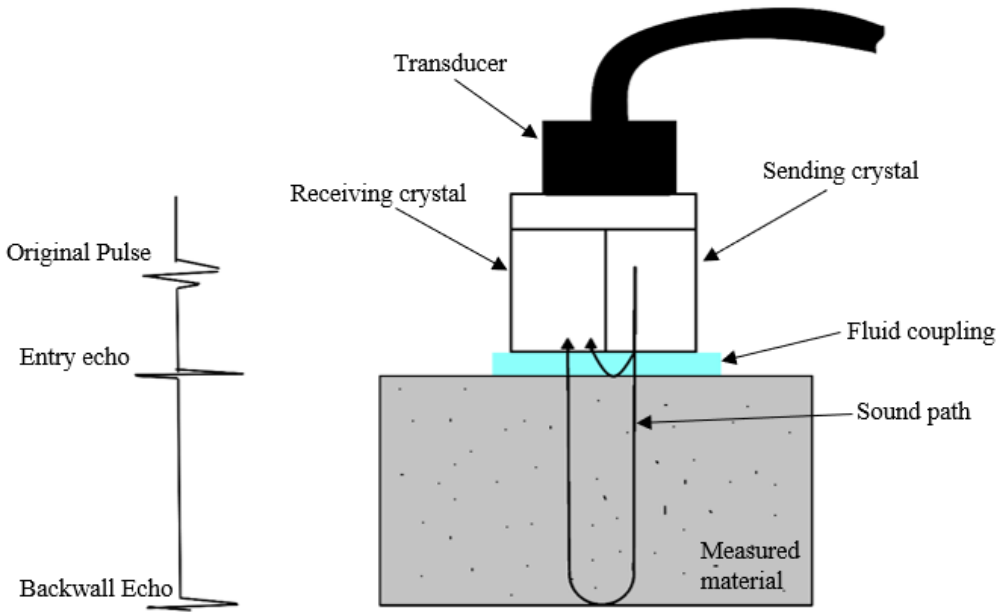

Figure 13: Diagram showing ultrasonic wave path during through thickness measurement.

2.7 Microstructural Characterisation of HY-80 Steel

HY-80 is classified as a high strength low alloy (HSLA) steel that is designed to be stronger, more durable and have better corrosion resistance than conventional carbon steels. Originally developed in the 1960s for submarine and naval ship construction (Oktadinata and Winarto, 2019), its many attractive properties, such as good formability, corrosion resistance, and weldability, lends itself to critical applications such as high-pressure pipelines and pressure vessels. As the name suggests, HY-80 has a minimum yield strength of 80 ksi or 552 MPa. The mechanical properties of HY-80 are listed in Table 3 according to the specifications in the MIL-S-16216K specification (Military specification: Steel Plate, Alloy, Structural, High Yield Strength (HY-80 and HY-100), 1987).

Table 3: Mechanical properties of HY-80.

Mechanical property	Nominal thickness	
	19 mm and under	Over 19 mm
Yield strength [Mpa]	552 – 690	552 – 686
Minimum elongation [%]	19	20

Table 4: Composition of HY-80.

Alloying element	C	Mn	P	Ni	Cr	Mo	Cu
Mass percentage	0.13-0.18	0.10-0.40	<0.025	2.00-3.25	1.00-1.80	0.2-0.3	<0.25

The composition of HY-80 is reported in Table 4. Nickel is typically added to steels to improve toughness and ductility (Budynas and Nisbett, 2015), while the wear resistance and hardness are attributed to the addition of Chromium. Minor elements such as Titanium and Vanadium are added for grain refinement. Considering that submarines are mostly immersedThe addition of Mn, Al, Si, Mo and Cr is favourable in terms of uniform corrosion resistance for low alloy steels depending on immersion time as seen in Table 5 (Hudson, Stanners and Hooper, 1994).

Table 5: Effect of alloying elements on marine corrosion resistance (Hudson, Stanners and Hooper, 1994).

Corrosion type	**Environment**	**Favourable**	**Neutral**	**Unfavourable**
Uniform corrosion	Immersion	Mn Si Al Mo (t > 4 years) Cr (t ≤ 4 years)	Ni	P S Cu Mo (t ≤ 4 years) Cr (t > 4 years)
	Tidal and splash zone	P	Cu, Cr, Ni	
	Marine atmosphere	P, Si, Mn, Cu, Cr, Ni, Mo, V, Ti		
Local corrosion (especially pitting)	Immersion		Cu, Cr	Ni
	Tidal and splash zone	Cu	Ni	Cr

The microstructure of quenched and tempered HY-80 is characterised as a tempered bainitic martensitic duplex structure (P. Deb and Challenger, 1984; Oktadinata and Winarto, 2019). Figure 14 shows a micrograph of a typical HY-80 plate. Guo and colleagues (2015) showed that the microstructure of a low-alloy steel affects the corrosion rate of the steel. It is therefore important to investigate microstructural changes in the steel in order to explain any changes in corrosion behaviour.

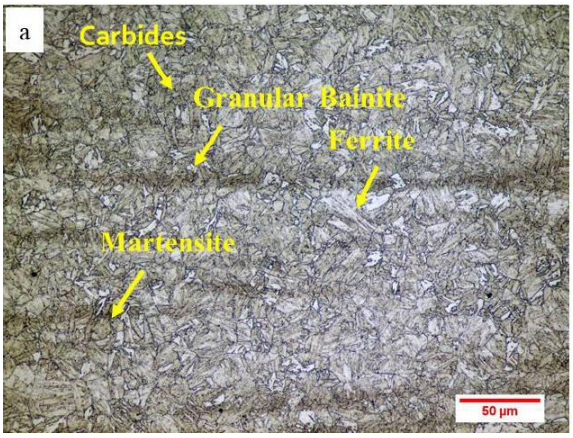

Figure 14: Typical microstructure of HY-80 steel (Oktadinata and Winarto, 2019)**.**

Extensive research has been conducted around the failure of HY-80 as a result of improper welding procedures. Steep temperature gradients in the heat affected zone (HAZ) could lead to cracking as a result of hydrogen embrittlement and the formation of untempered martensite. It is interesting to note that the USS Thresher (SSN-593), that sank in 1963 during depth testing, had a pressure hull made of HY-80. Although the cause of the incident is not yet known, it is speculated that material defects due to welds led to its sinking.

2.8 Submarine Pressure Hull Analysis

2.8.1 Analytical analysis of collapse pressure

A large portion of a submarine's weight can be attributed to that of the pressure hull. Table 6 shows the weight distribution of an SSK diesel electric submarine with its pressure hull weight accounting for about half of the "Structures" weight.

Table 6: Weight distribution of an SSK diesel submarine (Burcher and Rydill, 1995)**.**

Component	Weight (%)	Space (%)
Payload	9	28
Structures	43	-
Main and Auxiliary Machinery	35	56
Accommodation and Outfit	4	11
Stores	1	5
Permanent Ballast	8	-

In order to limit its weight, a submarine pressure hull needs to be designed efficiently to utilize the strength of the hull material to its maximum potential (Burcher and Rydill, 1995).

The ideal pressure vessel geometry would be that of a sphere as it will experience equal stresses and strains throughout the shell according to:

$$\sigma_c = \frac{Pr}{t} \tag{2.8.1}$$

where σ_c is circumfrerential stress, P is the applied pressure, r is the hull radius and t the wall thickness of the shell. This shape, however, is very difficult to manufacture, not hydrodynamic, and it is difficult to utilise the internal volume efficiently. A cylindrical structure with domed enclosures at either end is not as efficient structurally, as the stress in the longitudinal direction is half that of the circumferential stress:

$$\sigma_l = \frac{Pr}{2t} \tag{2.8.2}$$

where σ_l is the longitudinal stress. However, from a hydrodynamic and volumetric utilisation efficiency point of view, this shape is much better. Furthermore, it is much easier to manufacture as hull plates are rolled in one direction and welded together (Burcher and Rydill, 1995).

For an unstiffened, internally pressurised cylinder, cylinder failure would occur when the circumferential stress, σ_c, approaches the yield stress of the material and the maximum allowable pressure is then described by the boiler pressure (Burcher and Rydill, 1995), P_b:

$$P_b = \frac{\sigma_y t}{r} \tag{2.8.3}$$

where σ_y is the yield stress of the steel. Unfortunately, this is not the case for externally pressurised cylinders as buckling along the length of the cylinder would occur long before the yield stress of the hull material can be reached. The predominant mode of failure for an unstiffened cylinder is that of an oval, in which the cylinder is flattened under the external pressure (Figure 15). Depending on the original out of circularity errors, material can buckle outward or inwards in many different mode shapes (Burcher and Rydill, 1995). To prevent premature elastic buckling, externally pressurised cylinders, such as submarines, are internally ring stiffened.

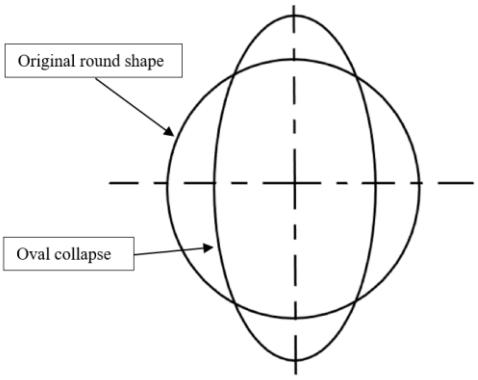

Figure 15: Cross section of structure - oval failure mode.

The addition of stiffeners along the length of a shell increases the complexity of stress and strain experienced by the shell. The strain will vary along the length of the shell with a maximum strain being reached at the midpoint between stiffeners and a minimum over a stiffener. This variable strain pattern results in bending strains in the longitudinal direction.

Over a stiffener, the outermost fibres of the shell plating are subjected to a circumferential stress, which is reduced by the stiffening ring, as well as tensile bending and axial compression in the longitudinal direction. The innermost fibres are subjected to compressive bending and axial loading which can lead to yielding of the material.

At the midpoint between stiffeners, shell plating will typically experience higher circumferential loading than those experienced at stiffeners, longitudinally compressive bending and compressive axial loading will be present. The inner fibres will be at a reduced stress state with bending and axial loading being in opposite directions. End loading on radially displaced shell plating will induce an additional bending moment which could result in failure where the material is folded up in between stiffeners. This failure is described as concertina mode (Figure 16) or interframe collapse (Burcher and Rydill, 1995), which is the preferred mode of failure for submarines (MacKay, Van Keulen and Smith, 2011).

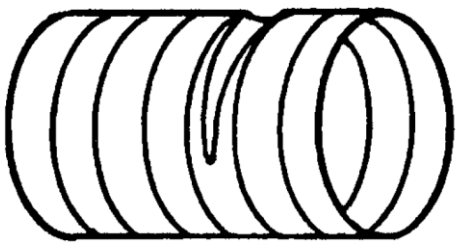

Figure 16: Partial concertina mode failure of a stiffened cylinder (Burcher and Rydill, 1995)**.**

The stress-strain behaviour of a ring stiffened cylinder is further complicated by the introduction of out of circularity imperfections which will allow for buckling at a lower critical load than described for the above cases.

Another countermeasure to overall collapse is the introduction of heavier stiffeners, known as deep frame stiffeners or transverse bulkheads to increase radial stiffness, which effectively reduces the length of possible overall collapse modes.

2.8.2 Submarine Design Formulas

Even though it is technically possible to determine the collapse pressure of a submarine pressure hull analytically, small deviations in geometry and material properties can have a large impact on actual collapse pressure. Interframe collapse is therefore predicted by relating analytically derived buckling and yield models, known as the submarine design formulas (SDF), to experimental data (MacKay, Van Keulen and Smith, 2011). Figure 18 shows an empirical design curve as used in the PD5500 standard (Specification for unfired fusion welded pressure vessels, 2009) standard. The curves are plotted as experimentally obtained collapse pressure against the elastic interframe collapse load, P_m, with both axes normalised with respect to the yield pressure of the hull plating between stiffeners, P_y. The associated characteristic pressures are calculated according to the PD5500 standard.

P_y describes failure where the mean circumferential stress in the plating between stiffeners is large enough to cause yielding in the material:

$$P_y = \frac{\sigma_y t}{r(1-\gamma G)} \tag{2.8.4}$$

where σ_y is the yield strength of the steel, t is the wall thickness of the shell plating and γ and G are stiffener parameters.

The first parameter, γ, is calculated by Eq. 2.8.5.

$$\gamma = \frac{A\left(1-\frac{v}{2}\right)}{(A-t_w t)(1+B)} \tag{2.8.5}$$

where v is Poisson's ratio and t_w the stiffener thickness. A is the modified ring frame area (Figure 17) in terms of the effective length of the ring-frame area:

$$L_{eff} = \frac{1.556\sqrt{rt}\dfrac{\cosh(\alpha L_s) - \cos(\alpha L_s)}{\sinh(\alpha L_s) + \sin(\alpha L_s)}}{\left\{\left(1 + 0.5n^4\left(\frac{t}{r}\right)^2\right)^{0.5} + \left(\frac{n^2\left(\frac{t}{r}\right)}{\sqrt{3}}\right)\right\}^{0.5}} \tag{2.8.6}$$

where L_s is the stiffener spacing, n is the number of circumferential lobes in the analysed mode and

$$\alpha = \frac{1.285}{\sqrt{rt}} \tag{2.8.7}$$

B is calculated as:

$$B = \frac{\dfrac{2t(\cosh(\alpha L_s) - \cos(\alpha L_s))}{\sinh(\alpha L_s) + \sin(\alpha L_s)}}{\alpha(A + t_w t)} \tag{2.8.8}$$

The second stiffener parameter, G is given by

$$G = \frac{2\left(\sinh\left(\frac{\alpha L_s}{2}\right)\cos\left(\frac{\alpha L_s}{2}\right) + \cosh\left(\frac{\alpha L_s}{2}\right)\sin\left(\frac{\alpha L_s}{2}\right)\right)}{\sinh(\alpha L_s) + \sin(\alpha L_s)} \tag{2.8.9}$$

The Von Mises buckling pressure is given in terms of the variables as mentioned before and Young's modulus, E_y:

$$P_m = \frac{E_y t J}{r\left(n^2 - 1 + \left(\frac{\pi r}{L_s}\right)^2\right)} \tag{2.8.10}$$

$$J = \left\{\left[n_i^2\left(\frac{L_s}{\pi r}\right)^2 + 1\right]^{-2} + \frac{t^2}{12r^2(1 - v^2)}\left[n_i^2 - 1 + \left(\frac{\pi r}{L_s}\right)^2\right]^2\right\} \tag{2.8.11}$$

The overall elastic collapse pressure is calculated using the Bryant equation (Cho *et al.*, 2018):

$$Pn = \frac{(n_o^2 - 1)EI_c}{r^3 L_s} + \frac{\dfrac{Et}{r}}{\left(n_o^2 - 1 + \frac{1}{2}\left(\frac{\pi r}{L_c}\right)^2\right)\left(n_o^2\left(\frac{L_c}{\pi r}\right)^2 + 1\right)^2} \tag{2.8.12}$$

where *Ic* is the second moment of inertia of the combined stiffener-frame area as shown in Figure 17 and *Lc* is the total length of the investigated cylinder section.

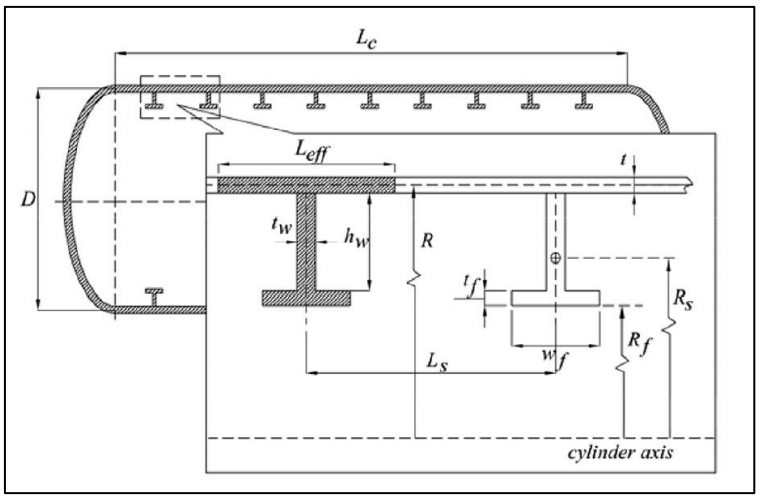

Figure 17: Ring stiffened cylinder showing the variables needed for calculation of the submarine design formulas.

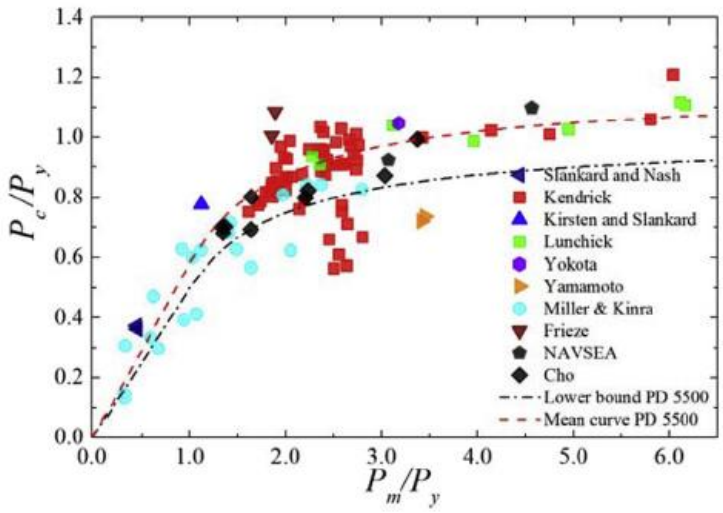

Figure 18: Empirical design curve for interframe collapse (Cho *et al.*, 2018).

2.8.3 Nonlinear Finite element analysis of ring-stiffened cylinders

Analytical predictions of collapse pressures are used in the initial design stage of submarine design. These predictions are generally conservative, (Smith, Macadam and MacKay, 2015) and based on ideal structures. The use of finite element analysis allows for the incorporation of material and geometric imperfections, assessment of in-service damage as well as more complex loading scenarios.

2.8.3.1 Modelling of imperfections

Out of circularity (OOC) imperfections are applied to mesh nodes to perturb the radial position of the hull plating. Ideally, these perturbations are based on actual measured out of circularity data of pressure vessels. This is achieved by fitting the measured imperfections to a Fourier series and applying the series to the hull plating (Cerik and Cho, 2013). In the absence of real data, idealised patterns based on linear elastic buckling modes are applied to the nodal positions (Gannon, 2010; MacKay, Van Keulen and Smith, 2011). The maximum amplitude of OOC is typically taken as 0.5% of the hull radius (MacKay *et al.*, 2010; Cerik and Cho, 2013).

2.8.3.2 Boundary Conditions

Boundary conditions were approached in several ways in the assessed literature. The literature is mostly concerned about the accuracy of numerical models as compared to experimentally obtained collapse pressures. This means that one end of the investigated cylinder was typically fully clamped, and the other end only allowed to move axially. For actual submarine models, symmetry boundary conditions were applied to the end of a compartment (Smith, Macadam and MacKay, 2015) or, when a symmetrical plane was identified in the length of one compartment, applied to the midplane (Gannon, 2010). Bulkheads were not explicitly modelled by Gannon (2010) or Smith (2015), but their effects on the stiffness of the whole structure was modelled by assuming that the bulkhead was perfectly rigid and, therefore, the bulkhead nodes were completely constrained radially. Other symmetry planes were utilised to reduce model size, but this constraint limits the out of circularity modes that can be applied to the structure.

2.8.3.3 Material Non-Linearity

Material non-linearity needs to be considered as pressure hulls are designed to fail in the plastic region. It is therefore important to incorporate actual stress-strain curves in the numerical model (MacKay, Van Keulen and Smith, 2011), especially if post-buckling information needs to be captured. Post buckling information can give valuable insights on the mode of failure

2.8.3.4 Solution Procedures

Dynamic analysis is shown to be unnecessary, (MacKay, Van Keulen and Smith, 2011) unless post buckling information is required. Using nonlinear static methods in which loads or displacements are applied incrementally are similar to the time-stepping procedures in dynamic analysis and is therefore referred to as “pseudo-static” (MacKay, Van Keulen and Smith, 2011).

2.8.4 Relating Operating Pressure to Density

The pressure at depth in seawater is a nonlinear function of density which varies with depth and temperature. Yang (2017) presented an experimentally obtained depth-density curve for seawater in the South China Sea that was subsequently fitted with a polynomial curve.

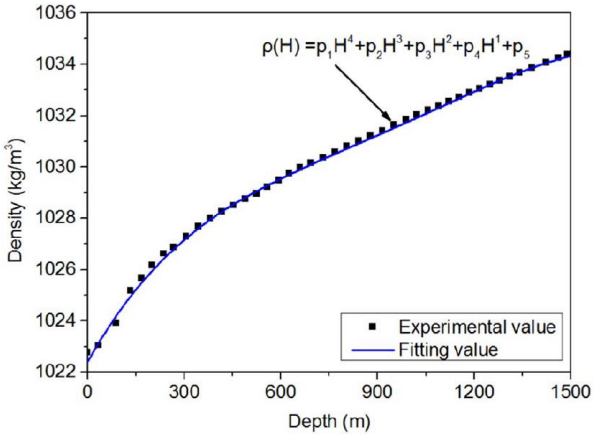

Figure 19: Density of seawater at certain depths (Yang *et al.*, 2017)**.**

This curve is utilised to estimate the density of seawater at set depths. These densities could then be related to a cumulative pressure increase using a Matlab code.

3 Experimental Procedure

In this chapter, the experimental procedures for this study are presented. Figure 20 shows the research methodology with the experimental work divided into three categories, namely mechanical property analysis, corrosion analysis and microstructural characterisation.

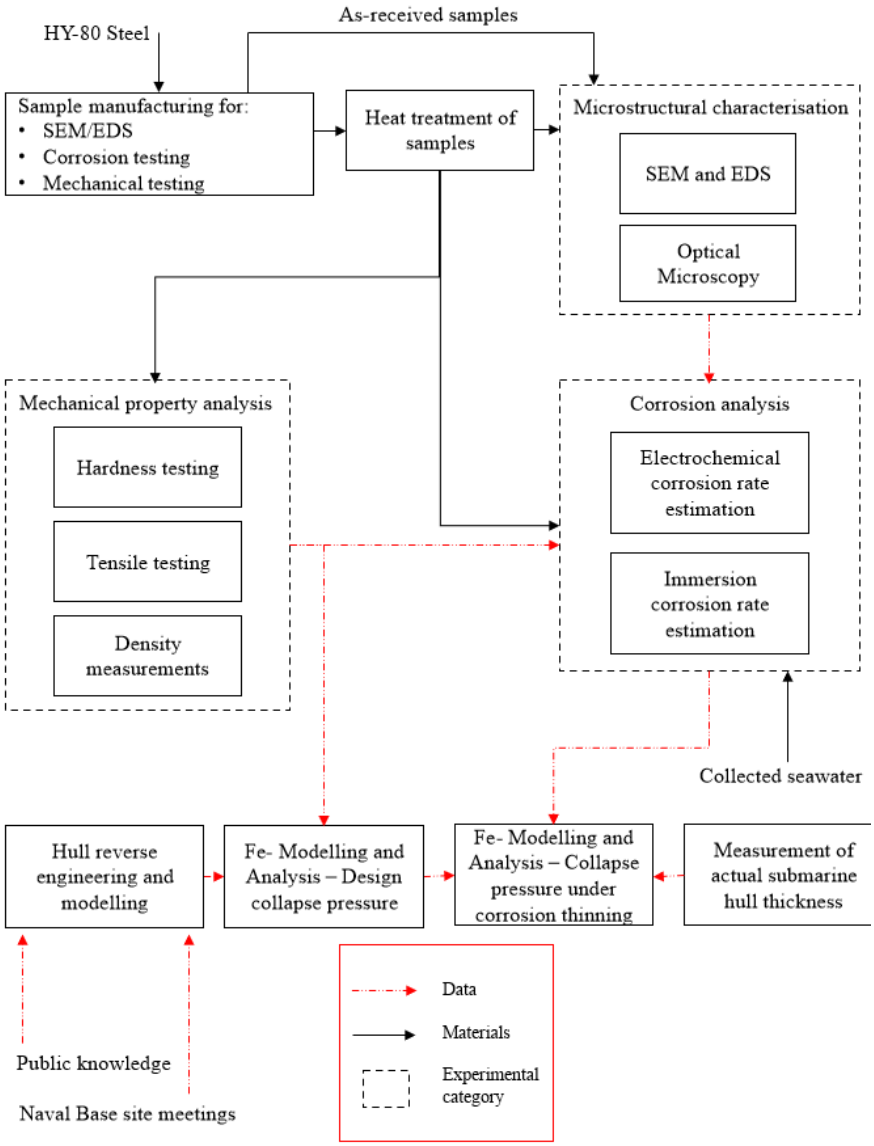

Figure 20: Project methodology showing experimental categories.

3.1 Materials

3.1.1 Steel

The South African Navy supplied a section of HY-80 steel for analysis. Unfortunately, the manufacturer is unknown, and no material certificate was provided, therefore the relevant material properties had to be determined to investigate the effect of heat treatment on the mechanical and corrosion properties. It is assumed that the submarine hull is stress relieved after rolling hull plating and welding and therefore the original condition of the material is altered. For these reasons as-received and heat treated samples were tested.

All samples, except for immersion corrosion samples, were manufactured by wire electrical discharge machining (WEDM), so that the samples were as geometrically accurate as possible and to ensure that the original material condition was not changed by excess heat input from processes such as sawing or milling. Table 7 contains the dimensions and quantities of the corrosion, metallographic and the tensile specimens.

Table 7: Steel Sample Specifications

Sample Type	Material Condition	Number of samples	Sample Size (mm)
Electrochemical	As-received	4	12x12x6
	Heat treated	4	
Metallographic	As-received	1	12x12x6
	Heat treated	1	
Immersion tests	Heat treated	4	50x23x4
	As-received	4	
Tensile specimens	As-received	5	As per ASTM E8/E8M-15a
	Heat treated	5	

3.1.2 Heat Treatment

In the absence of actual specifications on heat treatment procedures used in submarine manufacture, a reasonable estimation of post manufacture heat treatment was made based on the minimum stress relief temperature listed in the MIL-S-16216K standard. A similar heat treatment was investigated by (Lins Junior *et al.*, 2014) as a post weld heat treatment.

The furnace heating curve is shown in Figure 22. Samples were placed in the furnace and allowed to heat up to 590°C, which is the minimum stress relief temperature as set in the MIL-S-16216K standard. The furnace was held at this temperature for 90 minutes, after which samples were removed and allowed to cool down in air.

Figure 21: Gollenkamp 3500 W electric muffle furnace size 2.

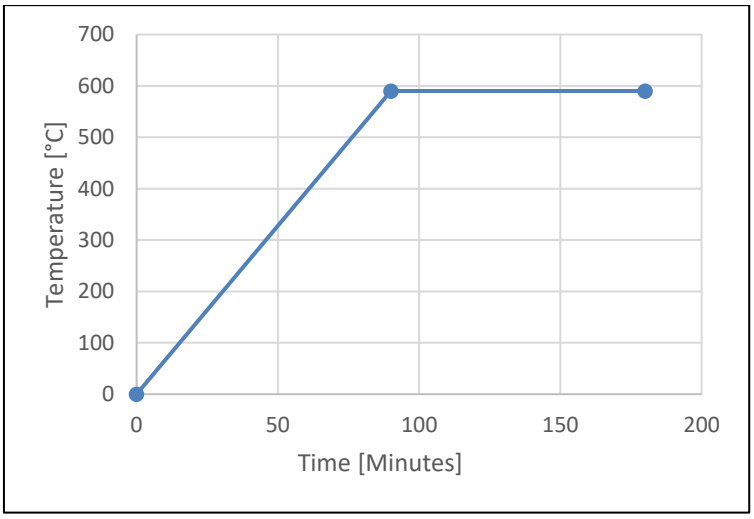

Figure 22: Heat treatment curve with a maximum average of 590°C.

3.1.3 Collected Seawater Analysis

Seawater was collected from Boulders Beach in Simon's Town, South Africa (the vicinity of SAN where the submarine hulls in this study are based) and stored in clean plastic containers for up to 7 months. It was noted that storing the water may lead to changes in the chemistry and biological makeup of the water.

The collected seawater composition and properties are shown in Table 8. All water composition tests were performed by Integral Laboratories. Results showed that the conductivity of the collected seawater, which is the reciprocal of resistivity, was 5440 mS/m. Ohmic drop as discussed in Section 2.3.2 is therefore

minimal especially when measurements are taken close to the sample surface. Salinity was calculated as 33.1 g/kg using Eq. 2.2.1 which is typical for seawater according to the literature (Rowlands, 1994).

Table 8: Collected seawater composition and properties, as per tests conducted by Integral Laboratories.

Physical parameters	**Unit**	**Quantity**
Alkalinity – Total as $CaCO_3$	mg/L	119
Bicarbonate as HCO_3^-	mg/L	145
Conductivity (25°C)	mS/m	5440
pH (25°C)		7.93
Total dissolved solids (105°C)	mg/L	37618
Chemical Parameters		
Boron as B	µg/L	3370
Bromine as Br^-	µg/L	0.15
Calcium as Ca	mg/L	394
Chloride as Cl^-	mg/L	18325
Fluoride as F^-	mg/L	0.86
Magnesium as Mg	mg/L	1220
Potassium as K	mg/L	581
Sodium as Na	mg/L	11500
Sulphate as SO_4^{3-}	mg/L	2473
Strontium as Sr	µg/L	648

The measured pH was slightly lower than the characteristic pH of 8 that was expected from the literature survey in Section 2.2. Taking into consideration that the seawater was proven to be basic, the main cathodic reaction of HY-80 in seawater would be oxygen evolution rather than hydrogen reduction.

The presence of Magnesium and Calcium in the collected seawater could lead to the formation of a protective scale of calcium carbonate ($CaCo_3$) or magnesium hydroxide ($Mg(OH)_2$) precipitates (Möller, Boshoff and Froneman, 2006). Möller et al. (2006) reported the formation of what was believed to be $Mg(OH)_2$ precipitates on low carbon steel submerged in natural seawater for three days, but XRD could not confirm its presence. Roberge (2008), on the other hand, states that magnesium hydroxide will only precipitate in seawater with a pH of higher than 9.5 and therefore it is assumed to be irrelavent in the current study.

3.2 Mechanical Property Analysis

3.2.1 Tensile Testing

An Instron Electromechanical 5982 series universal testing machine (Figure 24) was used to perform tensile testing on plate type subsize specimens with a gauge length of 25 mm and a cross section of 6x6 mm according to the ASTM E8/M-15a (Standard Test Method for Tension Testing of Metallic Materials, 2015) (Figure 23). A technical drawing can be viewed in Appendix F. The loadframe was fitted with a 100 kN load cell and an extensometer (Instron 2630) for determination of yield strength as required by the ASTM E8/M standard. Bluehill Universal software was used to control the frame and monitor and capture the applicable tensile data. A strain rate of 0.015 mm/mm/min was applied up to an elongation of 5% after which the speed of testing was increased to 0.5 mm/mm/min.

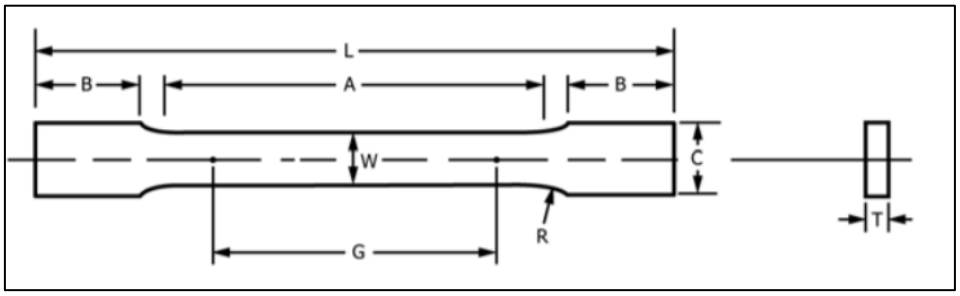

Figure 23: Plate type tensile specimen (ASTM E8/E8M, 2015).

The extensometer was used to capture displacement data up to an extension of 5% of the gauge length, after which the test was paused and the extensometer was removed, and the test was continued by using crosshead displacement. Strain was calculated as:

$$\varepsilon = \frac{\Delta l}{l_{gauge}} \tag{3.2.1}$$

where Δl is displacement and l_{gauge} is the gauge length. Stress was calculated by dividing the captured load data by the original cross-sectional area as measured using a micrometer with a resolution of 0.01 mm.

Figure 24: Instron Electromechanical 5980 universal testing machine.

3.2.2 Hardness Testing

Hardness testing was performed on unetched, polished metallographic samples. A Durascan-10 micro-hardness testing machine with a 1 kgf load was used. Fifteen measurements (three rows of five) were made on each sample surface, with 1 mm distance between measuring points.

3.2.3 Density Measurements

The density of HY-80 was required for corrosion rate calculations in Eq. 2.4.1 and 2.4.9, but no value could be found in literature, it was therefore determined experimentally using the Archimedes principle. Three different samples were used to calculate density ($\rho_{HY\text{-}80}$) as:

$$\rho_{HY-80} = \frac{\rho_w}{1 - \left(\frac{m_w}{m_a}\right)} \tag{3.2.2}$$

where ρ_w is the density of water, m_w is the weight of the sample in water and m_a is the weight of the sample in air. Water temperature at the time of testing was found to be 16°C. The correlating density of the water was taken as 0.9989 g/cm^3 (Çengel and Ghajar, 2015)

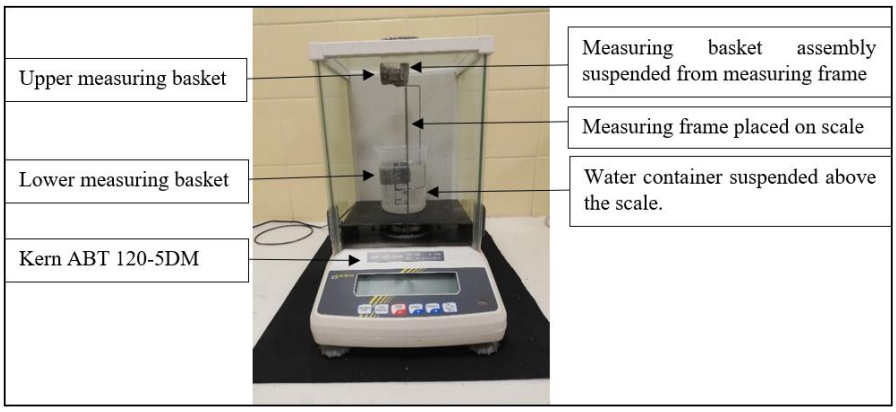

Figure 25: Archimedes density measurement testing set-up.

The test set-up (Figure 25) was placed on a scale after which the scale was zeroed. A sample was then weighed in the upper measuring basket to determine the weight in air. Without disturbing the position of the set-up, the sample was moved to the lower measuring basket to determine the weight in water. Special care was taken to ensure that the sample did not trap any air in the basket or on the sample surface as this will lead to erroneous measurements.

3.3 Microstructural Analysis

3.3.1 Metallographic Sample Preparation

Samples were hot mounted with a Buehler SimpliMet 1000 automatic mounting press at a temperature of 180°C and a pressure of 280 bar in phenolic resin, and then ground in a Buehler Alpha grinding and polishing machine. Samples were rinsed with water between grinding and polishing steps and cleaned with iso-propanol in an ultrasonic cleaner afterwards. Table 9 contains the *AKASEL* duplex steel grinding and polishing procedure (Aka-Brief #7 Stainless and Duplex steels, 2020).

Table 9: Grinding and polishing procedure.

Step	Grinding/Polishing disc	Lubricant	Speed	Force	Time
1	Piatto 220	Water	High	25 N	Until plane
2	Allegran 3	DiaMaxx Poly 6 µm	Low	25 N	5 min
3	Daran	DiaMaxx Poly 3 µm	Low	25 N	4 min
4	Chemal	Fumed Silica 0.2 µm	Low	20 N	2 min

3.3.2 Optical Microscopy

HY-80 has a very fine, homogeneous grain structure that cannot be observed without etching. A 2% Nital solution was used to etch the samples for up to 40

seconds in order to reveal the grain boundaries. An Olympus GX51 microscope fitted with an Olympus SC30 CMOS colour camera was used to study the microstructure of the steel and Stream Essensials 1.9.4 software was used to capture the images.

3.3.3 Scanning Electron Microscopy

Scanning electron microscopy (SEM) and energy dispersive spectroscopy (EDS) was performed at the Central Analytical Facilities of Stellenbosch University. A Zeiss EVO MA15VP fitted with an EDS detector was used to determine the composition of the acquired steel. Oxford Instruments' Aztec software was used to analyse the EDS data.

3.4 Corrosion Analysis

3.4.1 Electrochemical Corrosion Instrumentation

A Reference Gamry 600 Potentiostat/Galvanostat (Figure 26) with a maximum current range of ± 600 mA and a potential range of ±11 V was used for all electrochemical testing along with Gamry Framework V7.07 software for monitoring and control of the potentiostat. The software has built-in programming for many different accelerated corrosion tests such as linear polarization and dynamic polarization.

A Gamry Multiport corrosion cell with a maximum working volume of 1200 mL was used to hold the working electrode, carbon counter electrode and a saturated calomel (SCE) reference electrode. The cell was fitted with a Gamry Reference bridge tube, which is a Luggin-Haber capillary with a CoralPor™ porous glass frit. The diameter of the frit is 2.8 mm. The bridge tube allows for measurement close to the sample surface without contamination of the reference electrode or the working fluid.

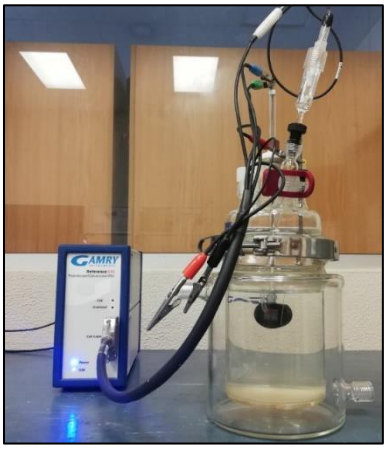

Figure 26: Gamry Multiport electrochemical cell.

3.4.2 Potentiostat Calibration

Potentiostat calibration was performed according to the Gamry Reference 600 user manual before testing. A dummy corrosion cell was connected to the potentiostat and placed in a faraday cage to prevent electrical interference. Calibration was software controlled.

3.4.3 Corrosion Specimen Preparation

Electrochemical samples were mounted in resin to ensure that only one surface is exposed to the electrolyte. The resin was ground flat at one side to allow for drilling and tapping to accommodate the 3 mm sample holder rod. Samples were polished with 200, 400 and 600 grit SiC to provide a sample surface with no large defects that could lead to crevice corrosion at the sample-resin interface. Each sample was polished with an 800-grit disk for a minute, rinsed with distilled water and dried with ethanol five minutes before immersion in the testing solution; this ensured that the sample-solution interfaces were clean and consistent between tests.

Immersion corrosion test samples were ground and cleaned in the same manner as the potentiodynamic samples. All of the samples were measured with an electric vernier with a resolution of 0.01 mm. A 4.5 mm hole was drilled to suspend samples in the testing tank with plastic hooks. Each sample was weighed with a Kern ABT 120-5DM analytical balance scale to a resolution of 0.1 mg before immersion.

3.4.4 Polarization Measurement

Before polarization of the corrosion cell, the sample was allowed to stabilise in the testing fluid at room temperature (25 ± 2°C). To determine if a stable potential was reached, the open circuit potential, E_{OCP} between the reference electrode and the working electrode, was monitored. Figure 27 shows a typical open circuit potential curve, it can be seen that a relatively stable potential (less than ± 5 mV/min fluctuation) could be reached within 1 hour. Samples were left to stabilise for 1.5 hours before initiation of the polarisation tests.

The linear polarization method was performed first, as this test is non-destructive. Samples were polarized to -20 mV below the E_{OCP} to 20 mV at a relatively slow rate of 0.6 V/h to avoid charging effects on the sample surface (Fischer *et al.*, 2019). The sampling frequency was set to 1 s. Data was plotted in real time as polarization against measured total current. Once the linear polarization test was completed, the sample was left unpolarized to assess the stability of the sample. Owing to the fact that linear polarization is considered non-destructive, it is expected that the corrosion potential is mostly unchanged.

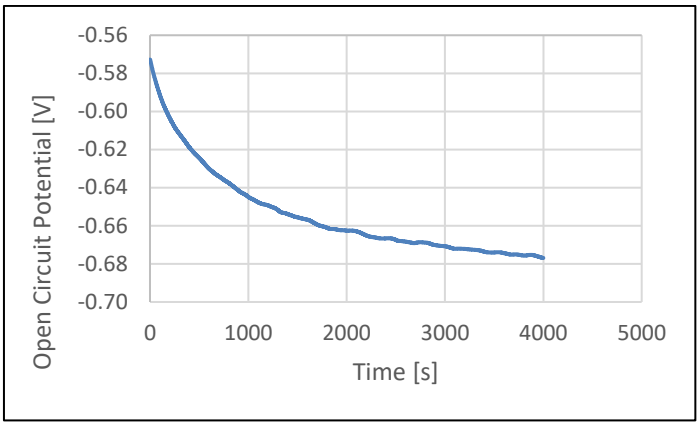

Figure 27: Open circuit potential of an HY-80 sample in seawater.

Potentiodynamic scans were initiated after polarization resistance data was captured. An initial delay of 1 minute was set before polarization. The delay serves as a means to capture the E_{OCP} which was later compared to the original open circuit potential to ensure that the system was still stable. Some drift in the E_{OCP} was expected seeing that the sample potential could still be changing naturally. The sample was polarized from -0.3 V more negative than the E_{OCP} to 0.3 V positive of the E_{OCP}. Wider ranges of potentiodynamic scans were not needed as localised corrosion mechanisms such as pitting, crevice corrosion and stress corrosion cracking were not investigated.

3.4.5 Immersion Testing

Immersion corrosion tests were performed using a temperature-controlled water tank with a volume of 10 L. A 12 V temperature control module was used to regulate the temperature of the water. A relay was used to switch a 50 W 220 V heating element – a schematic is shown in Figure 28. The accuracy of the temperature controller was verified weekly with a HUATO S220-T8 datalogger and a K-type thermocouple.

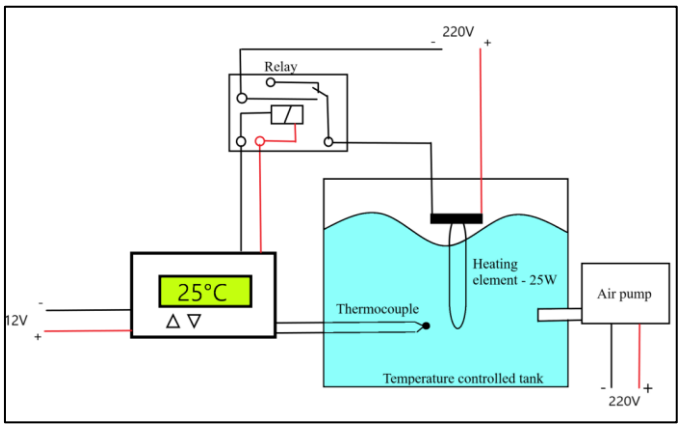

Figure 28: Schematic diagram of immersion testing set-up

3.4.5.1 Testing Procedure

Samples were immersed in seawater for 14 and 30 days at a temperature of 25 ± 1°C. Water in the tank was changed weekly to ensure that the corrosion product did not affect corrosion behaviour and that the reactive components in the water such as salts were not depleted or concentrated as a result of evaporation. A small air pump was used as agitation in the water to minimise temperature gradients as required by ASTM G31-12a (Standard Guide for Laboratory Immersion Corrosion Testing of Metals, 2012), and samples were reordered daily as an additional measure to mitigate any temperature gradient effects.

Table 10: Electrolytic procedure for removal of corrosion product (ASTM G31, 2012).

Material	Solution	Time	Temperature	Treatment
Iron, Cast Iron or Steel	75 g NaOH 25 g Na_2SO_4 75 g Na_2CO_3 Reagent water to make 1 L	20-40 min	20 to 25°C	Cathodic treatment with 100-200 A/m^2 with a stainless steel anode

3.4.5.2 Post-Immersion Cleaning

Loose corrosion product was removed by scrubbing with a non-metallic brush after which the electrolytic cleaning procedure, E.1.1 (Table 10), as designated in ASTM G1-03 (Standard Practice for Preparing, Cleaning, and Evaluating Corrosion test Specimens, 2003), was performed. A reference sample with no corrosion was also weighed and cleaned in the same manner to determine the material lost as a result of the cleaning procedure.

3.4.5.3 Immersion Corrosion Rate Determination

Samples were weighed after cleaning and a mass loss was determined. This value was corrected by taking into account the mass lost as a result of the cleaning procedure. A corrosion rate was determined according to:

$$CR = \frac{KW}{ATρ} \tag{3.4.1}$$

where K is a constant that converts the corrosion rate to the required units, in this case, in millimetres per year (mm/y), $K = 8.76 \times 10^4$; W is the mass loss in grams; A is area in cm^2; T is the exposure time in hours and ρ is the density in g/cm^3.

4 Simulation Methodology

4.1 Preliminary Snalysis Using SDF

A preliminary analysis was performed using the submarine design formulas discussed in Section 2.8.2. The purpose of the analysis was to identify the most critical out-of-circularity modes for incorporation in the finite element analysis. The calculated critical pressures are shown in Table 11. A sample calculation can be viewed in Appendix D. All measurements were determined using sketches in the public domain (Appendix G) and site visits at the Simon's Town Naval base.

The interframe out of circularity number and its associated pressures are a function of the stiffener parameters, shown in Figure 29 and is therefore the same for all the submarine sections. Figure 29 is similar to Figure 17, but instead of domed ends, a section between deep frame stiffeners is analysed. Different values of out of circularity mode numbers, *n*, were tested using the Von Mises buckling equation (Eq. 2.8.10) to identify the most interframe mode (Figure 30) that would yield the lowest critical pressure. A similar procedure was followed to identify the overall elastic collapse pressure for each submarine section according to Eq. 2.8.12. Figure 31 shows the minimisation of the critical submarine section with a length of 15.05 m. The other submarine compartments were also tested as each section would have different collapse pressures. As expected, the longest section (15.05 m) had the lowest overall elastic buckling pressure.

The most critical mode numbers were found to be 16 for the interframe imperfections, n_i, and 2 for overall imperfections. The overall mode number (n_o) is interesting in the sense that this would be the same critical mode for an unstiffened cylinder, indicating that the cylinder length is excessively long. Bulkheads or deep frame stiffeners are typically placed two cylinder diameters apart (Burcher and Rydill, 1995), which is not the case for the investigated submarine.

Table 11: Preliminary results based on approximate empirical hull design formulas.

Compartment independent pressures	Reference	Pressure (MPa)
P_y	Eq. 2.8.4	6.07
P_m (n_i=16)	Eq. 2.8.10	12.85
Pc (Mean)	From Figure 18	5.34
Overall elastic buckling pressure according to compartment length		
15.050 m (n_o=2)		12.02
6.880 m (n_o=3)		25.71
5.590 m (n_o=3)		30.70
3.890 m (n_o=4)		43.82

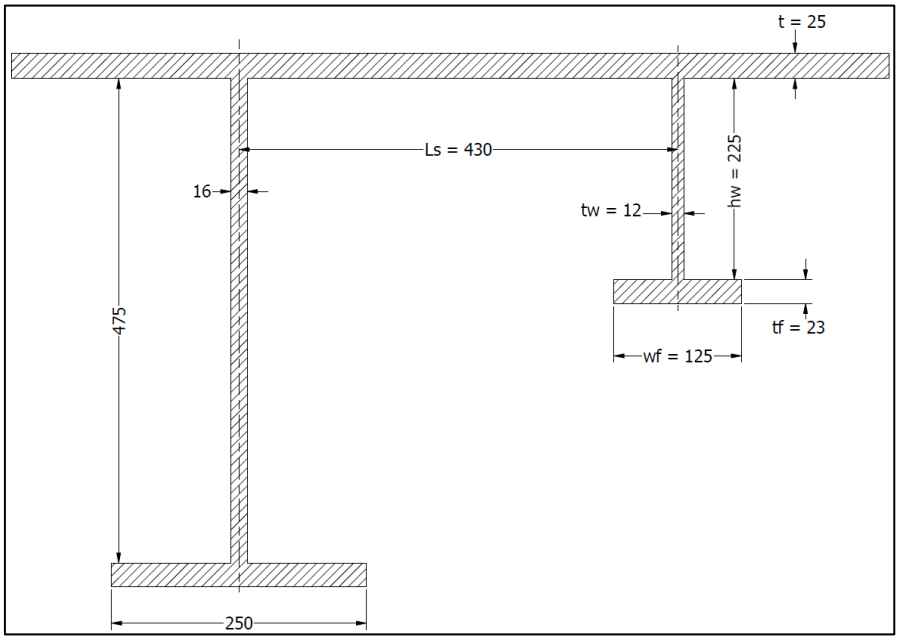

Figure 29: Geometric parameters of hull stiffeners.

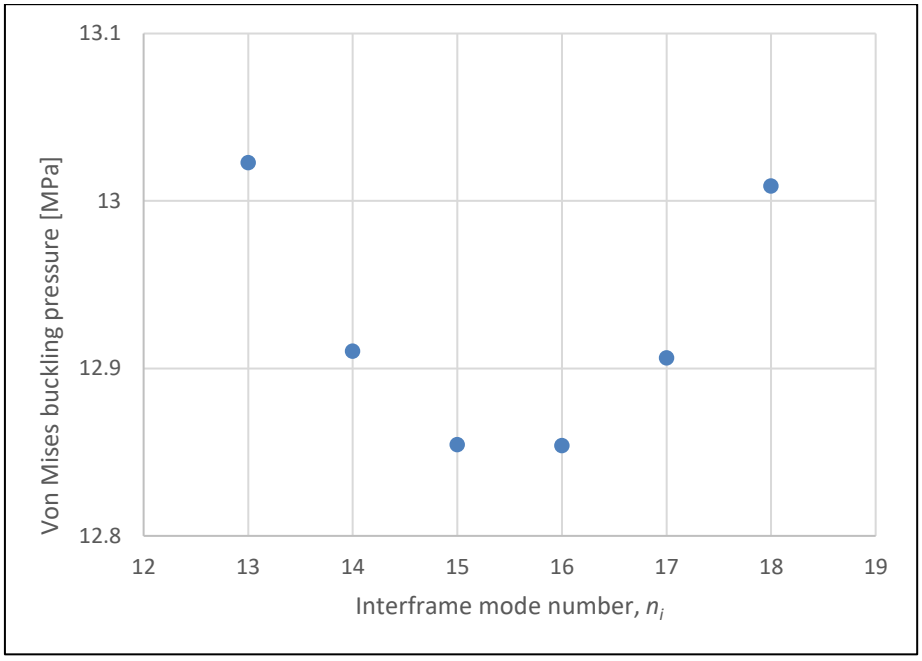

Figure 30: Minimisation of interframe buckling pressure.

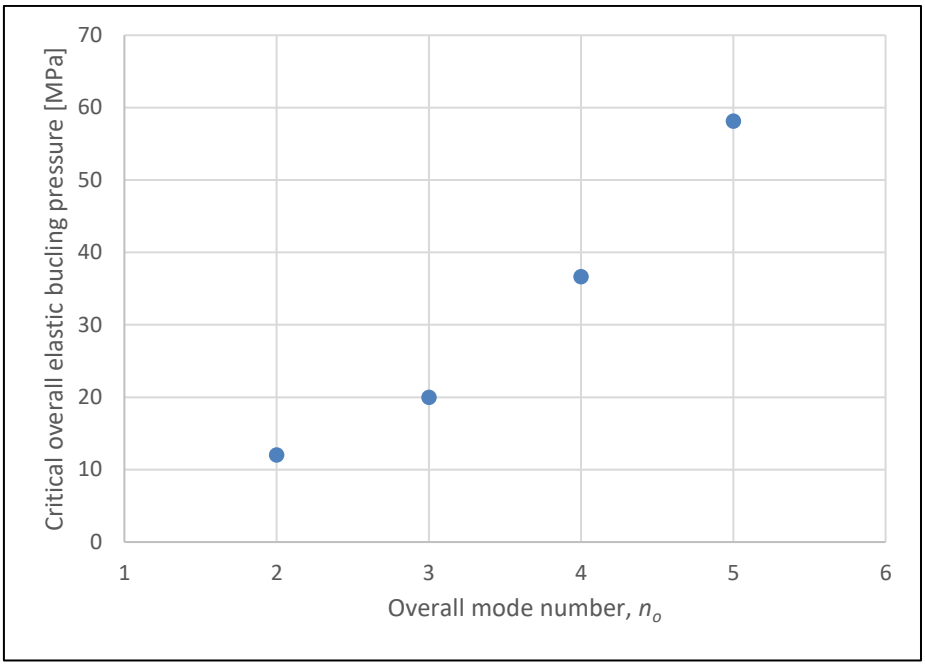

Figure 31: Minimization of overall elastic buckling pressure

4.2 Finite Element Analysis

4.2.1 Model Geometry

A finite element analysis was performed on the most critical submarine section identified in the preliminary analysis. Penetrations and residual stresses induced by the manufacturing procedures were not incorporated in the model as there was insufficient information made available about these parameters.

The analysed section comprised 34 light tee stiffeners, with dimensions shown in Figure 29, between two large deep frame stiffeners. The stiffeners were spaced 430 mm apart so that the total length of the section is 15.05 m. The section had a nominal diameter of 6.2 m. Burcher (1995) stated that bulkheads are typically placed two diameters apart to prevent overall collapse, and seeing that a deep frame stiffener is not as rigid as a watertight bulkhead, it is expected that overall collapse might occur before inter stiffener collapse. Shell theory was utilised for the whole model. The section was meshed using 4 noded quadrilateral shell elements. Corrosion thinning was introduced as uniform one-sided reduction of the whole shell plating thickness. This was achieved by specifying a *shell offset ratio* in Abaqus so that the reference surface, where nodes are defined, is offset from the mid-surface of the original shell (Figure 32). Symmetry in the longitudinal and circumferential directions was utilised so that only one eighth or one quarter of the bay had to be analysed, depending on the applied imperfections. This minimised computational time and simplified boundary conditions.

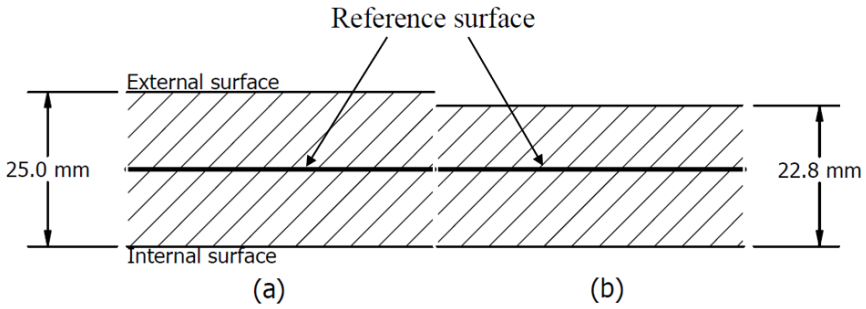

Figure 32: The rendered thickness of shell plating where (a) is intact and (b) is thinned

4.2.2 Incorporation of Out of Circularity Modes

In the absence of actual out of circularity measurements of the submarine hull, an idealised imperfection set was applied to the mesh in order to initiate non-linear buckling. A maximum amplitude of just more than 0.5% of the mean cylinder radius was applied so that the mesh was perturbed up to 15.75 mm. This corresponds to the maximum out-of-circularity imperfections covered in the submarine design formulas discussed in Section 2.8.2.

A Matlab script, given in Appendix E, was written to apply the out-of-circularity errors. The script imports nodal position data from an Abaqus input file. The nodal positions are then edited using mathematical expressions (Eq. 4.2.1 and 4.2.2) of the mode shapes as shown by Gannon (2010). An overall out-of-circularity with mode number of $n_o = 2$ (Figure 33) and an amplitude of 15.5 mm was applied to the whole structure, including the stiffeners:

$$dR_o = A_o \sin(\varphi + n_o\pi) \sin\left(\frac{\pi}{2} + \frac{x\pi}{L_c}\right) \qquad (4.2.1)$$

where dR_o is the change in radial position of a node, A_o is the amplitude of the applied imperfection, φ is used to control the phase angle, x is the distance of a node from the central point in the submarine section in the X-direction and L_c is the compartment length.

Interframe out of circularity with a mode number of $n_i = 16$ (Figure 34) and an amplitude of 0.25 mm, was applied to the shell plating:

$$dR_i = A_i \sin(\varphi + n_i\pi) \sin\left(\frac{\pi}{2} + L_r\pi\right) \qquad (4.2.2)$$

where A_i is the amplitude of the interframe out of circularity mode, and L_r is the position of a node relative to the two adjacent stiffeners.

The of the out-of-circularity modes were aligned so that symmetry in the XZ and YZ planes was ensured. Two phase alignments were investigated so that the minimum collapse pressure could be determined.

The out of circularity modes could also be produced by performing a linear buckling analysis to identify the first overall and interframe buckling modes. These mode shapes can then be superimposed and applied to a model using the *IMPERFECTION* keyword to import the node displacements. This procedure was not applied because the phase angle of the mode shapes could not be easily controlled.

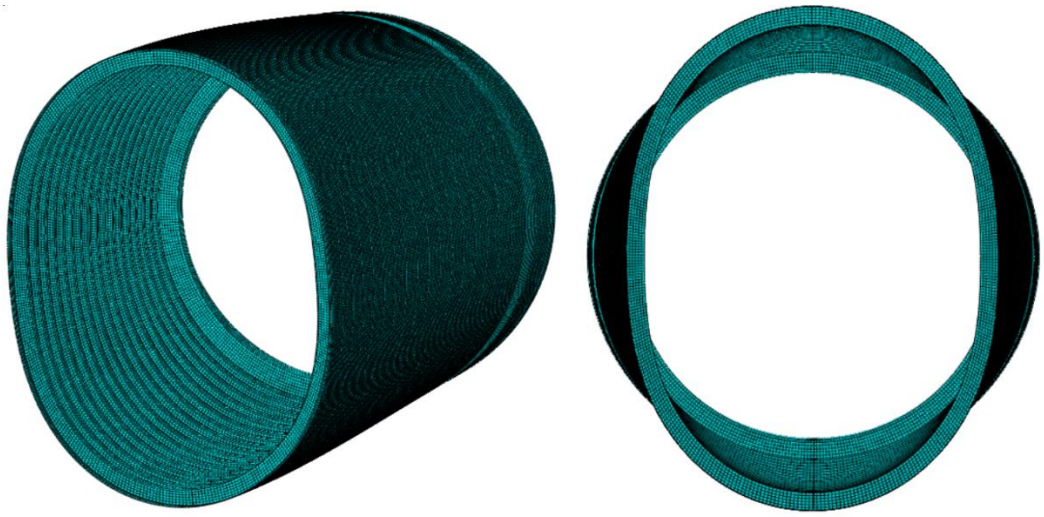

Figure 33: Overall out-of-circularity (n_o=2) with an exaggerated amplitude that will allow overall buckling of the hull.

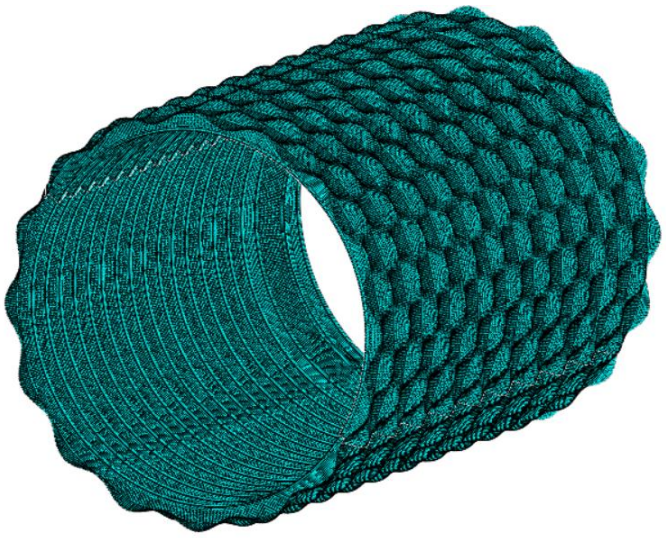

Figure 34: Interframe out-of-circularity (n_i=16) with an exaggerated amplitude that will allow interframe buckling of the hull plating.

4.2.3 Boundary Conditions and Loading

A mid-bay symmetry condition was applied in the X-direction as all imperfection modes are symmetric in the longitudinal direction. Two extra ring stiffeners and hull plate sections were modelled to simulate the effect of an adjacent submarine section on the analysed frame as performed by Smith (2015). Only rotational constraints were applied to the additional section to allow displacement in the X-direction.

Initial calculations showed that the imperfection modes, especially the interframe modes, would yield similar critical buckling loads. It is therefore important to test multiple imperfections to ensure that the most critical modes are accounted for. Depending on the imperfection modes utilised in the model, single or dual planes of symmetry were available. For even mode numbers, two cross-sectional planes of symmetry were employed to minimize the model size and for application of boundary conditions in the Z-X and Y-X planes (Figure 35). Only one cross sectional plane of symmetry (Y-X plane) was utilised for models with uneven mode numbers (Figure 36).

To prevent rigid body motion in the quarter model (Fig 36), a boundary condition was needed in the Z-direction. One solution is to constrain the deep frame stiffener nodes in the radial direction (Y=Z=0) as performed in some research (Gannon, 2010). This does, however, imply that the deep frame stiffener is perfectly rigid, which will artificially stiffen the structure considerably. A second solution was to make use of a “weak spring” boundary condition in which a spring bank connected to ground is modelled. It was anticipated that the loading condition was mostly symmetrical even after applying imperfections in the hull plating, and therefore the spring stiffness required to prevent rigid body motion in the Y-direction was assumed to be very small. This condition could also cause artificial stiffening of the structure, it was therefore important to minimise the spring stiffness to the lowest value that allows convergence of a solution. Both boundary conditions were tested and compared to a quarter cross sectional model to assess their accuracy and validity.

A uniform external pressure load was applied to the hull plating to represent static external diving pressure. Axial loading as a result of end pressures on the submarine was accounted for by applying an equivalent shell edge load in Abaqus. The loading was equal to:

$$F_a = \frac{Pr}{2} \tag{4.2.3}$$

with units of N/mm. This load is equivalent to the axial pressure imparted on the circular cross section of the submarine hull.

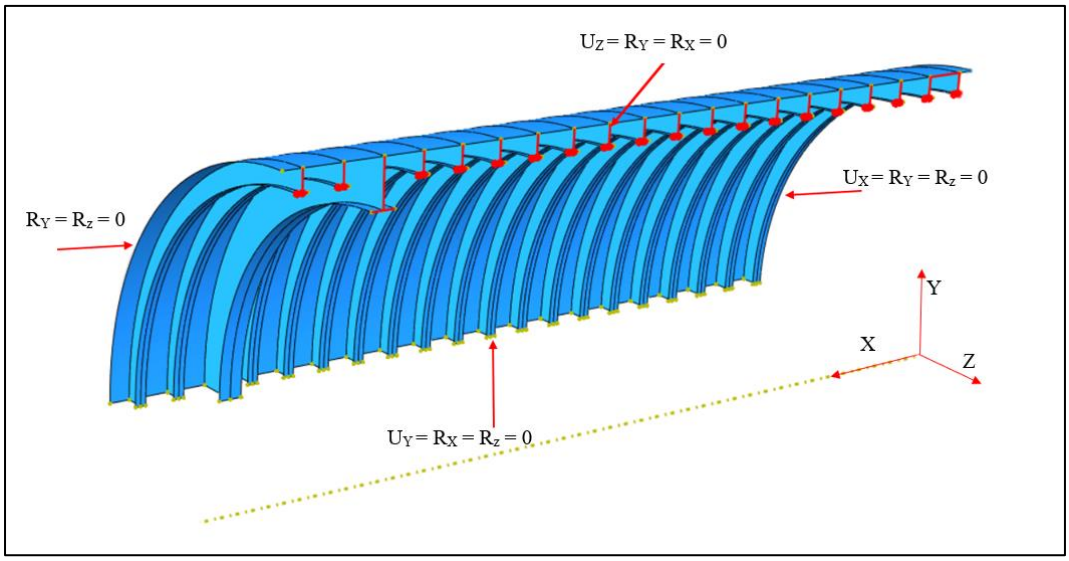

Figure 35: Boundary conditions applied to an eighth model.

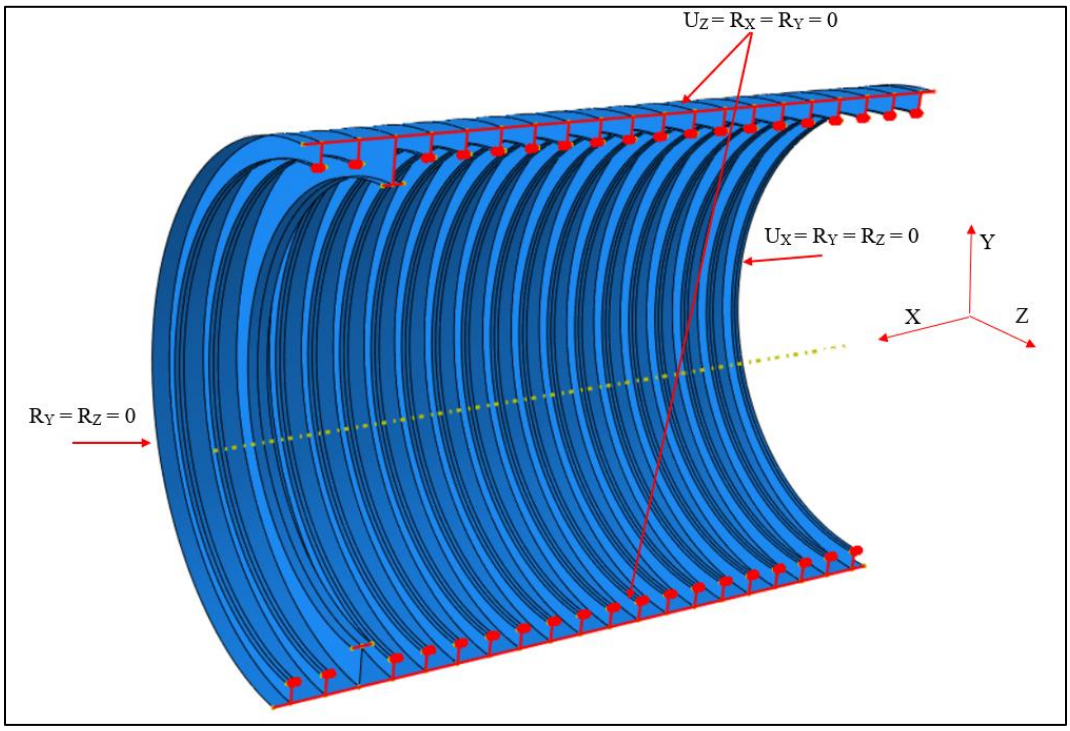

Figure 36 : Boundary conditions applied to a quarter model.

4.2.4 Simulation Environment

The complex nature of the non-linearities associated with submarine collapse necessitates a more complex analysis than elastic buckling. Therefore, a load-deflection analysis, known as the Riks method, was performed. The main

advantage of using the Riks method instead of normal non-linear static analysis is that non-linear buckling and post buckling behaviour can be observed. Abaqus uses Newton's method for solving the equilibrium equations. Simulations were terminated when the load-displacement curve reached a maximum value, indicating the onset of buckling. Loads at yielding were investigated using a nonlinear general static analysis.

Material non-linearity was incorporated by defining a true stress– plastic strain material model in Abaqus. The shape of the plastic region in the stress strain curve was corrected so that the minimum yielding stress was 550 MPa which relates to the minimum yield stress that the material would experience. All the components including the hull plating and stiffeners were defined as HY-80. The large-displacement formulation was activated, by selecting the *Nlgeom* option, to account for geometric non-linearities.

5 Experimental Results and Discussion

5.1 Mechanical Property Analysis

5.1.1 Tensile Properties

Ten tensile specimens were manufactured and tested according to the specifications listed in Section 3.2.1. The stress-strain curves of the original steel as well as the heat-treated samples are shown in Figures 37 and 38. The heat-treated steel only showed a reduction in ultimate tensile strength but no evident decrease of yield strength or increase in elongation was observed as expected from tempering the steel at 590°C. It is interesting to note that both sets of samples exceeded the minimum required properties according to the MIL-16216K (Military Specification for HY-80 and HY-100 steel standard. Similar yield and tensile strengths for as-received steel was quoted by Deb and Challenger (1984) as shown in Table 12.

One specimen, Sample 5, was manufactured incorrectly with a width of only 5.9 mm. This was the only specimen that exhibited an elongation at fracture below 20 % and was therefore excluded from calculation of average stress values.

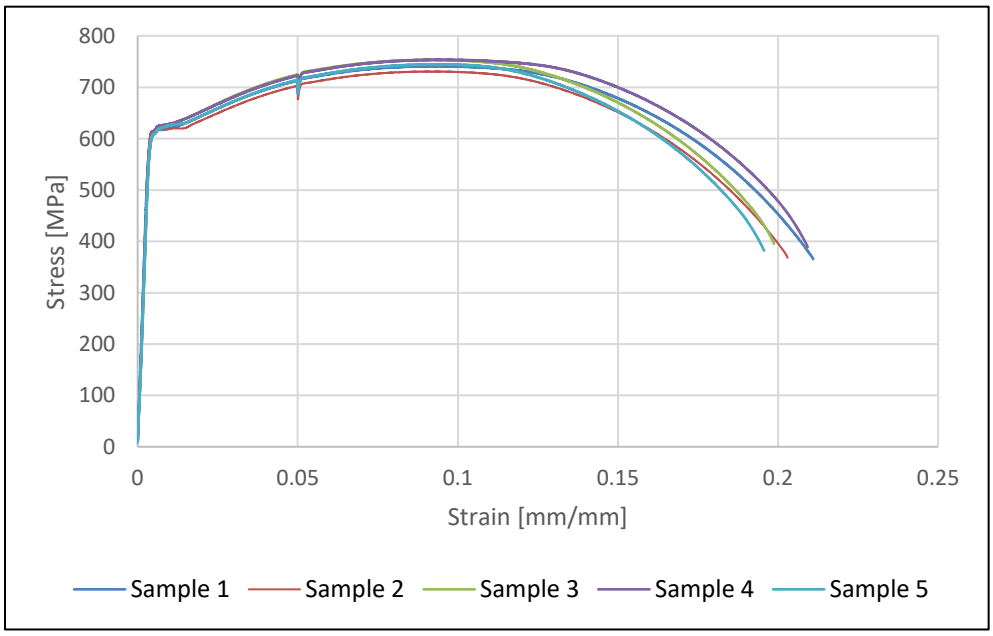

Figure 37: As-received HY-80 stress-strain curves.

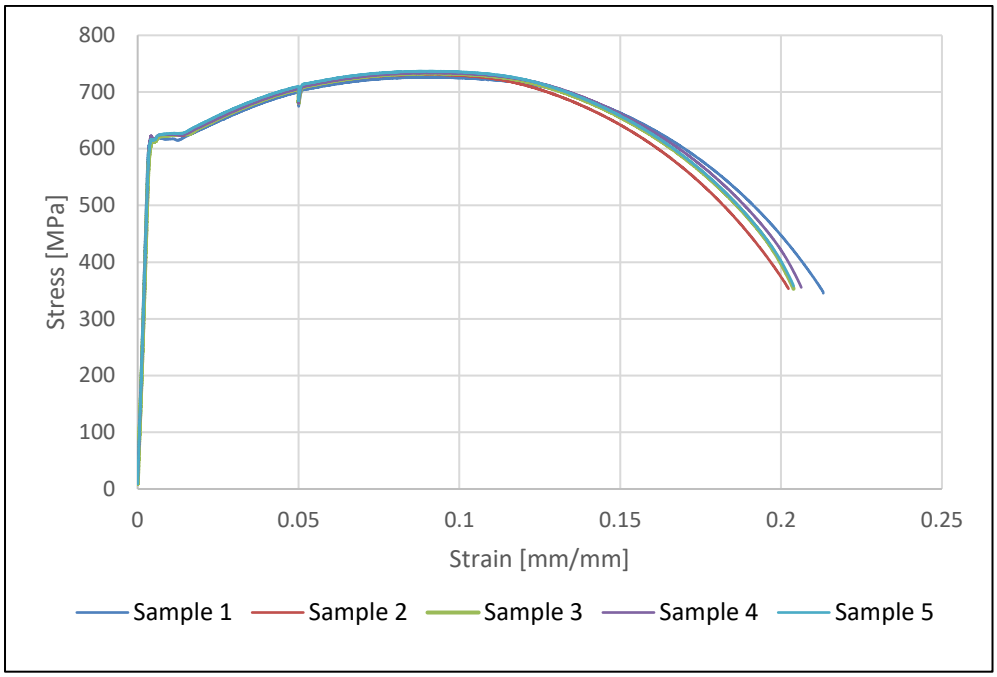

Figure 38: Heat treated HY-80 stress-strain curves.

Table 12: Tensile properties of HY-80 steel.

Tensile Property	Measured as received	Measured heat treated	Deb and Challenger	MIL-S-16216K
Yield strength	615 ± 4 Mpa	612 ± 2 MPa	605 MPa	552 MPa
Ultimate tensile strength	744 ± 11 Mpa	731 ± 5 MPa	700 MPa	-
Elongation at fracture	20.6 ± 0.5 %	20.6 ± 0.4 %	21 %	20 %

5.1.2 Vickers Hardness

Vickers hardness tests were performed on heat treated and as received samples as described in Section 3.2.2. The hardness tests confirmed the strain relief heat-treatment did not have a significant effect on the mechanical properties of HY-80. The average Vickers hardness was found to be 234 for as-received steel and 228 for the heat-treated steel.

Table 13: Vickers hardness measurements for HY-80 Steel

Condition	Position	Vickers hardness [HV1]	Average
As received	Top	234	234 ± 3
		234	
		234	
		235	
		230	
	Middle	229	
		237	
		235	
		231	
		236	
	Bottom	229	
		231	
		238	
		236	
		238	
Heat treated	Top	225	228 ± 2
		228	
		225	
		224	
		228	
	Middle	228	
		230	
		226	
		227	
		227	
	Bottom	230	
		229	
		228	
		229	
		229	

5.1.3 Archimedes Density

. The sample weights and resulting densities according to Eq. 3.2.2 is given in Table 14. The calculated density was slightly lower than the general density of 7.85 g/cm^3 given for low alloy steel in the ASTM G102 standard.

Table 14: Archimedes density of HY-80 steel.

Sample	Weight in air [g]	Weight in water [g]	Density [g/cm^2]
1	11.2177	9.7808	7.798
2	11.2163	9.7781	7.790
3	11.2214	9.7818	7.786
		Average:	7.792
		Standard deviation:	0.005

5.1.4 Measurement of Actual Hull Thinning

Actual hull thinning was measured using an ultrasonic thickness gauge with an accuracy of 0.01 mm. Measurements were made in January 2020 at the Naval base in Simon's Town. The investigated submarine was being refurbished in dry-dock, and it was therefore possible to take measurements from the outside of the hull.

Twenty-three measurements were taken along the length of the hull at thirteen cleaned locations with approximate positions shown in Figure 39. The measured values are shown in Table 15. Double measurements were not possible at three of the thirteen locations where access was restricted or internal welded structured made hull thickness measurement impossible. Maximum and minimum thicknesses of 24.81 mm and 22.99 mm respectively were measured at opposite ends of the submarine hull. The average thickness was found to be 23.85 mm with a standard deviation of 0.41 mm.

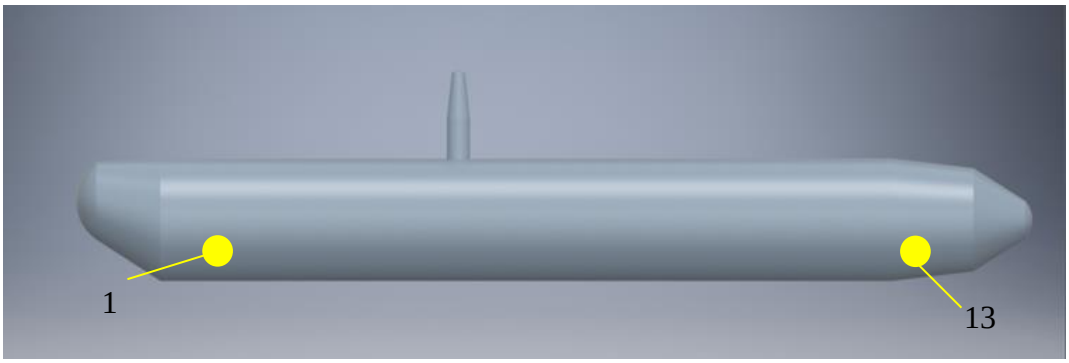

Figure 39: Thickness measurement range on the submarine pressure hull.

Assuming an original hull thickness of 25 mm, in-service thinning of the hull varied from as low as 0.2 mm up to 2.0 mm over the 10-year service life of the submarine. The maximum corrosion rate can be determined by dividing the maximum loss of material by the amount of service years:

$$Maximum\ penetration = 25\ mm - 22.99\ mm = 2.01\ mm$$

And therefore, the maximum in-service corrosion rate:

$$Penetration\ rate = \frac{Loss\ of\ material}{Service\ time} = \frac{2.01}{10} = \frac{0.201\ mm}{year}$$

The average rate is estimated in the same manner as 0.15 mm/year. For the purposes of this study it is assumed that most of the material lost is due to corrosion, but other forms of damage such as removal of organic material such as barnacles and seagrass by manual scraping or scrubbing could also have contributed to material loss. Dry dock cleaning could also include high-pressure abrasive spraying. This technique is listed in literature (Song and Cui, 2020).

Variations in hull thickness as a result of manufacturing techniques might also be present, but without beginning of life data on hull thickness, it is not considered in this analysis.

Table 15: Hull thickness measurements taken along the length of the submarine pressure hull

Hull thickness measurements		Hull thickness measurements	
Position	Measurement [mm]	Position	Measurement [mm]
1	24.81	8	23.82
	24.72		-
2	23.76	9	23.79
	23.62		24.00
3	23.67	10	23.41
	23.68		23.38
4	24.34	11	24.05
	24.32		-
5	23.43	12	23.92
	23.40		23.94
6	24.02	13	22.99
	23.82		-
7	23.69		
	23.94		

5.2 Microstructural Characterisation

5.2.1 Optical Microscopy

Optical micrographs were taken to identify any changes in microstructure as a result of heat treatment. This was aimed at explaining any changes in mechanical properties (if any), as well as any difference in corrosion resistance between the two sets of samples (pre-heat-treated and post-heat-treated).

Figure 40 shows as received and heat-treated HY-80 under optical microscopy. Micro-porosity, which can serve as pitting initiation sites, is observed in both samples.

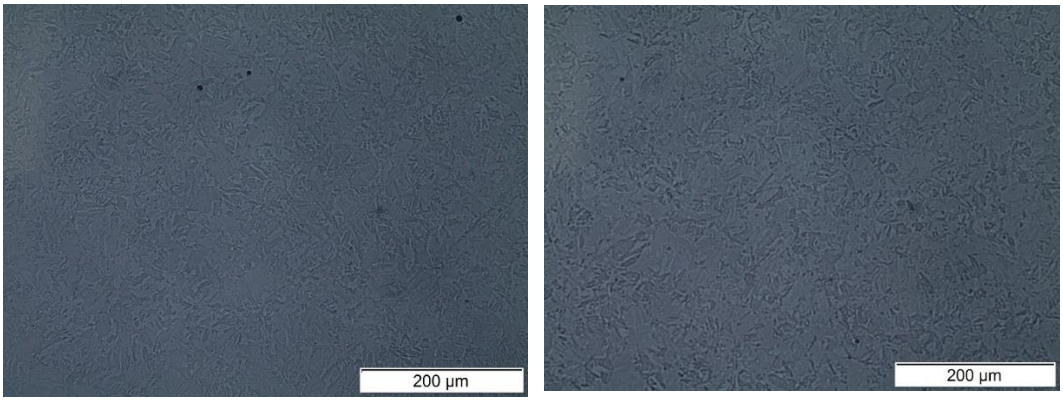

Figure 40: Optical micrographs of as received HY-80 (a) and heat treated HY-80 (b)

Etching the samples with a 2% Nital solution revealed more of the microstructure (Figure 41 & 42). The images show an extremely fine microstructure that is difficult to identify. According to Deb and Challenger (1984), the microstructure of HY-80 consists of a bainitic martensitic duplex structure with prior austinite grain boundaries. Bainite forms as extremely fine needles or plates consisting of cementite (Fe_3C) and ferrite phases that can only be observed using electron microscopy (Callister and Rethwisch, 2015). Similarly, the tempered martensite covering most of the sample surface consists of Fe_3C particles in a α-Ferrite matrix. No clear difference is observed between the heat treated and as received steel microstructure. The similarities in microstructure is in agreement with the findings of the mechanical properties of the steel.

An attempt was made to identify some microstructural characteristics as performed by Oktadinata (2019). Most of the microstructure is a Martensitic-Bainitic duplex structure.

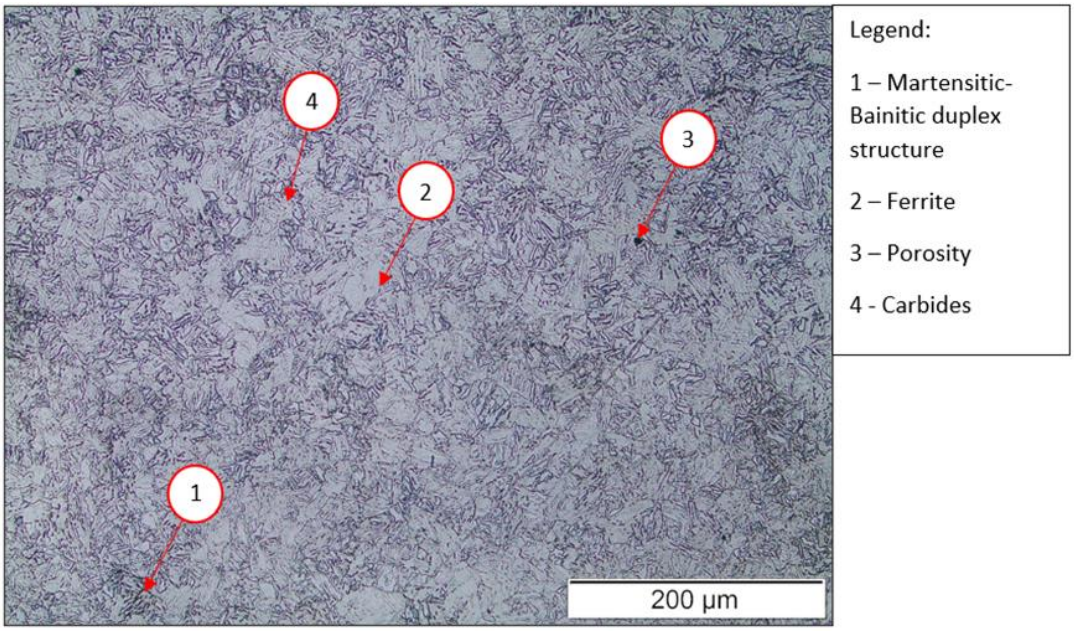

Figure 41: Optical micrograph of etched HY-80 steel.

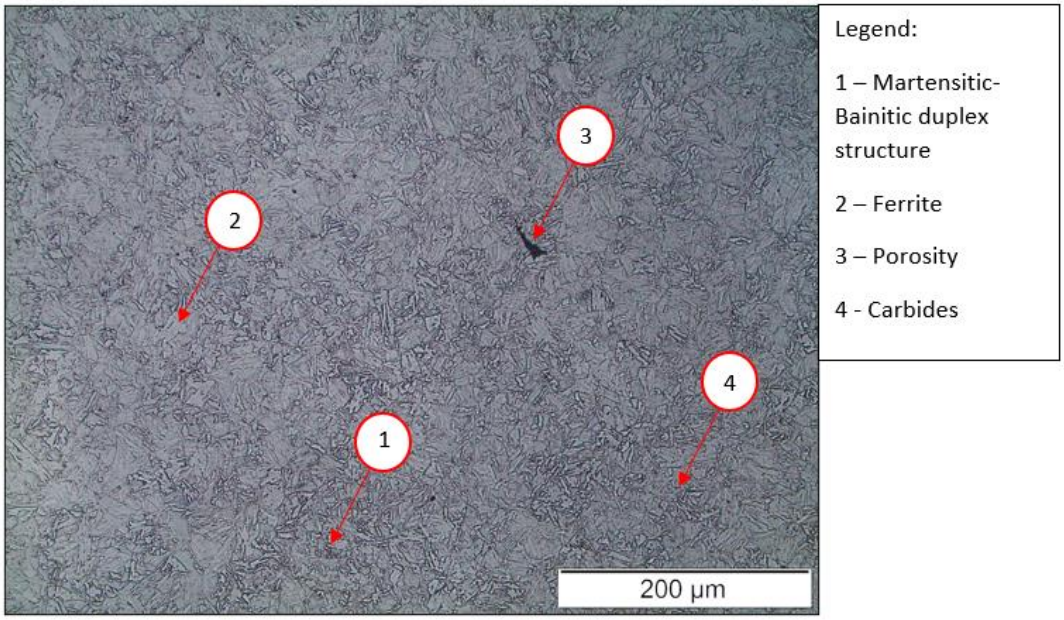

Figure 42: Optical micrograph of heat treated HY-80 steel.

5.2.2 SEM and EDS

SEM/EDS analysis on the HY80 material samples was undertaken with the aim of further investigation of the material's microstructure, as well as to determine the composition of the material as required for the corrosion analysis. Homogeneity was also investigated, even though micro-hardness and optical microscopy already indicated a homogeneous martensitic microstructure. Figure 43 shows that the material is very homogeneous. Some porosity is observed on the sample surfaces.

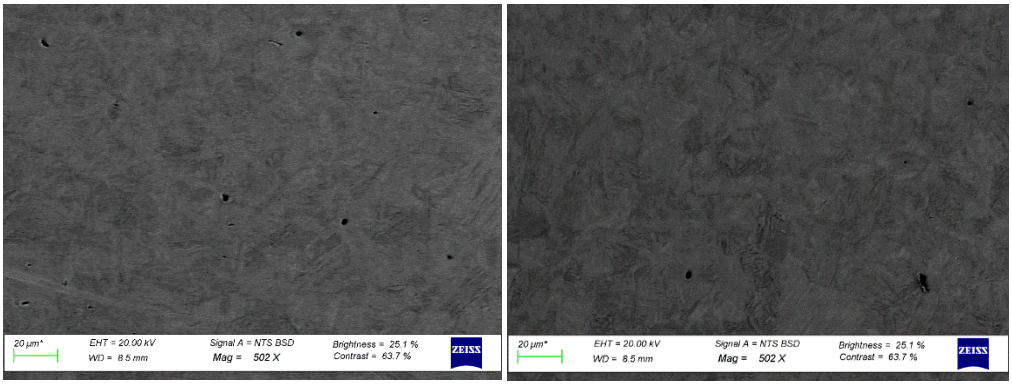

Figure 43: Electron Micrographs of (a) as received and (b) heat-treated HY-80 steel.

Figure 44 shows an example of a line scan conducted on an HY-80 sample with its overall composition shown in Table 16. There was no notable change in distribution of elements. The EDS spot resolution was not high enough to analyse the specific phases present in the fine microstructure. Another limitation with the instrumentation is that elements with mass percentages lower than about 0.2% could not be identified. The composition of the microstructure is as expected, with all of the elements falling in the range specified in Table 4.

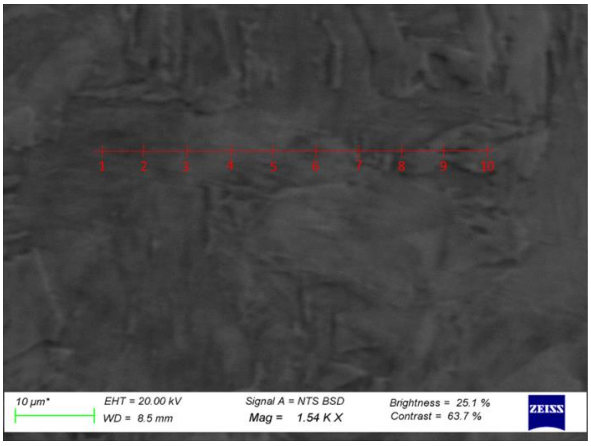

Figure 44: SEM image showing the positions of an EDS line scan on HY-80 steel.

Table 16: Chemical composition of HY-80 steel obtained from an EDS analysis.

Spot	Composition (%)					
	Si	Cr	Mn	Fe	Ni	Mo
1	0.280	1.678	0.268	93.355	2.793	0.557
2	0.304	1.631	0.347	92.946	2.977	0.545
3	0.320	1.697	0.352	93.103	2.840	0.695
4	0.281	1.711	0.365	92.768	3.139	0.659
5	0.294	1.752	0.276	93.156	2.889	0.507
6	0.276	1.746	0.261	93.318	2.830	0.721
7	0.312	1.782	0.290	93.190	2.704	0.639
8	0.302	1.760	0.248	93.055	2.879	0.688
9	0.304	1.761	0.279	93.079	2.717	0.849
10	0.303	1.793	0.228	92.893	2.976	0.695
Ave	0.298	1.731	0.291	93.086	2.874	0.656
Standard deviation	0.0145	0.051	0.047	0.183	0.131	0.100

Table 17: Chemical composition of HY-80 steel in a heat-treated condition obtained from an EDS analysis.

Spot	Composition (%)					
	Si	**Cr**	**Mn**	**Fe**	**Ni**	**Mo**
1	0.308	1.575	0.326	93.467	3.068	0.642
2	0.303	1.600	0.228	93.574	3.103	0.652
3	0.321	1.720	0.305	93.040	3.087	0.756
4	0.359	1.739	0.291	92.628	3.086	0.529
5	0.376	1.601	0.350	92.800	3.198	0.768
6	0.319	1.694	0.322	92.976	3.061	0.623
7	0.324	1.576	0.227	92.625	2.934	0.723
8	0.295	1.460	0.208	92.904	2.646	0.784
9	0.294	1.505	0.255	93.686	2.817	0.523
10	0.316	1.561	0.271	93.665	2.924	0.755
Ave	0.322	1.603	0.278	93.137	2.992	0.676
Standard deviation	0.0266	0.091	0.048	0.422	0.164	0.097

5.3 Corrosion analysis

The corrosion rate of HY-80 steel in natural seawater was investigated using three methods, namely potentiodynamic polarization, the polarization resistance technique and immersion corrosion tests.

5.3.1 Potentiodynamic Polarization

Full potentiodynamic scans were conducted on as-received and heat treated steel at room temperature between a range of -0.3 V and +0.3 V. Two typical potentiodynamic scans can be viewed in (Figure 45).

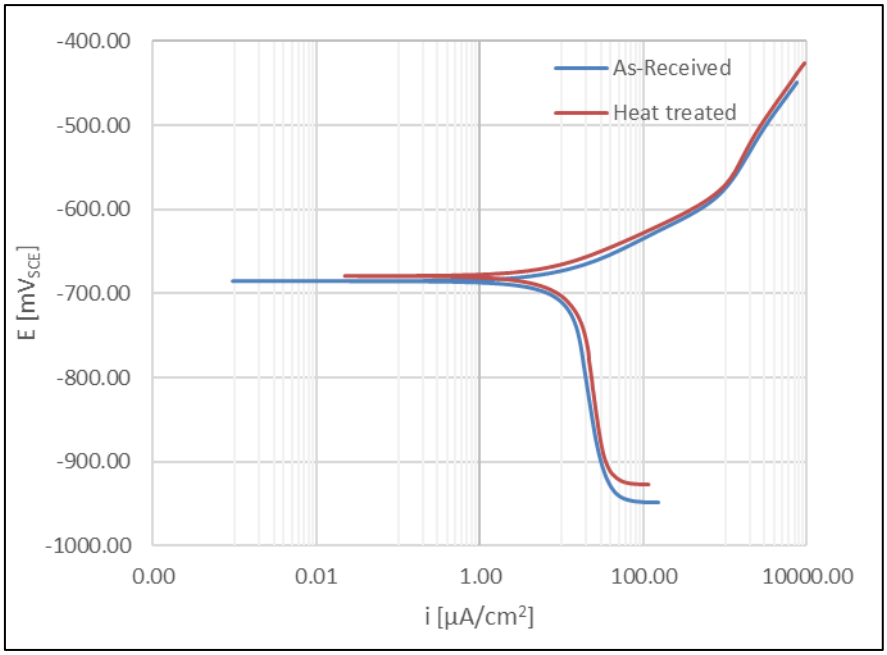

Figure 45: Potentiodynamic polarisation curves for HY-80 steel in as-received and heat-treated conditions.

From Figures 45, it is observed that the potentiodynamic behaviour is almost identical between samples, which is expected given the similarities in microstructure identified in Section 5.2. The average corrosion potential of the heat-treated steel is more positive than that of the as-received steel, which would theoretically mean that the latter is more likely to corrode spontaneously when referring to Eq. 2.3.4. The difference, however, is very small and there is some overlapping of data between heat treated and as-received steel.

Both curves show clear diffusional effects in the cathodic region. This is attributed to the presence of dissolved oxygen in the solution. Although the cathodic branch of the polarization curve shows linearity over a large potential range, it is not exhibiting Tafel behaviour as the whole linear section spans less than one decade of current.

The anodic curves between samples are also similar. The curve shows linear behaviour close to the corrosion potential with an increase in gradient at higher overpotentials, which indicates a degree of passivation. It is speculated that the

mounting method is responsible for this phenomenon, as it was observed that corrosion product filled in and was held in place by the small indentation in the mounting material as the electrode was oxidised.

5.3.1.1 Corrosion rate determination with Echem Analyst

Gamry Echem Analyst software was used to estimate the Tafel slopes and corrosion current density for the selected portions on the potentiodynamic curves as shown in Figure 46. The modelled curve fitted the data very well, but unfortunately Echem analyst cannot consider the effect of diffusion-controlled processes in the analysis. Echem analyst interprets the curve as if it was purely under activation control resulting in an apparent Tafel slope that is much higher than the actual Tafel slope for an activation controlled cathodic processes.

The corrosion current density is used directly in Eq. 2.5.6 along with the determined density and composition for determination of corrosion rate.

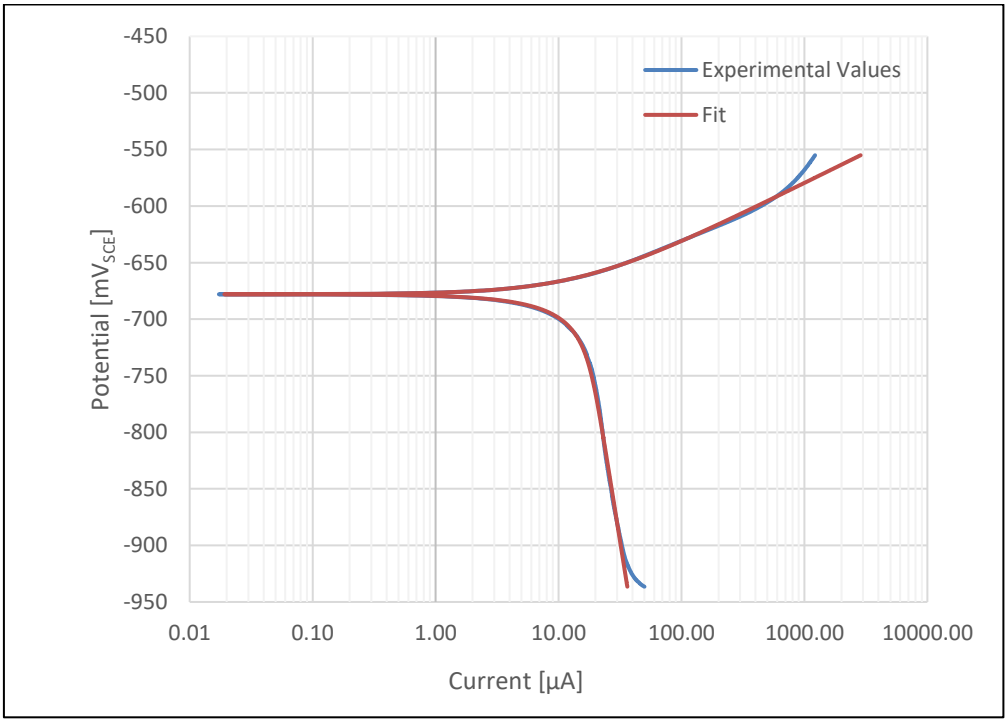

Figure 46: Typical potentiodynamic Tafel fit by Gamry Echem Analyst.

5.3.1.2 Manual extrapolation

It is possible to make an estimation of the corrosion current by extrapolating only one of the polarization curves to the corrosion potential. Cai (Cai, Wen and Jin,

2017) and Yuan (Yuan *et al.*, 2018) estimated corrosion currents for carbon steels in 3.5% NaCl solutions by extrapolation of linear Tafel regions in the anodic polarization curve. Moller (Möller, Boshoff and Froneman, 2006) performed similar extrapolations for mild steel in seawater using only cathodic polarization curves which did not exhibit clear Tafel regions. Möller validated these results with immersion tests. Manual extrapolation of the anodic and cathodic curves on a potential-current density plot (Figure 47) yielded similar results to those obtained in automatic curve fitting in Echem analyst (Table 18). The apparent cathodic Tafel slopes are also reported.

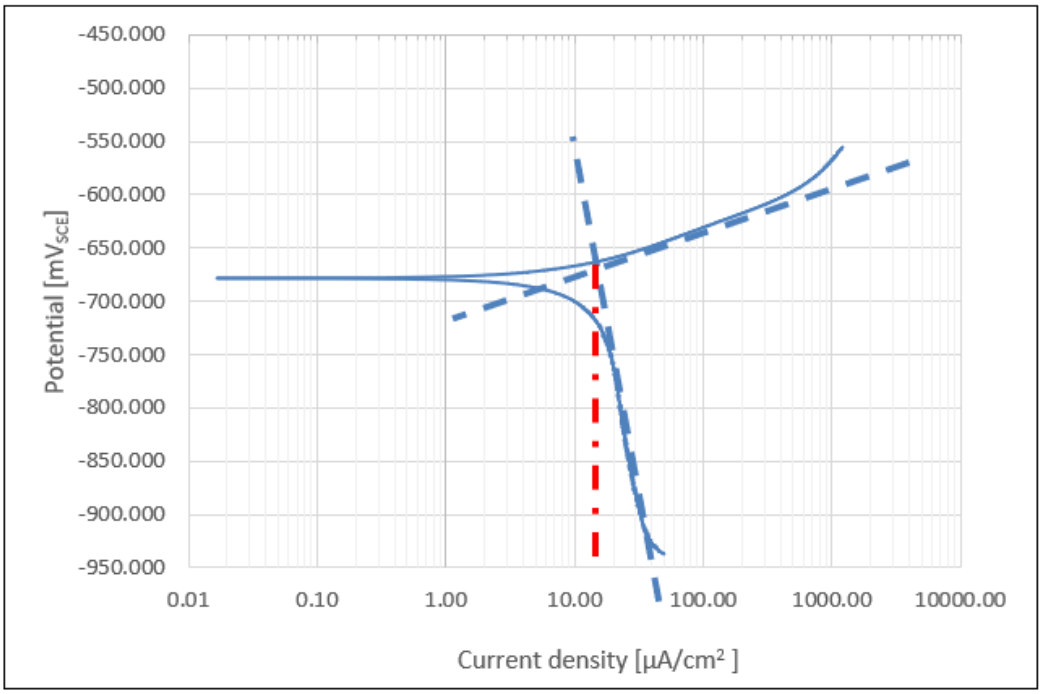

Figure 47: Manual extrapolation of the linear regions of potentiodynamic curves.

A non-linear curve fitting technique, as described by Cai (Cai, Wen and Jin, 2017), in which experimental data is fitted to the total polarization equation (Eq. 2.3.7) using a nonlinear regression analysis function, *fitnlm* in Matlab, was attempted. This technique, although very promising initially, did not produce reliable results. The model seemed to be insensitive to some of its parameters, particularly b_c and i_L. The technique was criticized by Zang (Zhang *et al.*, 2019) for being sensitive to data errors and initial values given to the nonlinear regression analysis. The results of this analysis were omitted.

Table 18: Average potentiodynamic results

Method	Sample	Rp [Ω]	b_a [mV/dec]	b_c – Apparent [mV/dec]	E_{corr} [mV]	i_{corr} [µA/cm^2]	Corrosion rate [mm/yr]
Automatic Curve fitting	HY-80 AR	995 ± 50	55 ± 7	665 ± 43	681 ± 3	14.76 ± 1.27	0.17 ± 0.01
	HY-80 HT	900 ± 77	60 ± 8	530 ±100	675 ± 8	16.16 ± 1.10	0.18 ± 0.01
Manual Extrapolation	HY-80 AR	998 ± 63	50 ± 6	620 ± 76	681 ± 3	15.13 ± 1.25	0.17 ± 0.01
	HY-80 HT	906 ± 85	50 ± 9	590 ±89	675 ± 8	15.58 ± 1.10	0.18 ± 0.01

5.3.2 Polarization resistance technique

The polarization technique is valuable in determining the instantaneous corrosion rate of assets in service, therefore assessing the applicability and accuracy of the technique is important.

Polarization resistance as calculated with Echem Analyst's curve fitting routine corelated well with that calculated in Matlab as the slope of the overpotential-current curve (Figure 48) as discussed in Section 2.3.4.2. This yielded polarization resistance values very close to those predicted in Echem Analyst.

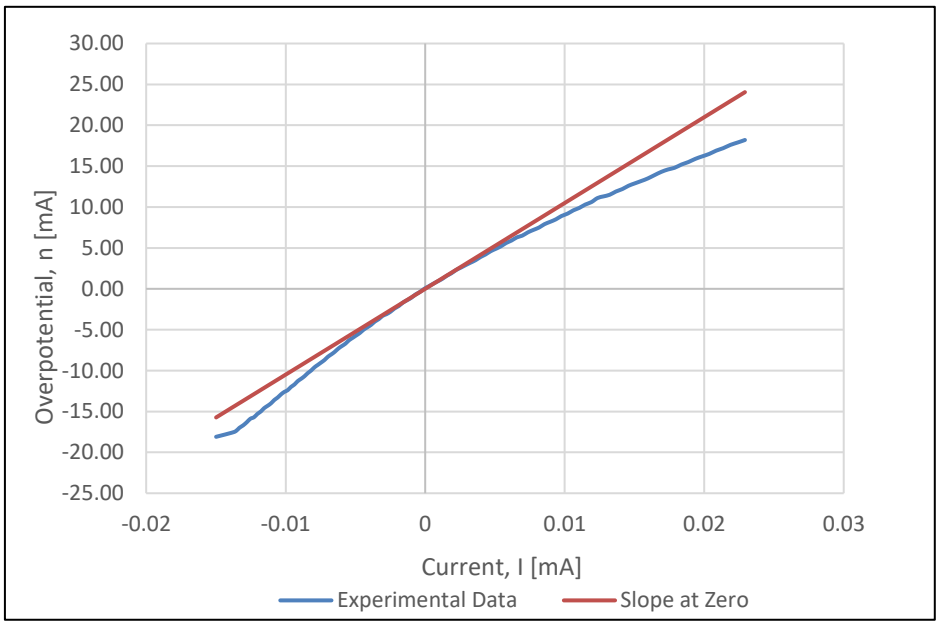

Figure 48: Polarization resistance technique

As discussed earlier, dynamic polarization results showed that the cathodic portion of the polarization curve is under mixed control. Referring to the

polarization resistance theory in Section 2.3.4, it is known that the Stern-Geary equation is not valid when diffusional effects are present and therefore the Mansfeld method as described in Section 2.3.4.2 could not be applied. The ASTM G102 standard (1989) recognizes that systems under mixed control will display a Stern-Geary constant, *B*, that is higher than the actual constant for a system under purely activation control. The standard suggests that two different Stern-Geary constants be calculated so that the actual corrosion current is taken as some value between the resulting upper and lower current estimations. The upper Stern-Geary constant is calculated by assuming that the cathodic Tafel slope, b_c, is parallel to the potential axis and therefore i_{corr} is equal to i_L. This assumes that the rate-controlling step is purely under diffusional control. The resulting Stern-Geary constant is then calculated using only the anodic Tafel slope (ASTM Standard G102, 1989):

$$B_{upper} = \frac{b_a}{2.303} \tag{5.3.1}$$

For a lower limit estimation, the Stern-Geary is calculated using the apparent cathodic Tafel slope:

$$B_{lower} = \frac{b_a b_{c-Apparent}}{2.303\left(b_a + b_{c-Apparent}\right)} \tag{5.3.2}$$

The corrosion current densities for the upper and lower limits are then calculated according to:

$$i_{corr} = \frac{B}{R_p} \tag{5.3.3}$$

Finally, corrosion rate is then determined using Eq. 2.5.9. A sample calculation of the polarization technique can be viewed in Appendix B.

Table 19: Polarization resistance results

Material Condition	R_p [Ω]	B_{lower} [V]	B_{upper} [V]	Lower i_{corr} [µA/cm^2]	Upper i_{corr} [µA/cm^2]	CR [mm/year]
As-recieved	998	0.022	0.024	15.47	16.75	0.18-0.20
Heat treated	906	0.024	0.026	19.38	19.88	0.20-0.23

5.3.3 Immersion corrosion

Immersion corrosion tests served the dual purpose of verifying electrochemically obtained corrosion rates as well investigating the effect of corrosion scale on the corrosion rate of samples. Immersion corrosion was performed on two sets of

specimens for 14 and 30 days at 25°C. The samples were measured using a digital Vernier and micrometer in order to determine the exposed area as accurately as possible, as they showed slight variations in dimensions after manual polishing and cutting with a hacksaw. Samples were weighed to a resolution of 0.1 mg and immediately immersed in seawater.

Figure 49 shows the corrosion product evolution over 30 days. After 2 days a thick corrosion product was formed on the steel surface in isolated “islands”. The film gained thickness and spread across most of the sample surface over the 30-day period. Certain areas on the samples did not exhibit the same behaviour, with only small deposits forming and tarnishing taking place, these areas are assumed to be cathodic sites and regions where thick corrosion product was formed is assumed to be anodic.

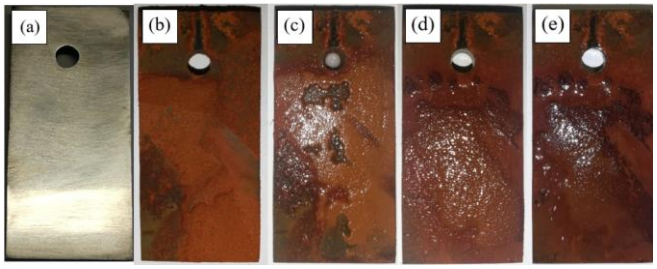

Figure 49: Corrosion evolution on a sample surface after 0 (a), 2 (b), 15 (c), 21 (d) and 30 days (e) immersion in seawater.

Microscopic evaluation of the thick corrosion product on 14-day samples revealed a soft, porous structure (Figure 50). This corrosion product flaked off naturally on some samples, revealing a dark corrosion product underneath.

Figure 50: Corrosion product on heat treated and as-received steel.

Initial cleaning of the samples was performed by rinsing the steel in distilled water and wiping the bulk of the corrosion off by hand. Loose corrosion product

is assumed to come off naturally in actual operation (Fontana, 1987). Washing off the external corrosion product revealed small adherent deposits. More adherent corrosion product could prove to be protective of the base material if enough surface area could be covered. Long-term immersion tests in a natural environment would be invaluable to determine the effect of corrosion product on the corrosion rate of the steel over extended periods.

Final cleaning of the samples consisted of cathodic treatment using a 304 stainless steel anode in an electrolytic solution for 20 minutes with a current density of 200 A/m^2 as described in Section 3.4.5. The steel was removed periodically and rinsed and brushed to remove loosened corrosion product. Samples were wiped and dried with ethanol before final weighing. A reference sample was subjected to the same cleaning procedure, no change in weight was observed.

Table 20 shows the calculated corrosion rates for the immersion samples. An average corrosion rate of 0.192 and 0.190 was calculated for as received and heat-treated samples after 14 days, respectively. Mass loss between duplicate samples were very similar, the variation was within the 10% permitted by the ASTM G31-12a standard between duplicate samples. Corrosion rates after 30 days also showed consistency between samples. The variation in corrosion rate between the heat treated samples was high, but within the allowable range. Corrosion rates after 30 days decreased significantly, this is attributed to the formation of a hard corrosion cap. It is anticipated that this cap would not be able to form under real service conditions where the corrosion product would be stripped off continuously while it is still soft. However, further investigation into the behaviour of HY-80 in service would have to be conducted to confirm this assumption.

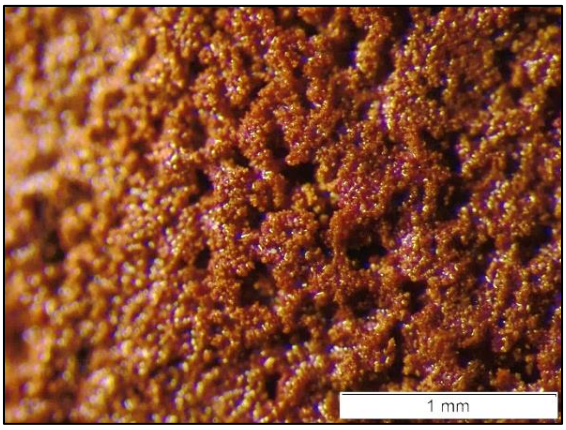

Figure 51: Optical micrograph of corrosion product on HY-80 steel immersed for 15 days in seawater.

Table 20: Immersion corrosion test results.

Time	Sample material condition	Mass loss [g]	Corrosion rate [mm/year]
14 Days	**As received**	0.1677	0.193
		0.1670	0.191
	Heat-treated	0.1699	0.194
		0.1644	0.187
30 Days	**As received**	0.2585	0.141
		0.2636	0.143
	Heat-treated	0.2628	0.143
		0.2874	0.156

5.3.4 Comparison and conclusion of corrosion testing results

This section of experimental work was conducted to satisfy the first two research objectives. The corrosion rate was determined and verified using 3 different techniques. The kinetic parameters of the corroding system were identified and used in the polarization resistance technique.

Electrochemical and 14-day immersion tests compared relatively well. Immersion tests showed corrosion rates slightly higher than those estimated in the potentiodynamic polarization tests for as-received steel and almost identical rates for heat-treated steel. The polarization resistance technique was also quite accurate, even though the cathodic slope did not show Tafel behaviour. Estimated corrosion rates were higher than those predicted with the potentiodynamic technique but the lower bound of corrosion rates estimated in Table 19 using the apparent cathodic Tafel slope was fairly accurate. This proved that the recommendation by the ASTM G102-89 standard to estimate an upper and lower corrosion current for calculation of the corrosion rate is valid for this scenario and that in-situ testing could yield reasonably accurate corrosion rate estimations.

Maximum corrosion rates estimated in Section 5.1.4 was only slightly higher than that predicted by potentiodynamic and immersion tests. From the average historical corrosion rate predicted in Section 5.1.4 it is concluded that the submarine hull is in overall good shape. The high maximum penetration would have to be monitored in the future, but the current corrosion model that shows a corrosion rate of 0.18 mm/year could be used as guideline.

The second set of immersion corrosion samples showed a significant reduction in corrosion rate, as estimated by electrochemical and 14-day immersion tests, which is attributed to the formation of a hard, adherent corrosion product. This could explain why the average estimated corrosion rates as measured on the actual submarine was much lower than the experimentally obtained results. Further studies into the effectiveness of the submarine coating and effect of fluid flow would have to be conducted to establish the cause of variation in material loss.

6 Simulation Results and discussion

6.1 Mesh convergence studies

A mesh convergence analysis was performed to ensure that the analysed mesh was sensitive enough for accurate results without being unnecessarily detailed. This reduced computational time greatly, seeing that 16 wall thicknesses were tested. Four different mesh sizes are represented in Table 20 where the lowest number of elements is 1938 and the highest 96985. The meshes were perturbed using the Matlab code as discussed in Section 4.2.2 and imported back to the FEA software for analysis. This step was important seeing that the out-of-circularity will affect the collapse pressure directly. The interframe mode n_i=16 was expected to be sensitive to element size seeing that 4 circumferential lobes were present along the perimeter of a quarter shell.

Table 21: Mesh convergence analysis as performed on an eighth model.

Number of Nodes	Number of Elements	Collapse pressure
1938	1818	5.318
37000	36531	5.650
80100	79417	5.648
97744	96985	5.647

From Table 21 it is seen that the results obtained from a mesh with 36531 elements were only about 0.1% different from that obtained in the finest mesh with 97744 nodes. However, it was anticipated that some extra resolution in the mesh might be useful in identifying collapse modes, especially at reduced wall thicknesses where the collapse mode could become more localized. It was decided to use the 79417-element mesh which corresponded to 149 elements along the perimeter of the quarter model shell plating, 8 elements in the web height of a stiffener and 4 elements across the flange width of a stiffener. An example of mesh density is shown in Figure 52.

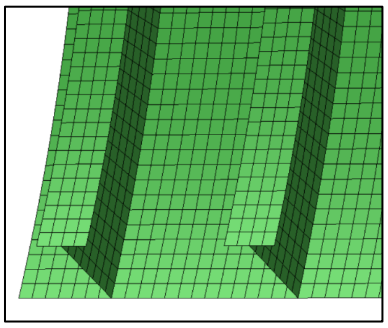

Figure 52: Example of mesh density

6.2 Verification of critical imperfection modes

From initial calculations it was anticipated that the most critical mode numbers would be $n_o = 2$ and $n_i = 16$. Mode numbers $n_o = 3$ and $n_i = 15$ were also tested using the different boundary conditions as discussed in Section 4.2.3.

Table 22 shows the estimated collapse pressures of the imperfect models using different boundary condition cases. The collapse pressures were normalised according to a reference model where $n_o = 2$, $n_i = 16$ and two circumferential symmetry constraints were in place as shown in Figure 35. It is shown that models mode numbers 15 or 16 yields almost identical collapse pressures. The weak spring model is shown to be more accurate than the assumption of a perfectly stiff deep frame stiffener and therefore the radially constrained deep frame stiffener results were not considered for further analysis. Using an overall imperfection of $n_o = 3$ increases the collapse pressure. The conclusion was made that the model with $n_o = 2$ and $n_i = 16$ out-of-circularity errors and boundary conditions as shown in Figure 35 would be the most accurate considering that no artificial stiffening is in place in the radial directions.

Table 22: Normalised collapse pressures of models with different boundary conditions and imperfection mode numbers.

n_o	n_i	Eighth model	Radially constrained deep frame stiffener	Weak spring
2	16	1	1.05	0.995
2	15	-	1.05	0.995
3	16	-	1.025	1.023
3	15	-	1.014	1.026

6.3 Effect of phase alignment

Two different phase alignments were investigated to ensure that estimated buckling load is at a minimum for the applied imperfections. The first alignment (Figure 53(a)) is where the maximum amplitudes of the out-of-circularity errors are aligned. The minimum amplitudes were aligned for the second case (Figure 53(b)). It was found that the collapse pressures are almost identical for this combination of OOC mode numbers. This can be attributed to the fact that the interframe OOC amplitude is relatively small in comparison to the large overall amplitude. Furthermore, the overall mode's gradient is very even across the narrowest section in the imperfect circle, meaning that the adjacent trough of the interframe mode will align with and overall mode amplitude that is almost identical to the minimum amplitude.

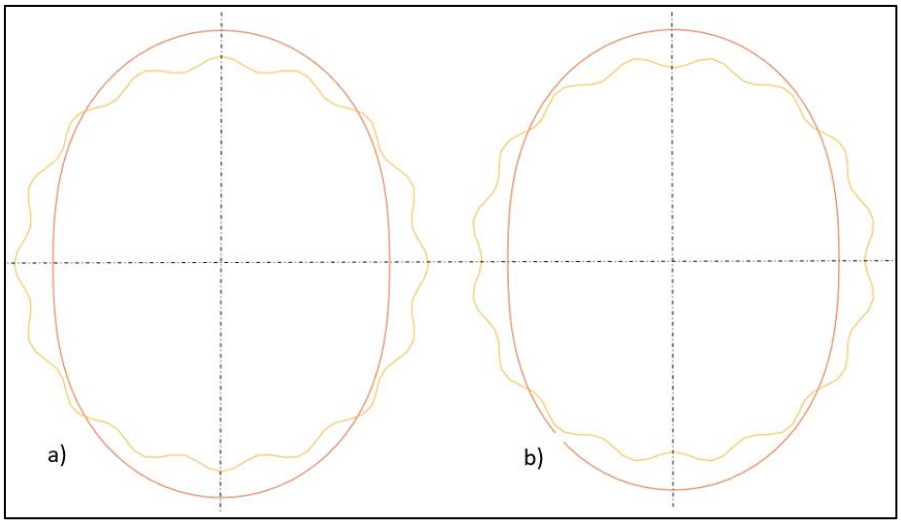

Figure 53: Exaggerated OOC phase alignments for a cross-section of submarine hull.

Table 23: Effect of phase alignment on the normalised collapse pressures.

Wall thickness	25 mm	22 mm
Case a	1	0.92
Case b	0.99	0.91

6.4 Failure analysis

6.4.1 Initial yielding

All 16 tested wall thicknesses showed similar yielding behaviour. Initial yielding of the shell plating took place over the deep-frame stiffener as a result of excessively high longitudinal bending strains caused by the relatively stiff plane. These stress estimations would have been amplified if boundary conditions, such as those utilised by Gannon (2010) and Smith (2015), were implemented in which the bulkhead nodes were completely constrained in the radial direction. Burcher (1995) suggests that adjacent stiffener spacing be moved toward the bulkhead/deep-frame stiffener in order to increase the safety factor against yielding or that hull thickness could be increased locally to ensure that yielding does not take place. It is not known if the hull plating is reinforced around the deep-frame stiffeners in the investigated submarine.

The FE-analysis also showed that the stiffening rings at the centre of the submarine hull, where OOC is at its maximum yielded under compression which led to ultimate collapse of the structure. It is believed that this yielding pressure constitutes failure rather than the yielding of shell plating.

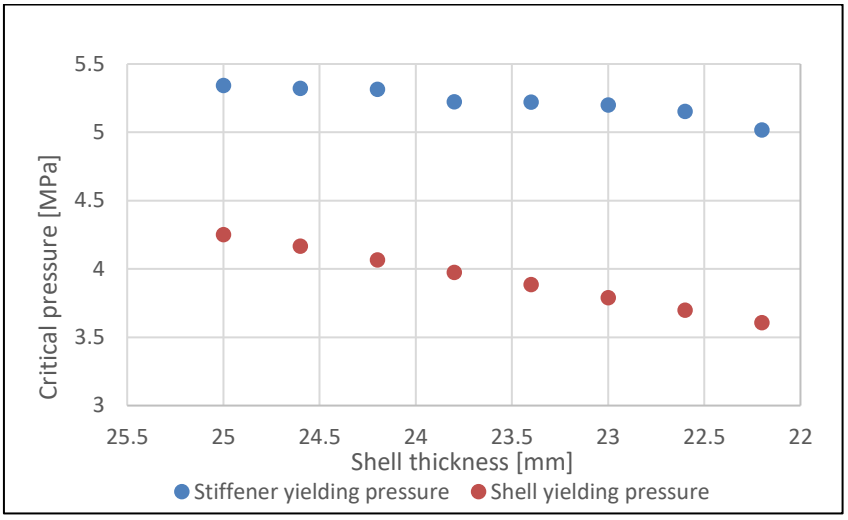

Figure 54: Numerically estimated yielding pressures for the analysed submarine hull.

6.4.2 Prediction of ultimate collapse pressure

Figure 55 shows the load-displacement curve of an intact hull for a node at the lowest out-of-circularity point (-15.75 mm). The curve shows a gradual displacement with an increase in pressure. A peak value is reached, after which the displacement of the investigated node increases very rapidly, indicating buckling of the cylinder. It is observed from the displacement contour plot in Figure 56 that the cylinder buckles in the overall mode (n_o = 2) initiated by yielding of the stiffeners as shown in Figure 57.

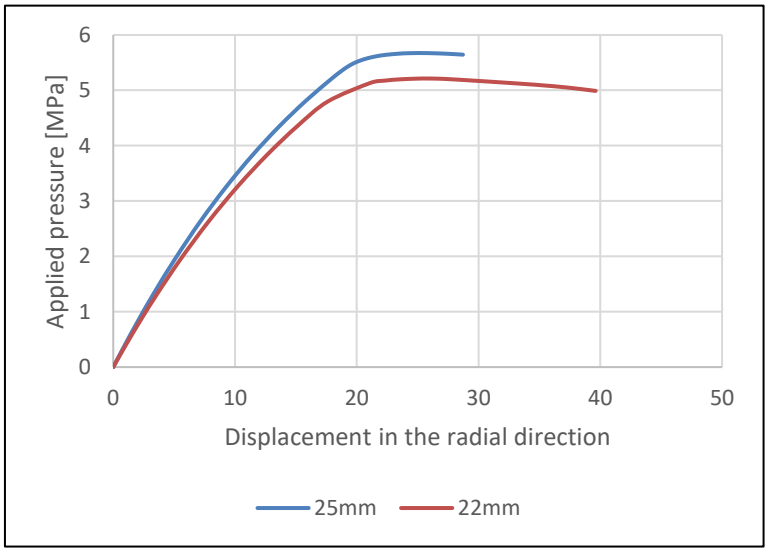

Figure 55: Load-displacement curve for the node experiencing maximum displacement.

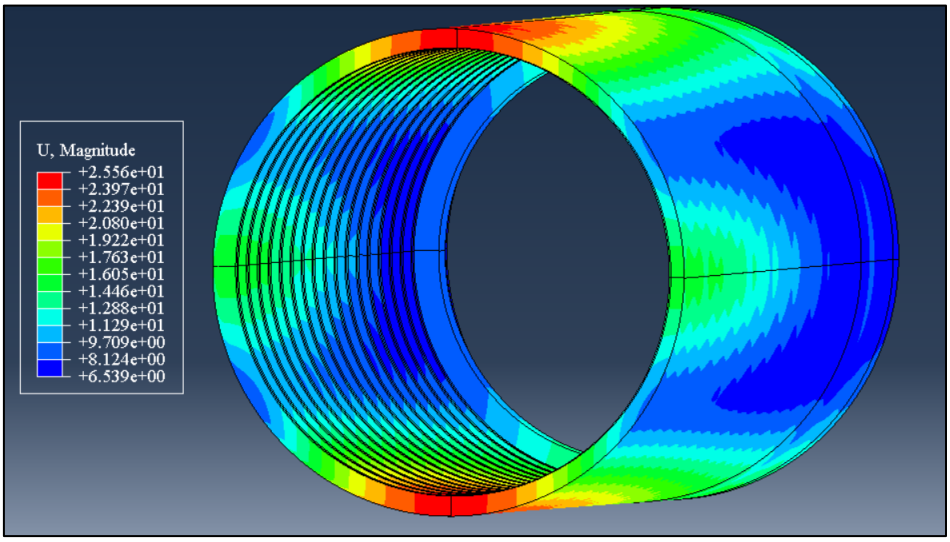

Figure 56: Displacement contour plot showing overall collapse (n_0=2).

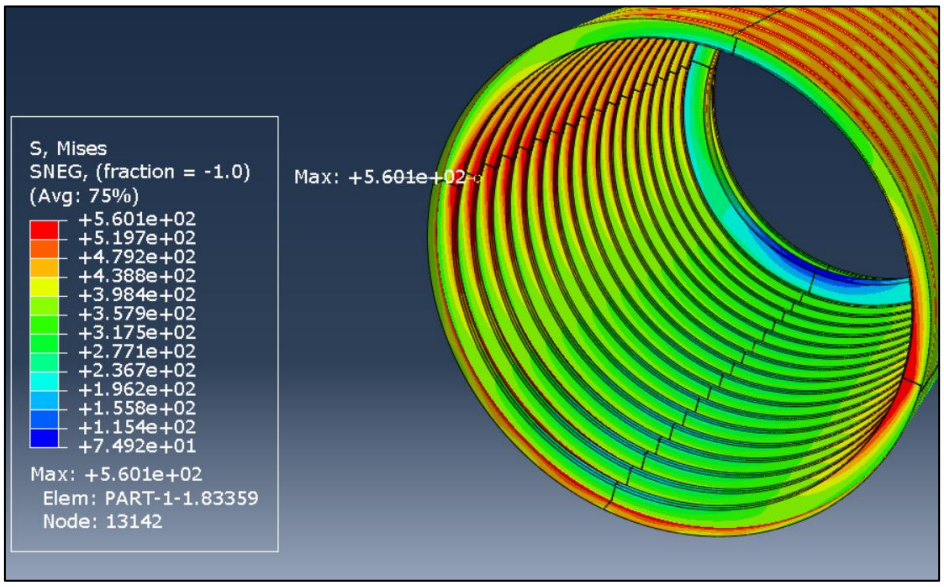

Figure 57: Yielding of stiffening rings where the OOC was at a maximum peak.

For wall thicknesses below 22.8 mm, the same stiffener yielding is observed, but before overall collapse can take place, the shell buckles locally where the OOC is at its lowest point as shown in Figure 58. Buckling is therefore initiated by instability of the thinned shell plating along with the instability of stiffeners.

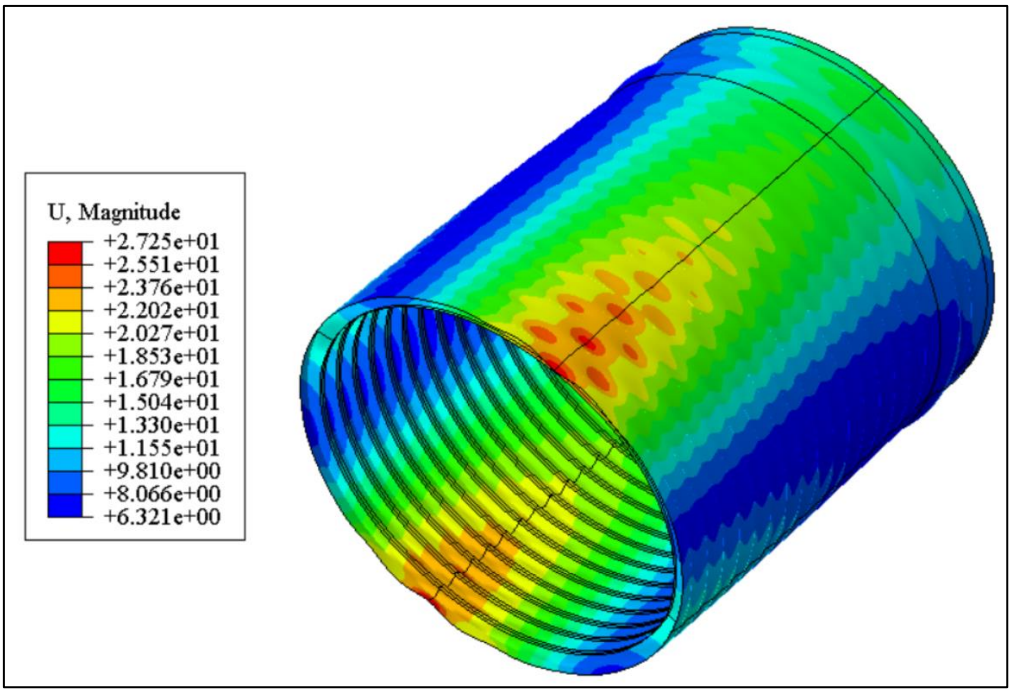

Figure 58: Post-collapsed shape of the pressure hull showing large local displacements where the OOC was at its highest negative point.

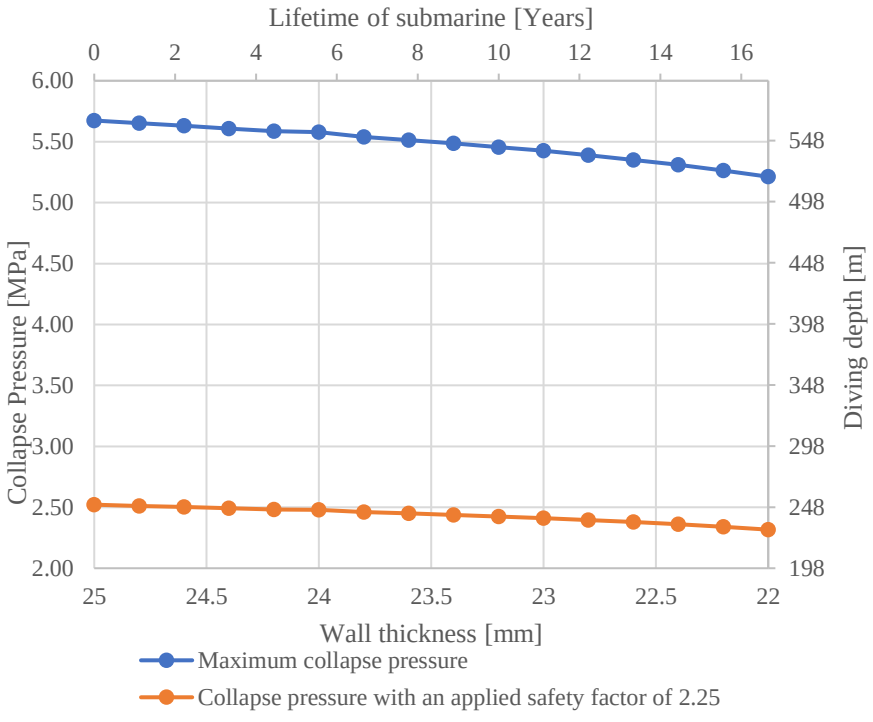

Figure 59: Collapse pressures of the investigated hull as shell plating is thinned.

The collapse pressure of a submarine hull was found to vary mostly linearly with wall thinning. An approximate slope of -0.15MPa per millimetre of thinning was observed in the range of wall thicknesses investigated. This translates to a reduction in operating pressure of ~27 kPa per year of operation for an estimated corrosion rate of 0.18 mm/year. Cho et al. (Cho *et al.*, 2018) also reported a linear relationship between thinning of shell plating and collapse pressures as calculated with empirical formulas. Gannon (2010) investigated the effect of local thinning representing a corrosion patch on the collapse pressure of a submarine pressure hull, and even though the results were not plotted or discussed, they appear to be very linear for the 5-20% thinning range.

A safety factor of 2.25 against buckling was calculated based on the normal operational depth of 250 m (Jones, 1997; Torkelson, 2005) for the uncorroded structure. A second plot on Figure 59 shows the actual normal diving depth with the original safety factor in place. After 16 years of operation, the normal diving depth is estimated to be approximately 231 m. Current collapse pressure is estimated to be 5.43 MPa. With a safety factor of 2.25, this is reduced to 2.41 MPa which relates to approximately 240 m diving depth.

7 Conclusions

The purpose of this study was to investigate the how the uniform corrosion thinning affects the collapse pressure of a submarine pressure hull.

The study considered two different material states, namely heat treated and as-received steel. A heat treatment procedure was applied to HY-80 to simulate a post-manufacture stress relieving cycle. Steel was heated to 590°C and held at this temperature for ninety minutes, after which the steel was allowed to cool down in air.

Mechanical properties of the different states of the steel was investigated and compared. Original material properties had to be determined as the acquired steel was not supplied with a material data sheet. The effect of heat treatment on the mechanical properties of the steel was minimal, with a reduction in ultimate tensile- and yield strength of only 13 MPa and 3 MPa, respectively, for the 10 tensile samples tested. This result was verified with Vickers hardness testing that showed a difference of only 6HV1 between material states.

Optical microscopy was conducted to investigate any visible changes in microstructure as a result of heat treatment. As expected from the consistency in mechanical properties, the microstructures were almost identical. The microstructure was confirmed to be a martensitic bainitic duplex structure as described in the literature. The composition of the steel was determined by SEM and EDS and compared well to the ranges specified in the literature. EDS results were used in the corrosion analysis.

Corrosion analysis was performed using polarization and immersion techniques. A corrosion rate of 0.17 mm/year and 0.18 mm/year was calculated for the as received and heat-treated steel respectively using the potentiodynamic polarization technique with manual as well as automatic curve fitting. It was observed that the rate determining step was largely controlled by oxygen diffusion to the sample surface and therefore corrosion results had to be verified using additional techniques.

The applicability of the polarization resistance technique was investigated and compared well with the results obtained in the full potentiodynamic analysis with rates of 0.18-0.20 mm/year and 0.20-0.23 mm/year estimated for non-heat treated and heat-treated steels, respectively. The Stern-Geary constant used for this estimation was determined to be 22-24 mV for as-received steel and 24-28 mV for heat-treated steel. These ranges were estimated as per the requirement in the ASTM G102-89 standard in which the upper estimation assumes that the corrosion process is completely under diffusional control and the lower estimation is based on apparent Tafel slope of the cathodic process under mixed control.

The electrochemically obtained corrosion rates were verified by immersion testing of steel coupons for 14 and 30-day periods. Corrosion rates obtained in the initial stage of immersion was found to be consistent with those estimated in electrochemical tests with an average corrosion rate of 0.19 mm/year for both material conditions. Longer immersion tests showed that corrosion product slowed the corrosion rate. It was assumed that thicker corrosion product would be stripped off while the vessel is in motion, but long-term testing would have to be conducted to confirm this assumption.

Actual measurement of hull thickness was performed on a submarine that was undergoing reparations and refurbishment. It was found that the maximum loss of material was 2.01 mm with an average loss of 1.15 mm after an estimated 10 years in service. For the purposes of this study it was assumed that all the material lost was because of corrosion and that the original thickness of material was 25 mm, neglecting any variation in thickness due to manufacturing. This yielded and a maximum corrosion rate of 0.20 mm per year over the 10-year service life of the submarine.

The literature review showed that FEA analysis of submarine hull structures could be simplified by only analysing the most critical section. Nonlinear submarine collapse is largely influenced by the out of circularity errors that will determine the collapse mode.

A finite element model with applied interframe and overall out-of-circularities, considering material and geometrical nonlinearities was analysed. A Matlab script was used to control the shape and phase of the multiple out-of-circularity modes. It was found that for the longest submarine compartment, with a total length of 15.05 m, the most critical overall mode was n_o=2. The critical interframe mode was found to be n_i=16. The Riks method was used to investigate post-collapse behaviour and it was determined that the submarine would buckle in an overall mode for wall thicknesses between 25 mm and 22.8 mm. It was observed that the buckling mode became very localised below a thickness of 22.8 mm. With an intact hull, the estimated buckling pressure was found to be 5.64 MPa, indicating a safety factor of 2.25 for a normal operational depth of 250 m. Buckling was preceded by the yielding of tee stiffeners at the centre of the compartment were the OOC was at a maximum. For an intact pressure hull, stiffeners began to yield at 5.22 MPa, indicating a safety factor of 2 against stiffener yielding.

Based on a corrosion rate estimation of 0.18 mm/year, it is estimated that the maximum collapse pressure will reduce by 27 kPa per year. It is recommended that the operational limits of the submarine under investigation be reduced to 240 m.

8 Recommendations

The assumption of perfect uniform corrosion over the whole structure provides a good worst case scenario for estimation of corrosion rate, but actual measurements of a submarine hull showed that the variation in corrosion rate is significant along the length of the structure. This could have been amplified by variation in wall thickness caused by manufacturing processes. Using the thickness values obtained in this study, more accurate estimations of in-service corrosion rates could be made in the future.

The effect of fluid flow could be investigated using specialised equipment such as rotating disk electrodes or simulated flow conditions in immersion testing. Seeing that a submarine is a mobile object that can travel at many different speeds, it would be difficult to compile an accurate model of thinning over time. It would be best to investigate the effect of different flow velocities on the instantaneous corrosion rate of the investigated steel in seawater. This would produce a graph of instantaneous corrosion rate vs. fluid velocity which can be used to estimate total corrosion loss based on travel speed and distance during a mission. This would of course have to be completed internally in the South African Navy as routes and speeds of submarines are national secrets.

More aggressive forms of localized corrosion such as pitting and galvanic corrosion was observed on the submarine. These corrosion mechanisms were observed where stainless steel screws and fittings were threaded into the submarine hull. The phenomenon of corrosion as a result of contact between dissimilar metals is well known and therefore a study could be launched to investigate alternative materials for fittings and bolts that would either minimize corrosion as a result of contact between metals. A cost-effective material that could be replaced periodically could also be recommended.

Finally, penetrations and internal structures were not modelled in the finite element analysis because these details were not made available to the author. The DESUP programme does not authorize staff of the South African Navy or Armscor to make secret information available to students. It is recommended that the whole structure be modelled if enough computing resources is available. This would have to be completed internally or after the submarine is decommissioned and the outstanding information is made available to the public.

9 References

45MG Ultrasonic Thickness Gauge User's Manual. 2016. Waltham: Olympus.

Aka-Brief #7 Stainless and Duplex steels. 2020. Roskilde: AKASEL.

Angst, U. and Büchler, M. 2015. 'On the applicability of the Stern-Geary relationship to determine instantaneous corrosion rates in macro-cell corrosion', *Materials and Corrosion*, 66(10), pp. 1017–1028.

ASTM Standard E8/E8M. 2015a. *Standard Methods for Tension Testing of Metallic Materials.* West Conshohocken: ASTM International.

ASTM Standard G1. 2003 (2011). *Standard Practice for Preparing , Cleaning , and Evaluating Corrosion Test Specimens*. West Conshohocken: ASTM International.

ASTM Standard G31. 2015a. *Standard Guide for Laboratory Immersion Corrosion Testing of Metals.* West Conshohocken: ASTM International.

ASTM Standard G102. 1989 (2010). *Standard Practice for Calculation of Corrosion Rates and Related Information from Electrochemical Measurements.* West Conshohocken: ASTM International.

British Standards Institution PD5500. 2009. *Specification for unfired fusion welded pressure vessels*, London: BSI.

Budynas, R. G. and Nisbett, J. K. 2015. *Shigley's Mechanical Engineering Design*. 10th edn. New York: McGraw-Hill.

Burcher, R. and Rydill, L. 1995. *Concepts in Submarine Design*. Cambridge: Cambridge University Press.

Cai, S. yu, Wen, L. and Jin, Y. 2017. 'A comparative study on corrosion kinetic parameter estimation methods for the early stage corrosion of Q345B steel in 3.5wt% NaCl solution', *International Journal of Minerals, Metallurgy and Materials*, 24(10), pp. 1112–1125.

Callister, W. D. and Rethwisch, D. G. 2015. *Materials Science and Engineering*. 9th edn. Danvers: John Whiley & Sons.

Çengel, Y. A. and Ghajar, A. J. 2015. *Heat and Mass Transfer: Fundamentals & Applications*. 5th edn. New York: McGraw-Hill.

Cerik, B. C. and Cho, S. R. 2013. 'Numerical investigation on the ultimate strength of stiffened cylindrical shells considering residual stresses and shakedown', *Journal of Marine Science and Technology*, 18(4), pp. 524–534.

Cho, S. R. et al. 2018. 'Ultimate strength formulation considering failure mode interactions of ring-stiffened cylinders subjected to hydrostatic pressure', *Ocean Engineering*. Elsevier Ltd, 161(April), pp. 242–256.

Cicek, V. 2014. *Corrosion Engineering*. Hoboken: John Wiley & Sons, Salem: Scrivener Publishing LLC.

Deb, P and Challenger, K. D. 1984. 'TEM characterization of HY-80 steel microstructure after small plastic strain', *Metallography*, (17), pp. 253–272.

Fischer, D. A. et al. 2019. 'The effect of scan rate on the precision of determining corrosion current by Tafel extrapolation: A numerical study on the example of pure Cu in chloride containing medium', *Electrochimica Acta*. Elsevier Ltd, 313, pp. 457–467.

Flitt, H. J. and Schweinsberg, D. P. 2005. 'A guide to polarisation curve interpretation: Deconstruction of experimental curves typical of the Fe/H2O/H+/O2 corrosion system', *Corrosion Science*, 47(9), pp. 2125–2156.

Flitt, H. J. and Schweinsberg, D. P. 2005. 'Evaluation of corrosion rate from polarisation curves not exhibiting a Tafel region', *Corrosion Science*, 47(12), pp. 3034–3052.

Fontana, M. G. 1987. *Corrosion Engineering Mars G. Fontana*. 3rd edn. New York: McGraw-Hill.

Gannon, L. 2010. *TM 2010-246: Submarine Pressure Hull Collapse Considering Corrosion and Penetrations*. Dartmouth: DRDC Atlantic.

Guo, Y. bing et al. 2015. 'Effect of microstructure variation on the corrosion behavior of high-strength low-alloy steel in 3.5wt% NaCl solution', *International Journal of Minerals, Metallurgy and Materials*, 22(6), pp. 604–612.

Hudson, J. C., Stanners, J. F. and Hooper, R. A. E. 1994. '3.2 Low-alloy Steels', in Shreir, L. L., Jarman, R. A., and Burstei, G. T. (eds). *Corrosion: Volume 1*. 3rd edn. Oxford: Butterworth-Heinemann.

Jones, E. R. 1997. *The proliferation of conventionally-powered submarines: Balancing U.S. cruise missile diplomacy? The cases of India and Iran*. Monterey: Naval Postgraduate School.

Kelly, R. G. and Scully, J. R. 2003. *Electrochemical Techniques in Corrosion Science and Engineering*. New York: Marcel Dekker Inc.

Li, Z. et al. 2019. 'Effect of pH and NaCl concentration on the hydrogen evolution reaction of X60 steel', *Anti-Corrosion Methods and Materials*, 66(2), pp. 203–209.

Lins Junior, A. S. et al. 2014. 'Mechanical and microstructural properties of SMAW and GMAW welded joints of HY-80 steel', *Soldagem e Inspecao*, 19(3), pp. 200–211.

MacKay, J. R. et al. 2010. 'Experimental investigation of the strength and stability of submarine pressure hulls with and without artificial corrosion damage', *Marine Structures*. Elsevier, 23(3), pp. 339–359.

MacKay, J. R., Van Keulen, F. and Smith, M. J. 2011. 'Quantifying the accuracy of numerical collapse predictions for the design of submarine pressure hulls', *Thin-Walled Structures.* Elsevier, 49(1), pp. 145–156.

Mansfeld, F. 1973. 'Tafel slopes and corrosion rates from polarization resistance measurements', *Corrosion*, 29(10), pp. 397–402.

MIL-S-16216K. 1987. *Steel Plate, Alloy, Structural, High Yield Strength (HY-80 and HY-100).* Military Specifications and Standards.

Möller, H., Boshoff, E. T. and Froneman, H. 2006. 'The corrosion behaviour of a low carbon steel in natural and synthetic seawaters', *Journal of the Southern African Institute of Mining and Metallurgy*, 106(8), pp. 585–592.

Oktadinata, H. and Winarto, W. 2019. 'Impact toughness of gas metal arc welded HY-80 steel plate at sub-zero temperatures', in MATEC Web of Conferences 269, no.06003.

Oldham, K. B. and Mansfeld, F. 1973. 'Corrosion rates from polarization curves: A new method', *Corrosion Science*, 13(10), pp. 813–819.

Roberge, P. R. 2000. *Handbook of Corrosion Engineering*. New York: McGraw-Hill.

Roberge, P. R. 2008. *Corrosion Engineering: Principles and Practice*. New York: McGraw-Hill.

Rowe, A. A. et al. 2011. 'Cheapstat: An open-source, "do-it-yourself" potentiostat for analytical and educational applications', *PLoS ONE*, 6(9), e23783.

Rowlands, J. C. 1994. '2.4 Sea Water', in Shreir, L., Jarman, R., and Burstei, G. (eds). *Corrosion:Volume 1*. 3rd edn. Oxford: Butterworth-Heinemann.

Smith, M. J., Macadam, T. and MacKay, J. R. 2015. 'Integrated modelling, design and analysis of submarine structures', *Ships and Offshore Structures*. Taylor & Francis, 10(4), pp. 349–366.

Song, C. and Cui, W. (2020) 'Review of Underwater Ship Hull Cleaning Technologies', Journal of Marine Science and Application. Journal of Marine Science and Application, 19(3), pp. 415–429.

Torkelson, K. O. 2005. *Comparative Naval Architecture Analysis of Diesel Submarines*. Cambridge: Massachusetts Institute of Technology.

Yang, Y. et al. 2017. 'Dynamic modeling and motion control strategy for deep-sea hybrid-driven underwater gliders considering hull deformation and seawater density variation', *Ocean Engineering*. Elsevier Ltd, 143(October 2016), pp. 66–78.

Yuan, W. et al. 2018. 'Effects of temperature and applied strain on corrosion of X80 pipeline steel in chloride solutions', *Corrosion Engineering Science and Technology*, 53(6), pp. 393–402.

Zhang, S. et al. 2019. 'Experimental data treatment of the pipeline steel polarization curve under AC interference', *International Journal of Electrochemical Science*, 14, pp. 10888–10906.

Appendix A: Potentiodynamic curves

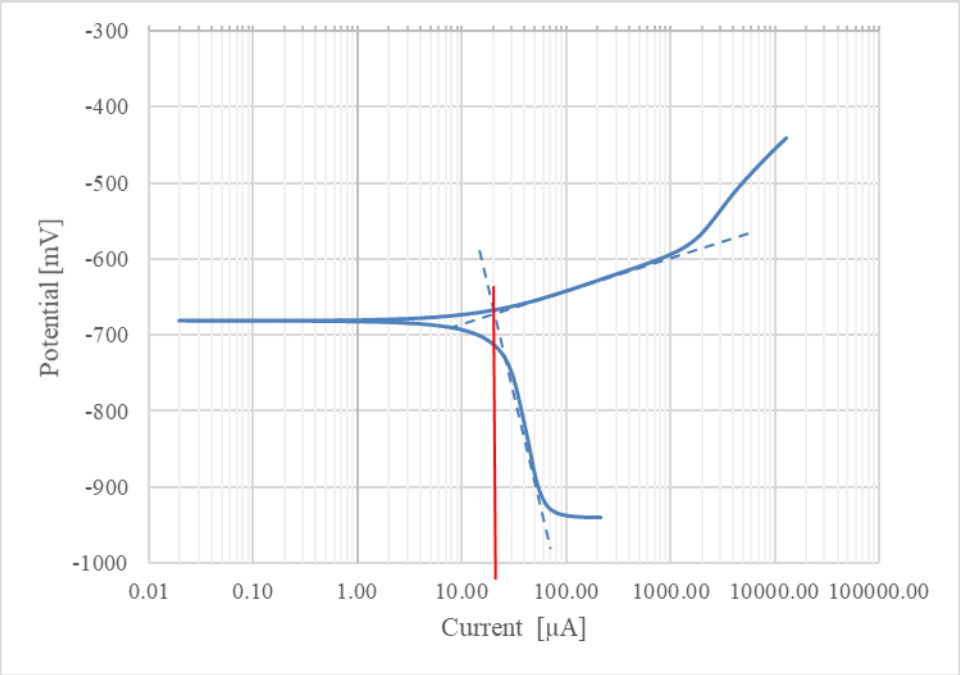

Figure A 1: Potentiodynamic curve of as-received Sample 1

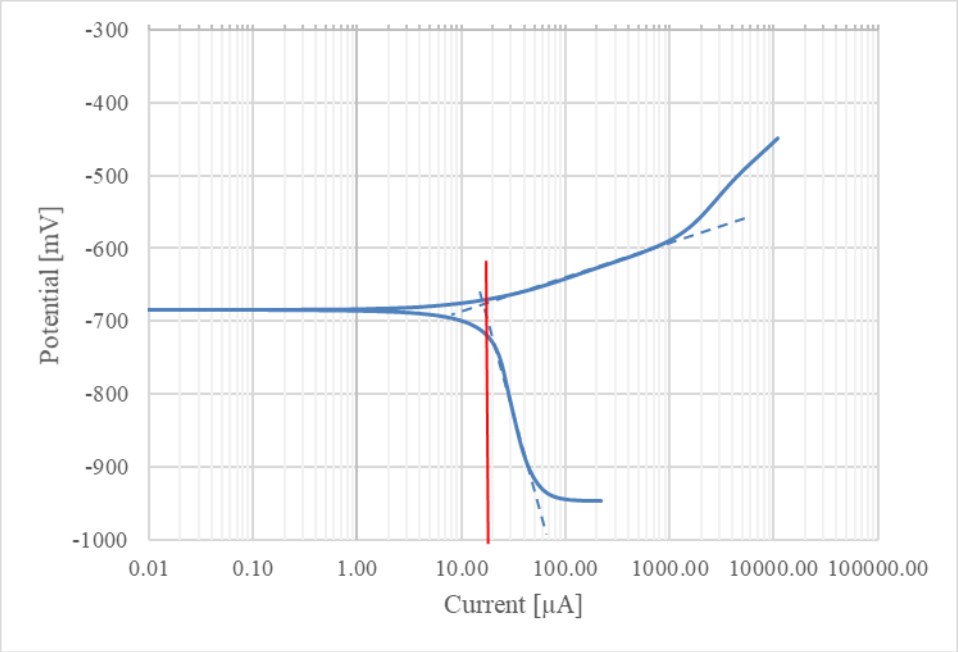

Figure A 2:Potentiodynamic curve of as-received Sample 2.

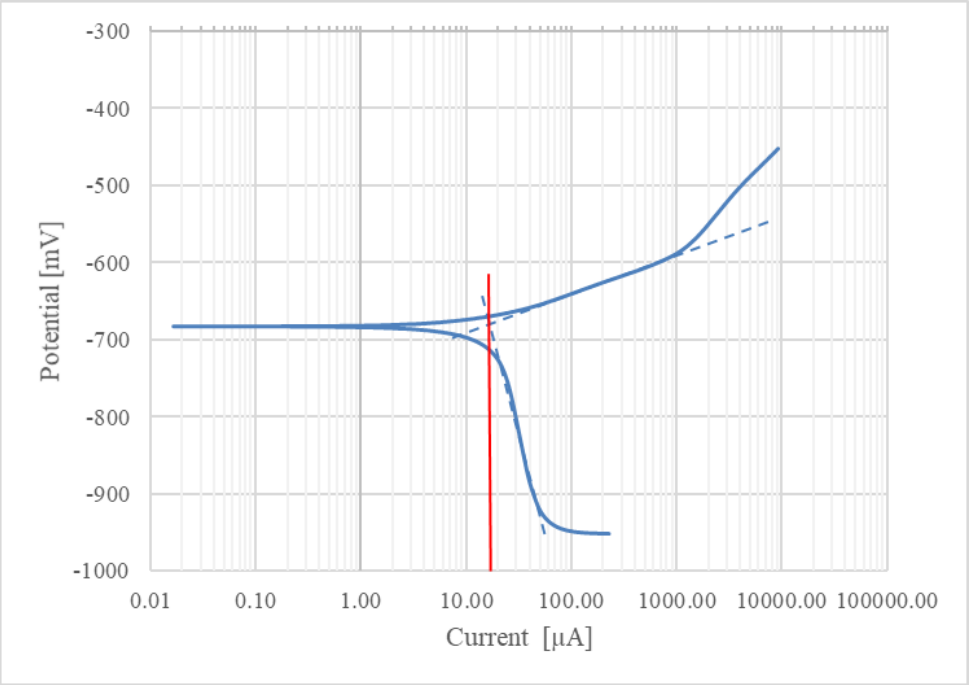

Figure A 3: Potentiodynamic curve of as-received Sample 3.

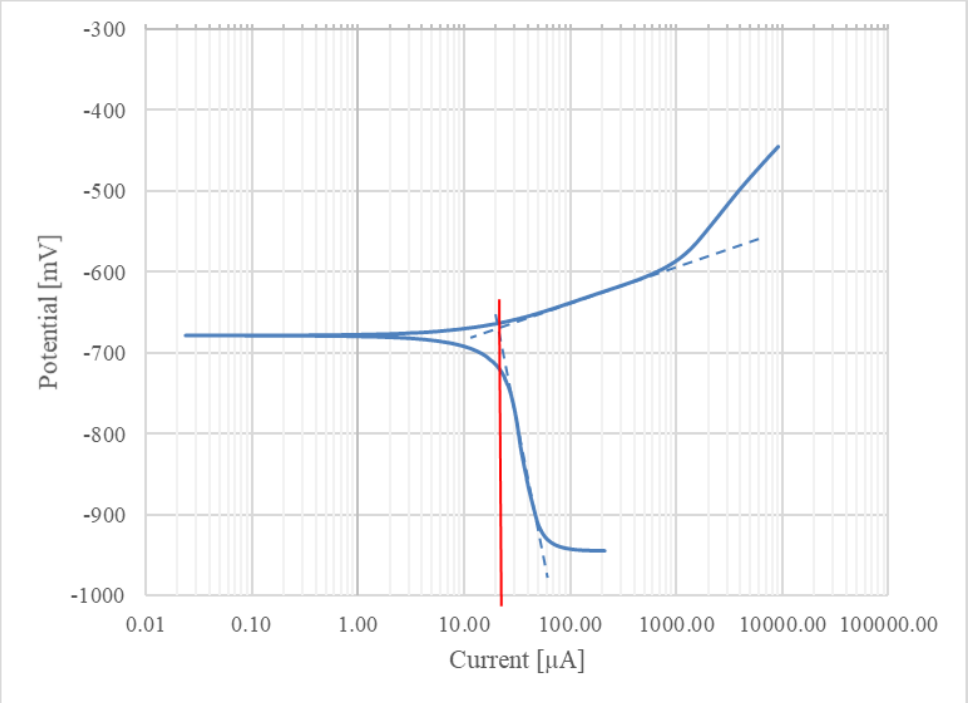

Figure A 4: Potentiodynamic curve of as-received Sample 4.

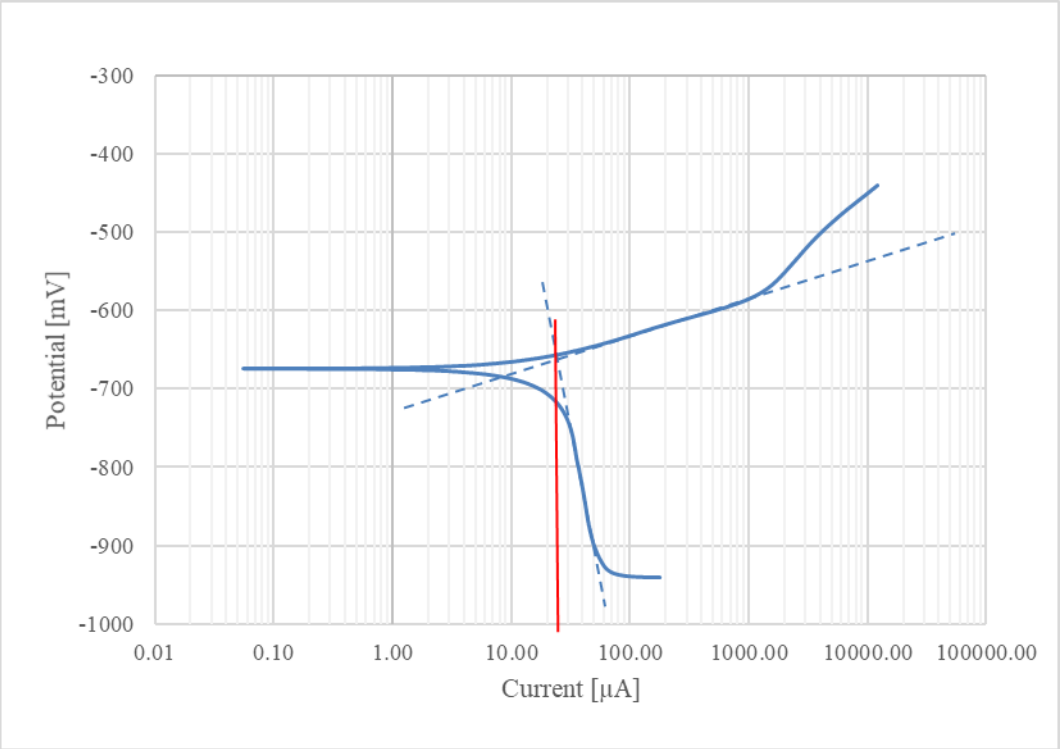

Figure A 5: Polarisation curve of heat treated Sample 1.

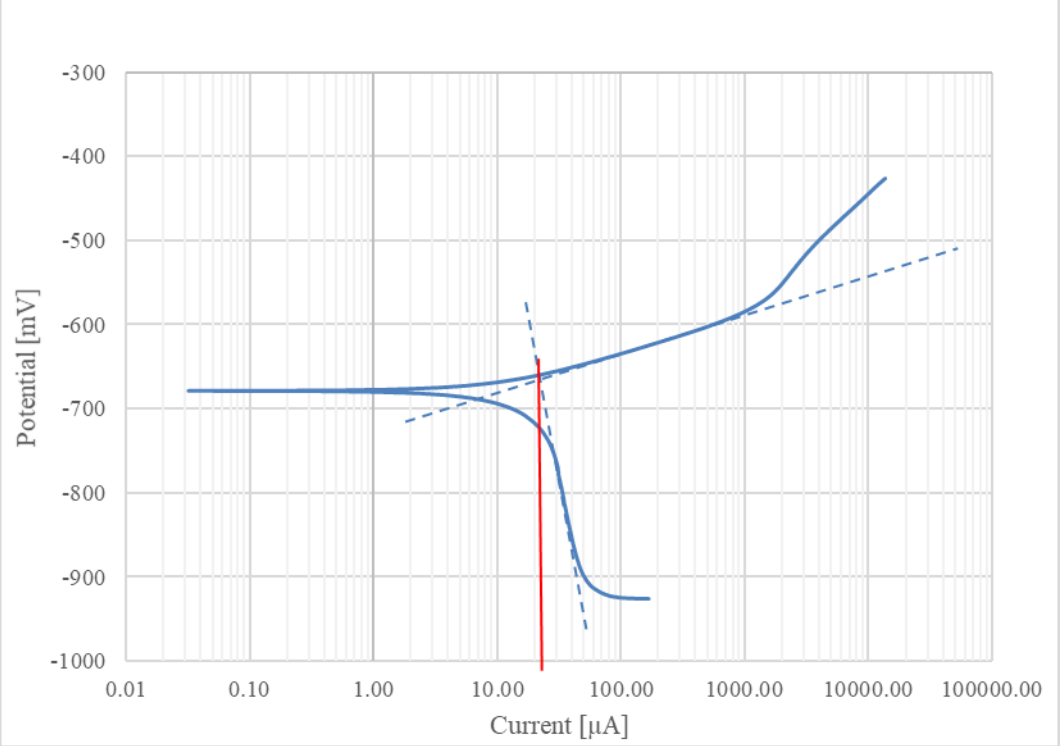

Figure A 6: Polarisation curve of heat treated Sample 2.

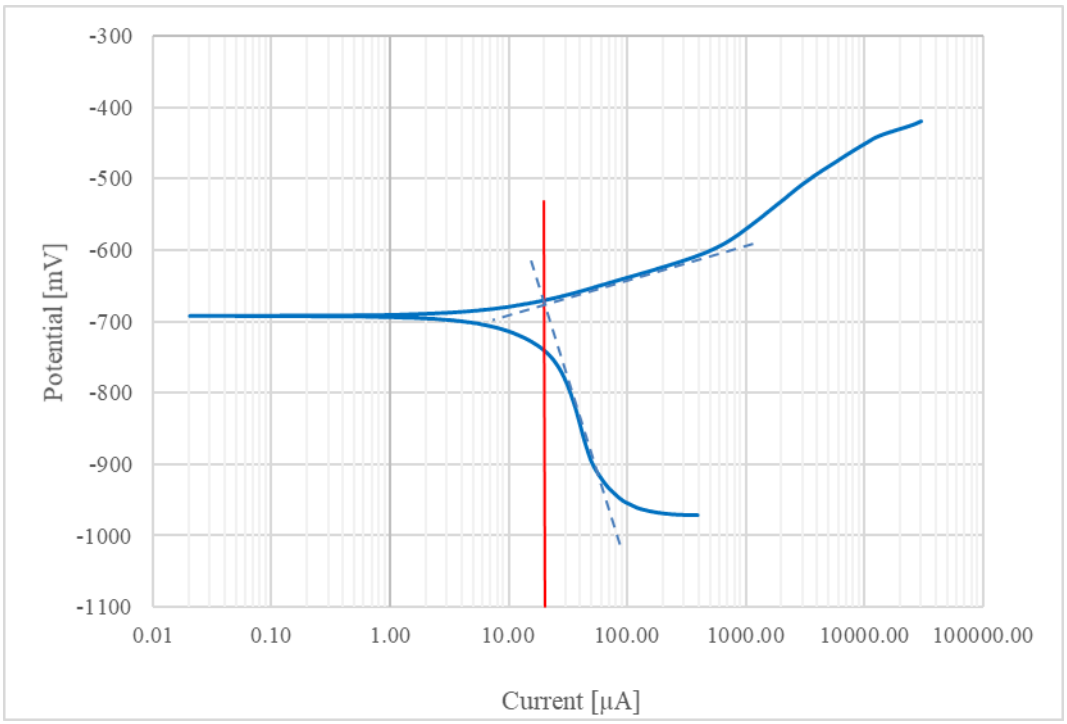

Figure A 7: Polarisation curve of heat treated Sample 3.

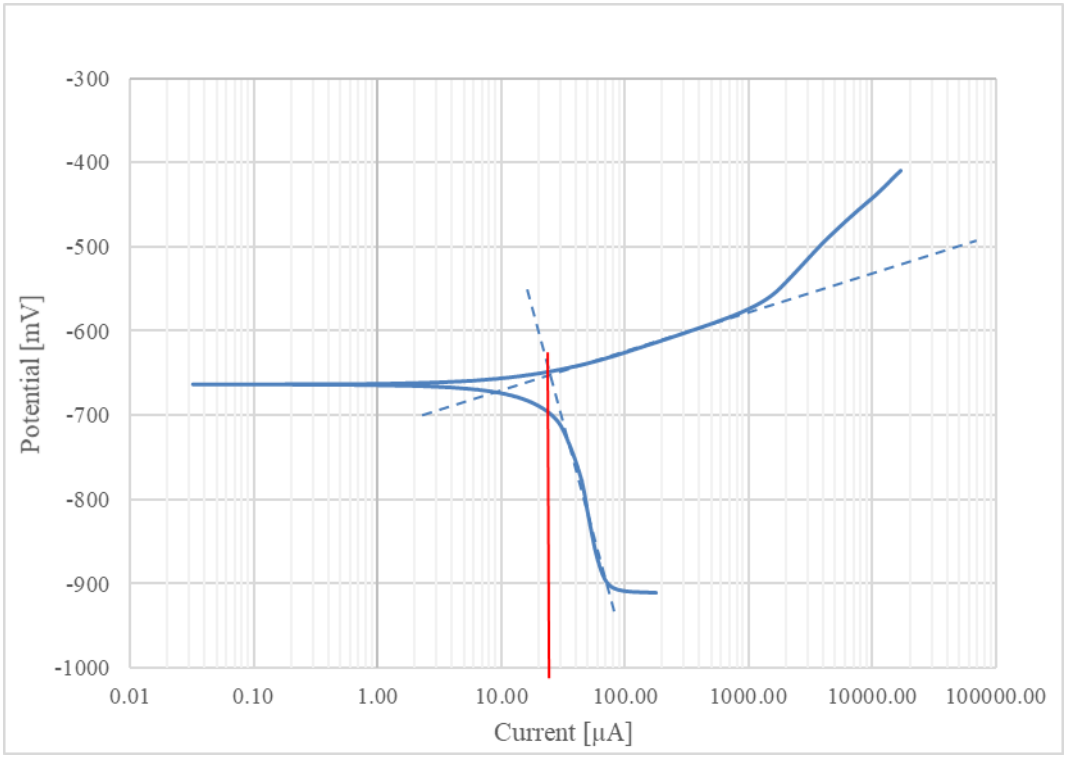

Figure A 8: Polarisation curve of heat treated Sample 4.

Appendix B: Sample calculation for corrosion rate determination

Equivalent weight calculation

Mass fraction (fi) taken as average values from microstructural analysis

$f_{Fe} := 0.931 \qquad f_{Ni} := 0.029 \qquad f_{Cr} := 0.016$

Valence (ni) of elements as shown in ASTM G102-89

$n_{Fe} := 2 \qquad n_{Ni} := 2 \qquad n_{Cr} := 3$

Atomic weight (Wi) of each element

$W_{Fe} := 55.84 \qquad W_{Ni} := 58.693 \qquad W_{Cr} := 51.996$

$$Q := \frac{\left(n_{Fe} \cdot f_{Fe}\right)}{W_{Fe}} + \frac{\left(n_{Ni} \cdot f_{Ni}\right)}{W_{Ni}} + \frac{\left(n_{Cr} \cdot f_{Cr}\right)}{W_{Cr}} = 0.0353 \qquad \text{(Eq 2.5.6)}$$

Equivalent weight is therefore :

$$EW := \frac{1}{Q} = 28.3635 \qquad \text{(Eq 2.5.5)}$$

Parameters determimed experimentally

$R_p := 1019\ \Omega \qquad \rho := 7.79\ \frac{g}{cm^3}$

$b_a := 0.063\ \frac{V}{decade}$

$b_{c\_apparent} := 0.58\ \frac{V}{decade}$

Determining the upper and lower Stern-Geary constants

$$B_{Upper} := \frac{b_a}{2.303} = 0.0274 \qquad \text{(Eq 5.3.1)}$$

$$B_{Lower} := \frac{\left(b_a \cdot b_{c\_apparent}\right)}{2.303 \cdot \left(b_a + b_{c\_apparent}\right)} = 0.0247 \qquad \text{(Eq 5.3.2)}$$

Determining upper and lower corrosion current densities

$A := 1.44\ cm^2$ (Area of electrode)

$K_1 := 3.27 \cdot 10^{-3}\ \frac{(mm \cdot g)}{\mu A \cdot cm \cdot year}$

$$i_{corr\_Lower} := \frac{B_{Lower}}{R_p \cdot A} \cdot 10^6 = 16.8162\ \mu A \qquad \text{(Eq 5.3.3)}$$

$$i_{corr\_Upper} := \frac{B_{Upper}}{R_p \cdot A} \cdot 10^{6} = 18.6427 \quad \mu A$$

Determining upper and lower corrosion rate estimations

$$CR_{Lower} := K_1 \cdot i_{corr\_Lower} \cdot \frac{EW}{\rho} = 0.2002 \quad \frac{mm}{year} \qquad \text{(Eq 2.5.9)}$$

$$CR_{Upper} := K_1 \cdot i_{corr\_Upper} \cdot \frac{EW}{\rho} = 0.222 \quad \frac{mm}{year}$$

Appendix C: Seawater Certificate Of Analysis

Integral Laboratories (Pty) Ltd
No 1 Zandwyk Park, Sandringham Close Paarl, 7646
Tel: 021 863 1238 Fax: 086 635 8874
Email: westerncape@integrallabs.co.za

T0417

Certificate Of Analysis

Company: Hermanus Viljoen
Address: [redacted]

Contact: Hermanus Viljoen

Service Request Number: PW-2020-25261
Date of Certificate: 03-August-2020
Date Completed: 03-August-2020

Date of Sampling: 24-July-2020
Date of Receival at Lab: 24-July-2020

Sample Identification:		Water Sample	
Sample Number: PW-20-87668	Sample Condition: Room Temperature	Remark:	

Chemical	Method	Unit	Limit	Result	Analysis Date
Strontium as Sr	M16	µg/L		648	2020-08-03
Physical / Aesthetic Parameters	**Method**	**Unit**	**Limit**	**Result**	**Analysis Date**
Alkalinity - Total as CaCO3	M7	mg/L		119	2020-07-28
Bicarbonate as HCO3-*	M42	mg/L		145	2020-07-28
Electrical Conductivity @ 25°C	M4	mS/m		5440	2020-07-28
pH @ 25°C	M6	pH units		7.93	2020-07-28
Total Dissolved Solids @ 105°C (Gravimetric)*	M112	mg/L		37618	2020-07-30
Chemistry (Macro) Parameters	**Method**	**Unit**	**Limit**	**Result**	**Analysis Date**
Calcium as Ca	M18	mg/L		394	2020-07-29
Chloride as Cl-	M44	mg/L		18325	2020-07-30
Fluoride as F-	M44	mg/L		0.86	2020-07-30
Magnesium as Mg	M18	mg/L		1220	2020-07-29
Potassium as K	M18	mg/L		581	2020-07-29
Sodium as Na	M18	mg/L		11500	2020-07-29
Sulphate as SO_4^{2-}	M44	mg/L		2473	2020-07-30
Chemistry (Micro) Parameters	**Method**	**Unit**	**Limit**	**Result**	**Analysis Date**
Boron as B	M16	µg/L		3370	2020-07-29
Bromine as Br2*	M48	mg/L		0.15	2020-07-24

Appendix D: Sample calculation of collapse pressures

Material data

$E := 206000\ \text{MPa}$ Young's modulus

$Sy := 550\ \text{MPa}$ Yield strength

$v := 0.3$ Poisson's ratio

$n := 2$

Compartment parameters

$Lc := 15050\ \text{mm}$ Compartment length

$Ls := 430\ \text{mm}$ Stiffener spacing

$R := 3100\ \text{mm}$

$t := 22\ \text{mm}$

Stiffener parameters:

$hw := 225\ \text{mm}$ Stiffener height

$tw := 12\ \text{mm}$ Stiffener width

$tf := 23\ \text{mm}$ Flange thickness

$wf := 115\ \text{mm}$ Flange width

SDF calculations

Stiffener parameters:

$$\alpha := \frac{1.285}{\sqrt{R \cdot t}} = 0.0049$$

$$N := \frac{\cosh(\alpha \cdot Ls) - \cos(\alpha \cdot Ls)}{\sinh(\alpha \cdot Ls) + \sin(\alpha \cdot Ls)} = 0.9563$$

$$G := \frac{2 \cdot \left(\sinh\left(\alpha \cdot \frac{Ls}{2}\right) \cdot \cos\left(\alpha \cdot \frac{Ls}{2}\right) + \cosh\left(\alpha \cdot \frac{Ls}{2}\right) \cdot \sin\left(\alpha \cdot \frac{Ls}{2}\right)\right)}{\sinh(\alpha \cdot Ls) + \sin(\alpha \cdot Ls)} = 0.8204$$

Effective length of a combined stiffener and shell section:

$$Leff := \frac{1.556 \cdot \sqrt{R \cdot t} \cdot N}{\left(\left(1 + 0.5 \cdot n^4 \cdot \left(\frac{t}{R}\right)^2\right)^{0.5} + \left(n^2 \cdot \frac{\left(\frac{t}{R}\right)}{\sqrt{3}}\right)\right)^{0.5}} = 385.3996$$

Combined area of shell plating and stiffener:

$$Ac := wf \cdot tf + hw \cdot tw + Leff \cdot t = 13823.7904$$

Centroid of stiffener from the inside of the shell plating:

$$ys := \frac{\left(hw \cdot tw \cdot \left(\frac{hw}{2}\right) + wf \cdot tf \cdot \left(\frac{tf}{2} + hw\right)\right)}{hw \cdot tw + wf \cdot tf} = 173.862$$

Modified ring frame area:

$$A := R^2 \cdot \frac{(hw \cdot tw + wf \cdot tf)}{(R - ys)^2} = 5999.0364$$

$$B := \frac{2 \cdot t \cdot N}{\alpha \cdot (A + tw \cdot t)} = 1.3653$$

$$\gamma := \frac{A \cdot \left(1 - \frac{v}{2}\right)}{(A + tw \cdot t) \cdot (1 + B)} = 0.3442$$

Pressure at which the mean circumferencial stress at midbay reaches yield stress of the material

$$Py := \frac{Sy \cdot t}{R \cdot (1 - \gamma \cdot G)} = 5.4392$$

Pressure at which the von Mises stress at midbay reaches yield stress of the material

$$Pmy := \frac{Sy \cdot t}{R} \cdot \frac{1}{\sqrt{\frac{1}{4} - \frac{(1 - \gamma \cdot G)}{2} + (1 - \gamma \cdot G)^2}} = 6.1246$$

Elastic instability pressure of a stiffened shell

$$Pm := \frac{E \cdot t}{R \cdot \left(\left(n^2 - 1 + \frac{1}{2} \cdot \left(\frac{\pi \cdot R}{Ls}\right)^2\right)\right)} \cdot \left(\left(n^2 \cdot \left(\frac{Ls}{\pi \cdot R}\right)^2 + 1\right)^{-2} + \frac{t^2}{12 \cdot R^2 \cdot \left(1 - v^2\right)} \cdot \left(n^2 - 1 + \left(\pi \cdot \frac{R}{Ls}\right)^2\right)^2\right) = 12.4649$$

Centroid of the combined stiffener and shell cross-section

$$yc := \frac{\left(Leff \cdot \frac{t^2}{2} + tw \cdot hw \cdot \left(\frac{hw}{2} + t\right) + \left(wf \cdot tf \cdot \left(hw + t + \frac{tf}{2}\right)\right)\right)}{Leff \cdot t + wf \cdot tf + hw \cdot tw} = 82.4773$$

Second moment of inertia of a the combined cross-section of a stiffener and shell section acting about an axis parallel with the cylinder axis passing through the centroid of the combined cross-section

$$Ic := \frac{Leff \cdot t^3}{12} + Leff \cdot t \cdot \left(\frac{t}{2} - yc\right)^2 + \frac{tw \cdot hw^3}{12} + tw \cdot hw \cdot \left(\frac{hw}{2} + t - yc\right)^2 + \frac{wf \cdot tf^3}{12} + = 1.4443 \cdot 10^8$$
$$+ \left(\frac{tf}{2} + t + hw - yc\right)^2 \cdot wf \cdot tf$$

Bryant's approximation of the overall elastic buckling pressure of a cylinder section

$$Pn := \frac{\left(n^2 - 1\right) \cdot E \cdot Ic}{R^3 \cdot Ls} + \frac{\left(E \cdot \frac{t}{R}\right)}{\left(n^2 - 1 + \frac{1}{2} \cdot \left(\frac{\pi \cdot R}{Lc}\right)^2\right)} \cdot \left(\frac{1}{\left(n^2 \cdot \left(\frac{Lc}{\pi \cdot R}\right)^2 + 1\right)^2}\right) = 11.0584$$

Appendix E: Mesh perturbation code

```
clc; clear all ;
fname = 'AbaqusInputFileName.inp' ;
fid = fopen(fname,'r+') ;
S = textscan(fid,'%s','Delimiter','\n');
S = S{1} ;

%Search for nodes start
idPH = strfind(S, 'Node');
idNode = find(not(cellfun('isempty', idPH)));

%Search for 'Element'
idPH = strfind(S, 'Element');
idEl = find(not(cellfun('isempty', idPH)));

% Create nodes variable
nodes = S(idNode+1:idEl-1) ;
nodes2 = cell2mat(cellfun(@str2num,nodes,'UniformOutput',false));


%% Editing node data

%Input dimensional parameters
a = 3100;                                   %Cylinder radius
t = 25;                                     %Cylinder thickness
L = 15050/2;                                %Total cylinder length
Lb = 430;                                   %Stiffener spacing
phi = 3*pi/2;                               %Phase angle
Ao = 0.005*a;                               %Overall OOC amplitude
Ai = 0.01*t;                                %Interframe OOC amplitude
ni=16;
no=2;

X = nodes2(:,2);
Y = nodes2(:,3);
Z = nodes2(:,4);
xmod = (X)/(Lb);

%Determine where the node is in the Y-Z plane
theta = atand(Y./Z);
theta = theta.*(pi/180);

% Determine the change in absolute position
%Overall
delo = Ao.*sin(3*pi/2+no.*theta).*sin(pi/2 + pi.*X./(2*L));
%Interframe
deli = Ai.*sin(phi+ni.*theta).*sin(pi/2 + pi*xmod);
%Combined
del = deli+deli;
```

```
%Write new Y and Z position
Zdiff = (del).*cos(theta);
Ydiff = (del).*sin(theta);
Znew = Zdiff+Z;
Ynew = Ydiff+Y;

nodes2(:,3)=Ynew;
nodes2(:,4)=Znew;
%% Writing perturbed mesh to a new input file
i =1;
G = S;
for count = (idNode+1):1:(idEl-1)
   G{count} = num2str(nodes2(i,:),'%d,    %4.4f,    %4.4f,    %4.4f');
    i = i+1;
end

fid =fopen('NewAbaqusInputFile.inp','w');
str = G;
fprintf(fid,'%s\n',str{:});
fclose(fid);
```

Appendix F: Technical drawings

F.1 Electrochemical corrosion sample specification

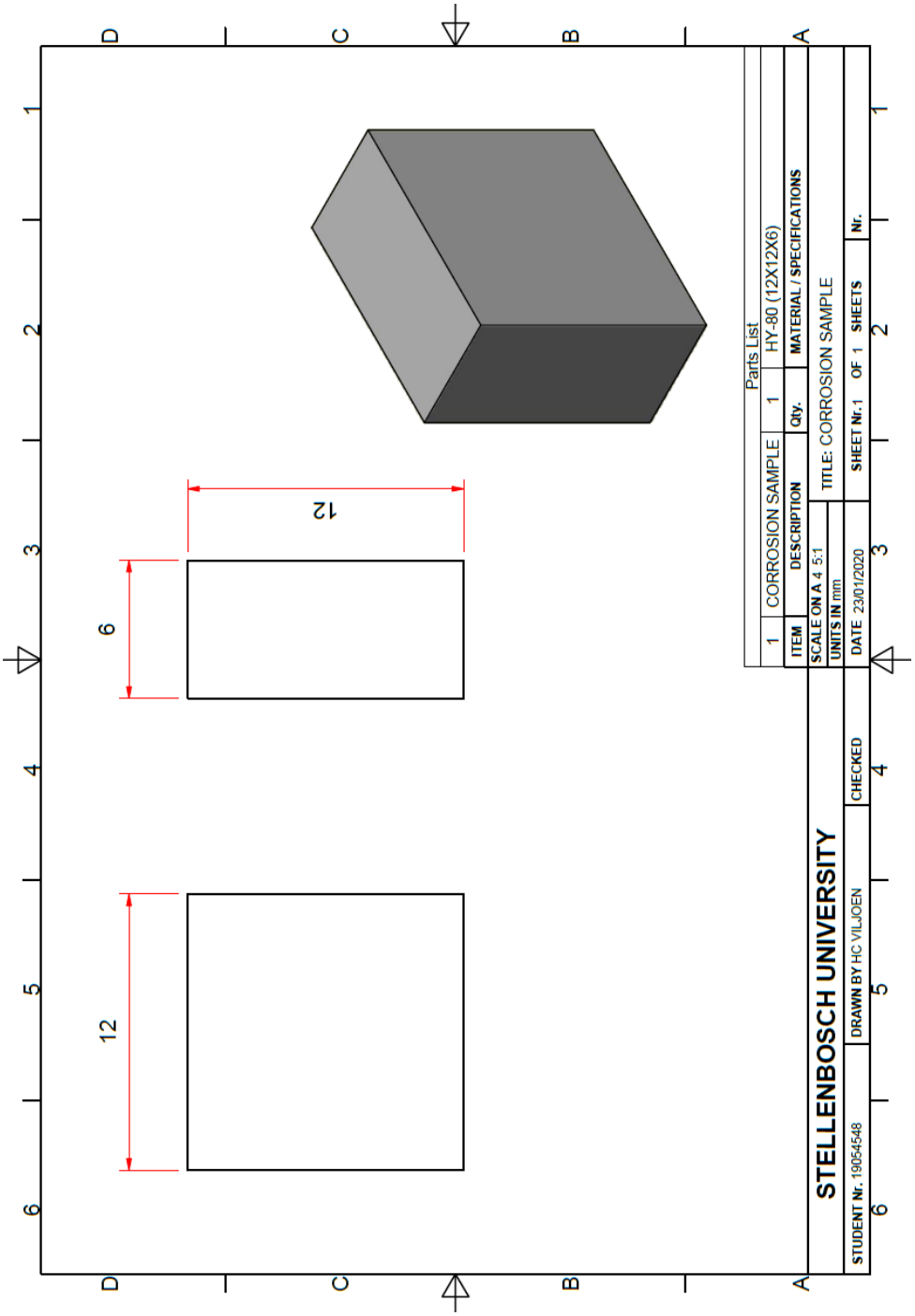

F.2 Tensile specimen specification

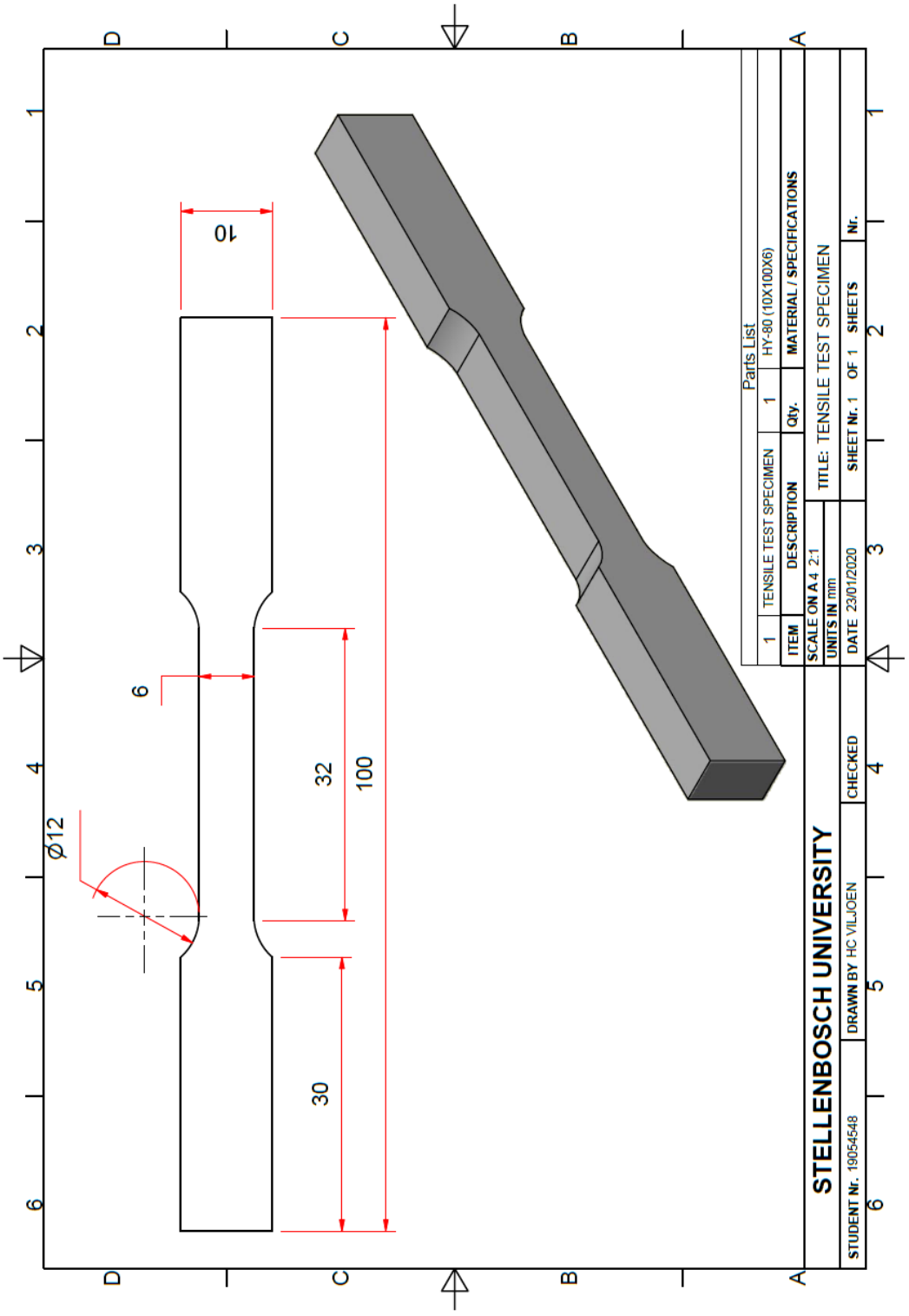

Appendix G: Type 290-1400 Submarine Layout